



TEZ ŞABLONU ONAY FORMU  
THESIS TEMPLATE CONFIRMATION FORM

1. Şablonda verilen yerleşim ve boşluklar değiştirilmemelidir.
2. **Jüri tarihi** Başlık Sayfası, İmza Sayfası, Abstract ve Öz'de ilgili yerlere yazılmalıdır.
3. İmza sayfasında jüri üyelerinin unvanları doğru olarak yazılmalıdır. Tüm imzalar **mavi pilot kalemle** atılmalıdır.
4. **Disiplinlerarası** programlarda görevlendirilen öğretim üyeleri için jüri üyeleri kısmında tam zamanlı olarak çalıştıkları anabilim dalı başkanlığının ismi yazılmalıdır. Örneğin: bir öğretim üyesi Biyoteknoloji programında görev yapıyor ve biyoloji bölümünde tam zamanlı çalışıyorsa, İmza sayfasına biyoloji bölümü yazılmalıdır. İstisnai olarak, disiplinler arası program başkanı ve tez danışmanı için disiplinlerarası program adı yazılmalıdır.
5. Tezin **son sayfasının sayfa** numarası Abstract ve Öz'de ilgili yerlere yazılmalıdır.
6. Bütün chapterlar, referanslar, ekler ve CV sağ sayfada başlamalıdır. Bunun için **kesmeler** kullanılmıştır. **Kesmelerin kayması** fazladan boş sayfaların oluşmasına sebep olabilir. Bu gibi durumlarda paragraf (¶) işaretine tıklayarak kesmeleri görünür hale getirin ve yerlerini **kontrol edin**.
7. Figürler ve tablolar kenar boşluklarına taşmamalıdır.
8. Şablonda yorum olarak eklenen uyarılar dikkatle okunmalı ve uygulanmalıdır.
9. Tez yazdırılmadan önce PDF olarak kaydedilmelidir. Şablonda yorum olarak eklenen uyarılar PDF dokümanında yer almamalıdır.
10. Tez taslaklarının kontrol işlemleri tamamlandığında, bu durum öğrencilere METU uzantılı öğrenci e-posta adresleri aracılığıyla duyurulacaktır.
11. Tez yazım süreci ile ilgili herhangi bir sıkıntı yaşarsanız, [Sıkça Sorulan Sorular \(SSS\)](#) sayfamızı ziyaret ederek yaşadığınız sıkıntıyla ilgili bir çözüm bulabilirsiniz.

1. Do not change the spacing and placement in the template.
2. Write **defense date** to the related places given on Title page, Approval page, Abstract and Öz.
3. Write the titles of the examining committee members correctly on Approval Page. **Blue ink** must be used for all signatures.
4. For faculty members working in **interdisciplinary programs**, the name of the department that they work full-time should be written on the Approval page. For example, if a faculty member staffs in the biotechnology program and works full-time in the biology department, the department of biology should be written on the approval page. Exceptionally, for the interdisciplinary program chair and your thesis supervisor, the interdisciplinary program name should be written.
5. Write **the page number of the last page** in the related places given on Abstract and Öz pages.
6. All chapters, references, appendices and CV must be started on the right page. **Section Breaks** were used for this. **Change in the placement** of section breaks can result in extra blank pages. In such cases, make the section breaks visible by clicking paragraph (¶) mark and **check their position**.
7. All figures and tables must be given inside the page. Nothing must appear in the margins.
8. All the warnings given on the comments section through the thesis template must be read and applied.
9. Save your thesis as pdf and Disable all the comments before taking the printout.
10. This will be announced to the students via their METU students e-mail addresses when the control of the thesis drafts has been completed.
11. If you have any problems with the thesis writing process, you may visit our [Frequently Asked Questions \(FAQ\)](#) page and find a solution to your problem.

Yukarıda bulunan tüm maddeleri okudum, anladım ve kabul ediyorum. / I have read, understand and accept all of the items above.

Name : Abdullah Azad  
Surname : Yılmaz  
E-Mail :  
Date :  
Signature : \_\_\_\_\_



METHANE TO METHANOL PARTIAL OXIDATION USING Cu-FERRIERITE

A THESIS SUBMITTED TO  
THE GRADUATE SCHOOL OF NATURAL AND APPLIED SCIENCES  
OF  
MIDDLE EAST TECHNICAL UNIVERSITY

BY

ABDULLAH AZAD YILMAZ

IN PARTIAL FULFILLMENT OF THE REQUIREMENTS  
FOR  
THE DEGREE OF MASTER OF SCIENCE  
IN  
CHEMICAL ENGINEERING

JULY 2024



Approval of the thesis:

**METHANE TO METHANOL PARTIAL OXIDATION USING Cu-FERRIERITE**

submitted by **ABDULLAH AZAD YILMAZ** in partial fulfillment of the requirements for the degree of **Master of Science in Chemical Engineering, Middle East Technical University** by,

Prof. Dr. Naci Emre Altun  
Dean, Graduate School of **Natural and Applied Sciences**

Prof. Dr. Yusuf Uludağ  
Head of the Department, **Chemical Engineering**

Assoc. Prof. Dr. Bahar İpek Torun  
Supervisor, **Chemical Engineering, METU**

**Examining Committee Members:**

Prof. Dr. Deniz Üner  
Chemical Engineering, METU

Assoc. Prof. Dr. Bahar İpek Torun  
Chemical Engineering, METU

Prof. Dr. Halil Kalıpçılar  
Chemical Engineering, METU

Prof. Dr. Burcu Akata Kurç  
Micro and Nanotechnology, METU

Assoc. Prof. Dr. Kadriye Özlem Hamaloğlu  
Chemical Engineering, Hacettepe University

Date: 12.07.2024

**I hereby declare that all information in this document has been obtained and presented in accordance with academic rules and ethical conduct. I also declare that, as required by these rules and conduct, I have fully cited and referenced all material and results that are not original to this work.**

Name Last name : Abdullah Azad Yılmaz

Signature :

## ABSTRACT

### METHANE TO METHANOL PARTIAL OXIDATION USING Cu-FERRIERITE

Yılmaz, Abdullah Azad

Master of Science, Chemical Engineering

Supervisor: Assoc. Prof. Dr. Bahar İpek Torun

July 2024, 151 pages

Methane is an abundant chemical but it is not easy to transport or convert to other chemicals. This is mainly because methane is a stable molecule, its conversion is highly energy intensive and selectivity to desired product is low due to overoxidation. In this study, the partial oxidation of methane to methanol by continuous catalytic method using  $N_2O$  in copper-containing zeolites (AEI, CHA, FER) is examined. These zeolites, especially FER, were optimized using different copper amounts and it was found that infinitesimal amount of copper ( $Cu/Al=0.02$ ) gave the highest methanol formation. Among different heating methods, heating of the catalyst bed with helium rather than reactant gases was preferred for higher methanol production and reusability. The activity tests were carried out under 100 sccm total flow with 40%  $CH_4$ , 15%  $N_2O$ , 3%  $H_2O$  and balance He at 310–325 °C and the highest methanol production with high stability ( $1249 \mu mol g^{-1}h^{-1}$ ) was detected over FER at 325 °C among other microporous zeolite samples. Nano-FER was synthesized in order to improve selectivity and to increase the methanol production and it was found to be more active compared to Micro-FER ( $1594 \mu mol g^{-1}h^{-1}$  at 325 °C).  $H_2O$  effect was also studied and the optimum condition of 9%  $H_2O$  was chosen. The best result in terms of activity was obtained over Nano-Cu-FER\_1 with the methanol formation rate of  $2174 \mu mol g^{-1}h^{-1}$  and methanol selectivity of 79%. In line with the activation energy calculation and UV–Vis analyses, monocopper was identified as the active site.

Keywords: Methane, Methanol, Copper, FER,  $H_2O$

## ÖZ

### **Cu-FERRİERİT KULLANILARAK METANIN METANOLE KİSMİ YÜKSELTGENMESİ**

Yılmaz, Abdullah Azad  
Yüksek Lisans, Kimya Mühendisliği  
Tez Yöneticisi: Doç. Dr. Bahar İpek Torun

Temmuz 2024, 151 sayfa

Metan, doğada bol miktarda bulunan ancak taşınması veya diğer kimyasallara dönüştürülmesi kolay olmayan bir kimyasaldır. Bunun temel nedeni, metanın kararlı bir molekül olması ve dönüşümünde tam oksidasyon nedeniyle istenen ürünün seçiciliğinin düşük olması ve dönüşümü için yüksek enerji gerektirmesidir. Bu çalışmada bakır içeren zeolitlerde  $N_2O$  kullanılarak sürekli katalitik yöntemle metanın metanole kısmi oksidasyonu incelenmiştir. Bu kapsamda, başta FER olmak üzere AEI ve CHA çerçeve yapısına sahip zeolitler farklı bakır miktarlarında optimize edilmiş ve oldukça düşük bakır miktarının ( $Cu/Al=0.02$ ) en yüksek metanol oluşumunu sağladığı tespit edilmiştir. Reaksiyonun reaksiyona giren gazlar yerine helyum ile ısıtma yöntemi metanol üretimi artışı ve örneklerin tekrar kullanılabilirliği için tercih edilmiştir. Aynı koşullar altında (100 sccm toplam akış, %40  $CH_4$ , %15  $N_2O$ , %3  $H_2O$ , %42 He ve 325 °C) yapılan aktivite testi sonuçlarında mikro gözenekli zeolitler arasında en kararlı ve en yüksek metanol üretimi ( $1249 \mu mol g^{-1}h^{-1}$ ) FER zeolitinde tespit edilmiştir. Nano-FER, seçiciliği geliştirmek ve metanol üretimini artırmak için sentezlenmiş ve aktivite testinde Mikro-FER'e kıyasla daha aktif olmuştur ( $1594 \mu mol g^{-1}h^{-1}$  325 °C'de).  $H_2O$  etkisi incelenmiş ve optimum koşul olarak %9  $H_2O$  seçilmiş ve aktivite açısından en iyi sonuç  $2174 \mu mol g^{-1}h^{-1}$  metanol oluşum hızı ve %79 seçicilik ile Nano-Cu-FER\_1 olmuştur. Aktivasyon enerjisi hesaplaması ve UV-Vis analizi ile beraber incelenerek, mono-bakırların aktif site oluşturduğu tespit edilmiştir.

Anahtar Kelimeler: Metan, Metanol, Bakır, FER,  $H_2O$

To my family, present and future

## ACKNOWLEDGMENTS

I would like to start by expressing my gratitude to my supervisor Assoc. Prof. Dr. Bahar İpek Torun for her guidance and advice provided throughout my graduate studies. By providing me a pressure-free environment, she gave me the opportunity to realize what I was curious about, a scientific perspective and self-confidence.

I would also like to thank the thesis examination committee Prof. Dr. Deniz Üner, Prof. Dr. Halil Kalıpçılar, Prof. Dr. Burcu Akata Kurç and Assoc. Prof. Dr. Kadriye Özlem Hamaloğlu.

I acknowledge the financial support by the HDESP-304-2021-10806 project number within the scope of Scientific Research Projects Coordination Unit General Research Project. I would like to thank Tübitak-BİDEB 2210-A for the scholarship they provided.

I would like to thank Selin Karahan, Merve Sarıyer Almira Çaldıklıoğlu, Görkem Bak, Oğuzhan Coşğun, Bedirhan Kapkiç and Hüseyin Öztürk for being my dear friends. I am also grateful to my close friends Hakan Kerem Ergül, Oktay Erkan Temizkan, Enes Sak, Ahmet Sert.

I would like to express my appreciation to my family, especially parents Müslüm and Muhlise Yılmaz for their constant love and care. I am grateful to them for raising me to be a strong and independent person.

Finally, I would like to express my deepest gratitude to Asena Kızıl. She was always there for me on my most difficult days and always gave me hope. While working in the same laboratory with her, I learned a lot from her about work discipline, organization and the systematics of science. It has always been a great pleasure to work with her and I hope it will be always possible in future.

## TABLE OF CONTENTS

ABSTRACT.....	v
ÖZ.....	vi
ACKNOWLEDGMENTS.....	viii
TABLE OF CONTENTS.....	ix
LIST OF TABLES.....	xiii
LIST OF FIGURES.....	xvi
LIST OF ABBREVIATIONS.....	xx
LIST OF SYMBOLS.....	xxi
CHAPTERS	
1 INTRODUCTION.....	1
1.1 Methane as a Feedstock.....	1
1.2 Methanol Production.....	4
1.3 Studies in The Literature and Industry on The Catalytic Methane to Methanol Conversion Process.....	5
1.3.1 Indirect Methane to Methanol Conversion.....	6
1.3.2 Direct Methane to Methanol Conversion.....	7
1.4 The Challenges in Direct Methane Conversion to Methanol.....	8
1.5 The Performance Targets for Feasibility of MTM.....	9
1.6 The Types of Catalyst Used in MTM.....	11
1.7 Zeolites.....	12
1.7.1 Synthesis of Zeolites.....	13
1.7.2 Structure of Zeolites.....	14

1.7.3	Si/Al Ratio of Zeolites .....	15
1.7.4	Brønsted Acidity of Zeolites.....	15
1.8	Zeolites Used in This Study .....	15
1.8.1	FER (Ferrierite).....	16
1.8.2	AEI (SSZ-39).....	17
1.8.3	CHA (SSZ-13).....	18
1.9	The Objective of This Study.....	19
2	LITERATURE REVIEW .....	21
2.1	The Types, Identification and Formation of Cu Active Sites.....	21
2.1.1	The Identification of The Types of Cu Active Sites.....	21
2.1.2	Cu Active Site Formation .....	24
2.2	Activity Test of Cu-Zeolites .....	31
2.3	Reaction Mechanism Studies .....	37
3	EXPERIMENTAL METHODOLOGY .....	41
3.1	Catalyst Synthesis and Preparation .....	41
3.1.1	Micro-H <sup>+</sup> -FER .....	41
3.1.2	Nano-H <sup>+</sup> -FER .....	41
3.1.3	Steam-Meso-H <sup>+</sup> -FER.....	42
3.1.4	CTABr-Meso-H <sup>+</sup> -FER.....	42
3.1.5	Micro-H <sup>+</sup> -SSZ-39 .....	43
3.1.6	Micro-H <sup>+</sup> -SSZ-13 .....	43
3.2	Ion-Exchange Procedure .....	44
3.2.1	Na <sup>+</sup> -Exchange .....	44
3.2.2	NH <sub>4</sub> <sup>+</sup> -Exchange.....	45

3.2.3	Cu <sup>2+</sup> -Exchange .....	45
3.2.4	Co <sup>2+</sup> -Exchange .....	46
3.3	Characterization Methods and Techniques .....	46
3.3.1	N <sub>2</sub> Physisorption at 77K.....	46
3.3.2	X-Ray Diffraction (XRD) Analysis .....	47
3.3.3	Elemental Analysis.....	47
3.3.4	Scanning Electron Microscopy (SEM) .....	47
3.3.5	Transmission Electron Microscopy (TEM).....	48
3.3.6	<sup>27</sup> Al and <sup>29</sup> Si Magic Angle Spinning Nuclear Magnetic Resonance .....	48
3.3.7	In-Situ Raman Spectroscopy .....	48
3.3.8	In-Situ Diffuse Reflectance UV–Visible Spectroscopy .....	49
3.4	Reaction System and Procedure.....	50
4	RESULTS AND DISCUSSION .....	53
4.1	Characterization Results .....	53
4.1.1	Elemental Analysis.....	53
4.1.2	X-Ray Diffraction Analysis .....	57
4.1.3	SEM Analysis.....	63
4.1.4	TEM Analysis .....	67
4.1.5	N <sub>2</sub> Physisorption at -196°C Analysis .....	70
4.1.6	<sup>27</sup> Al MAS NMR .....	81
4.1.7	<sup>29</sup> Si MAS NMR .....	84
4.1.8	Raman Spectroscopy Results .....	87
4.1.9	In-Situ DR UV–Vis .....	88
4.2	Activity Test Results.....	93

4.2.1	Activity Test Results with Reactant Heating Method .....	93
4.2.2	Activity Test Results with Helium Heating Method .....	102
5	CONCLUSION .....	117
	REFERENCES .....	119
	APPENDICES .....	139
A.	Deconvolution of $^{27}\text{Al}$ -MAS-NMR and $^{29}\text{Al}$ -MAS-NMR .....	139
B.	Detailed Activity Test Results .....	141

## LIST OF TABLES

### TABLES

Table 2.1. Cu active sites and coordination structures.....	21
Table 2.2. Activity test results given in the literature .....	34
Table 4.1. Ion-exchange conditions and elemental analysis results using ICP-OES .....	55
Table 4.2. Surface Area and Pore Volume of Samples.....	75
Table 4.3. Activation energy values of FER samples .....	114
Table A.1. Al structure of Nano-FER and Micro-FER using Dedeczek Method....	138
Table B.1. Micro-Cu-FER activity results 100 sccm total flow, 40% CH <sub>4</sub> , 15% N <sub>2</sub> O, 3% H <sub>2</sub> O, balance He at 325 °C (Reactant Heating). Yields based on per g <sub>zeolite</sub> (300 mg). r unit is μmolg <sup>-1</sup> h <sup>-1</sup> .....	141
Table B.2. Micro-Cu-FER activity results 100 sccm total flow, 40% CH <sub>4</sub> , 5-15% N <sub>2</sub> O, 3% H <sub>2</sub> O, balance He at 325 °C (Reactant Heating). Yields based on per g <sub>zeolite</sub> (300 mg). r unit is μmolg <sup>-1</sup> h <sup>-1</sup> .....	142
Table B.3. Meso-Steam/CTABr-Cu-FER activity results 100 sccm total flow, 40% CH <sub>4</sub> , 15% N <sub>2</sub> O, 3% H <sub>2</sub> O, balance He at 325 °C (Reactant Heating). Yields based on per g <sub>zeolite</sub> (300 mg). r unit is μmolg <sup>-1</sup> h <sup>-1</sup> .....	142
Table B.4. Micro-Cu-SSZ-39 activity results 100 sccm total flow, 40% CH <sub>4</sub> , 15% N <sub>2</sub> O, 3% H <sub>2</sub> O, balance He at 325 °C (Reactant Heating). Yields based on per g <sub>zeolite</sub> (300 mg). r unit is μmolg <sup>-1</sup> h <sup>-1</sup> .....	143
Table B.5. Micro-Cu-FER_1 activity results 100 sccm total flow, 40% CH <sub>4</sub> , 15% N <sub>2</sub> O, 3% H <sub>2</sub> O, balance He at 325 °C (Reactant Heating). Yields based on per g <sub>zeolite</sub> (300 mg). r unit is μmolg <sup>-1</sup> h <sup>-1</sup> .....	143
Table B.6. Micro-Cu-FER_2 activity results 100 sccm total flow, 40% CH <sub>4</sub> , 15% N <sub>2</sub> O, 3% H <sub>2</sub> O, balance He at 325 °C (Helium Heating). Yields based on per g <sub>zeolite</sub> (300 mg). r unit is μmolg <sup>-1</sup> h <sup>-1</sup> .....	144
Table B.7. Micro-Cu-FER activity results 100 sccm total flow, 40% CH <sub>4</sub> , 15% N <sub>2</sub> O, 3% H <sub>2</sub> O, balance He at 325 °C (Helium Heating). Yields based on per g <sub>zeolite</sub> (300	

mg). r unit is $\mu\text{molg}^{-1}\text{h}^{-1}$ .....	144
Table B.8. Fresh Nano-Cu-FER activity results 100 sccm total flow, 40% CH <sub>4</sub> , 15% N <sub>2</sub> O, 3% H <sub>2</sub> O, balance He at 325 °C (Helium Heating). Yields based on per $g_{\text{zeolite}}$ (300 mg). r unit is $\mu\text{molg}^{-1}\text{h}^{-1}$ .....	145
Table B.9. Fresh Micro-Cu-SSZ-39 activity results 100 sccm total flow, 40% CH <sub>4</sub> , 15% N <sub>2</sub> O, 3% H <sub>2</sub> O, balance He at 325 °C (Helium Heating). Yields based on per $g_{\text{zeolite}}$ (300 mg). r unit is $\mu\text{molg}^{-1}\text{h}^{-1}$ .....	145
Table B.10. Fresh Micro-Cu-SSZ-13 activity results 100 sccm total flow, 40% CH <sub>4</sub> , 15% N <sub>2</sub> O, 3% H <sub>2</sub> O, balance He at 325 °C (Helium Heating). Yields based on per $g_{\text{zeolite}}$ (300 mg). r unit is $\mu\text{molg}^{-1}\text{h}^{-1}$ .....	146
Table B.11. Fresh Micro-Cu-FER_1 activity results 100 sccm total flow, 40% CH <sub>4</sub> , 15% N <sub>2</sub> O, 0-9% H <sub>2</sub> O, balance He at 325 °C (Helium Heating). Yields based on per $g_{\text{zeolite}}$ (300 mg). r unit is $\mu\text{molg}^{-1}\text{h}^{-1}$ .....	146
Table B.12. Fresh Nano-Cu-FER_1 activity results 100 sccm total flow, 40% CH <sub>4</sub> , 15% N <sub>2</sub> O, 0-9% H <sub>2</sub> O, balance He at 325 °C (Helium Heating). Yields based on per $g_{\text{zeolite}}$ (300 mg). r unit is $\mu\text{molg}^{-1}\text{h}^{-1}$ .....	147
Table B.13. Micro-Cu-FER_1 activity results 100 sccm total flow, 40% CH <sub>4</sub> , 15% N <sub>2</sub> O, 3% H <sub>2</sub> O, balance He at different temperatures (Helium Heating). Yields based on per $g_{\text{zeolite}}$ (300 mg). r unit is $\mu\text{molg}^{-1}\text{h}^{-1}$ .....	147
Table B.14. Micro-Cu-FER_2 activity results 100 sccm total flow, 40% CH <sub>4</sub> , 15% N <sub>2</sub> O, 3% H <sub>2</sub> O, balance He at different temperatures (Helium Heating). Yields based on per $g_{\text{zeolite}}$ (300 mg). r unit is $\mu\text{molg}^{-1}\text{h}^{-1}$ .....	148
Table B.15. Micro-Cu-FER_3 activity results 100 sccm total flow, 40% CH <sub>4</sub> , 15% N <sub>2</sub> O, 3% H <sub>2</sub> O, balance He at different temperatures (Helium Heating). Yields based on per $g_{\text{zeolite}}$ (300 mg). r unit is $\mu\text{molg}^{-1}\text{h}^{-1}$ .....	149
Table B.16. Nano-Cu-FER_1 activity results 100 sccm total flow, 40% CH <sub>4</sub> , 15% N <sub>2</sub> O, 3% H <sub>2</sub> O, balance He at different temperatures (Helium Heating). Yields based on per $g_{\text{zeolite}}$ (300 mg). r unit is $\mu\text{molg}^{-1}\text{h}^{-1}$ .....	150
Table B.17. Nano-Cu-FER_2 activity results 100 sccm total flow, 40% CH <sub>4</sub> , 15%	

N<sub>2</sub>O, 3% H<sub>2</sub>O, balance He at different temperatures (Helium Heating). Yields based on per g<sub>zeolite</sub> (300 mg). r unit is μmolg<sup>-1</sup>h<sup>-1</sup>.....151

## LIST OF FIGURES

### FIGURES

Figure 1.1. Global emissions coming from methane and methane flaring between 1990 and 2022 (units in bcm) [9] .....	2
Figure 1.2. Methane conversion routes and end products [11] .....	3
Figure 1.3. MTM production methods [15].....	6
Figure 1.4. Stepwise MTM Process [17].....	8
Figure 1.5. Enzymes and zeolites active center representation [28] .....	12
Figure 1.6. FER Framework viewed along [001] [51] .....	16
Figure 1.7. AEI Framework viewed along [001] [53].....	17
Figure 1.8. AEI Framework viewed along [001] [56].....	18
Figure 2.1. Possible reaction mechanism on the Cu-monomer [CuOH] <sup>+</sup> (A) and Cu-dimer [Cu <sub>2</sub> O] <sup>2+</sup> (B) in a continuous DMTM using DFT simulation [103].....	37
Figure 2.2. Possible reaction mechanism for Cu/SSZ-39 [105].....	39
Figure 3.1. The schematic representation of reaction set-up.....	52
Figure 4.1. XRD pattern of Micro-H <sup>+</sup> -FER.....	57
Figure 4.2. XRD pattern of Meso-Steam-H <sup>+</sup> -FER .....	58
Figure 4.3. XRD pattern of Meso-CTABr-H <sup>+</sup> -FER .....	59
Figure 4.4. XRD pattern of Micro-H <sup>+</sup> -SSZ-39.....	59
Figure 4.5. XRD patterns of Micro-H <sup>+</sup> -FER and Micro-Cu-FER samples.....	60
Figure 4.6. XRD patterns of Nano-H <sup>+</sup> -FER and Nano-Cu-FER samples .....	60
Figure 4.7. XRD patterns of Micro-H <sup>+</sup> -SSZ-39 before and after HCl treatment ....	61
Figure 4.8. XRD patterns of Micro-H <sup>+</sup> -SSZ-39 and Micro-Cu-SSZ-39 samples ...	61
Figure 4.9. XRD patterns of Micro-H <sup>+</sup> -SSZ-13 and Micro-Cu-SSZ-13 samples ...	62
Figure 4.10. SEM Image of Micro-H <sup>+</sup> -FER.....	63
Figure 4.11. SEM Image of Meso-Steam-H <sup>+</sup> -FER .....	64
Figure 4.12. SEM Image of Meso-CTABr-H <sup>+</sup> -FER .....	64
Figure 4.13. SEM Image of Nano-H <sup>+</sup> -FER .....	65
Figure 4.14. SEM Image of Micro-H <sup>+</sup> -SSZ-39 before HCl treatment .....	65

Figure 4.15. SEM Image of Micro-H <sup>+</sup> -SSZ-39 after HCl treatment .....	66
Figure 4.16. SEM Image of Micro-H <sup>+</sup> -SSZ-13.....	67
Figure 4.17. HR-TEM Image of fresh Micro-Cu-FER_1 .....	67
Figure 4.18. HR-TEM Image of Micro-Cu-FER_1 after reaction.....	68
Figure 4.19. HR-TEM Image of fresh Micro-Cu-SSZ-39_3 (above) and d-spacing calculations (below) .....	69
Figure 4.20. N <sub>2</sub> adsorption/desorption isotherms of Micro-H <sup>+</sup> -FER.....	70
Figure 4.21. N <sub>2</sub> adsorption/desorption isotherms of Meso-Steam-H <sup>+</sup> -FER.....	71
Figure 4.22. N <sub>2</sub> adsorption/desorption isotherms of Meso-CTABr-H <sup>+</sup> -FER.....	72
Figure 4.23. N <sub>2</sub> adsorption/desorption isotherms of Micro-H <sup>+</sup> -SSZ-39 .....	72
Figure 4.24. N <sub>2</sub> adsorption/desorption isotherms of Micro-Cu-FER.....	73
Figure 4.25. N <sub>2</sub> adsorption/desorption isotherms of Nano-Cu-FER.....	73
Figure 4.26. N <sub>2</sub> adsorption/desorption isotherms of Micro-Cu-SSZ-39.....	74
Figure 4.27. N <sub>2</sub> adsorption/desorption isotherms of Micro-Cu-SSZ-13.....	74
Figure 4.28. BJH adsorption pore size distribution of Micro-H <sup>+</sup> -FER.....	77
Figure 4.29. BJH adsorption pore size distribution of Meso-Steam-H <sup>+</sup> -FER .....	77
Figure 4.30. BJH adsorption pore size distribution of Meso-CTABr-H <sup>+</sup> -FER .....	78
Figure 4.31. BJH adsorption pore size distribution of Micro-H <sup>+</sup> -SSZ-39.....	78
Figure 4.32. BJH adsorption pore size distributions of Micro-Cu-FER .....	79
Figure 4.33. BJH adsorption pore size distributions of Nano-Cu-FER .....	79
Figure 4.34. BJH adsorption pore size distributions of Micro-Cu-SSZ-39 .....	80
Figure 4.35. BJH adsorption pore size distributions of Micro-Cu-SSZ-13 .....	80
Figure 4.36. <sup>27</sup> Al-MAS-NMR Spectra of Micro-NH <sub>4</sub> <sup>+</sup> -FER .....	81
Figure 4.37. <sup>27</sup> Al-MAS-NMR Spectra of Meso-Steam-NH <sub>4</sub> <sup>+</sup> -FER.....	82
Figure 4.38. <sup>27</sup> Al-MAS-NMR Spectra of Micro-NH <sub>4</sub> <sup>+</sup> -SSZ-39 .....	83
Figure 4.39. <sup>27</sup> Al-MAS-NMR Spectra of Nano-Na <sup>+</sup> -FER.....	83
Figure 4.40. <sup>29</sup> Si-MAS-NMR Spectra of Micro-NH <sub>4</sub> <sup>+</sup> -FER .....	84
Figure 4.41. <sup>29</sup> Si-MAS-NMR Spectra of Meso-Steam-NH <sub>4</sub> <sup>+</sup> -FER.....	85
Figure 4.42. <sup>29</sup> Si-MAS-NMR Spectra of Micro-NH <sub>4</sub> <sup>+</sup> -SSZ-39 .....	85
Figure 4.43. <sup>29</sup> Si-MAS-NMR Spectra of Nano-Na <sup>+</sup> -FER.....	86

Figure 4.44. Raman Spectra of Micro-Cu-SSZ-39_3R .....	87
Figure 4.45. In-situ DR UV–Vis spectra of Micro-Cu-FER_1 .....	88
Figure 4.46. In-situ DR UV–Vis spectra of Micro-Cu-FER_2 .....	89
Figure 4.47. In-situ DR UV–Vis spectra of Micro-Cu-FER_3 .....	90
Figure 4.48. In-situ DR UV–Vis spectra of Nano-Cu-FER_1 .....	91
Figure 4.49. In-situ DR UV–Vis spectra of Nano-Cu-FER_2 .....	92
Figure 4.50. In-situ DR UV–Vis spectra of Micro-Cu-SSZ-39_3 .....	92
Figure 4.51. Activity test results of Micro-Cu-FER samples, 325 °C, 40% methane, 15% N <sub>2</sub> O, 3% H <sub>2</sub> O and 42% He .....	93
Figure 4.52. Activity test results of Micro-Cu-FER samples with and without Na <sup>+</sup> ions, 325 °C, 40% methane, 15% N <sub>2</sub> O, 3% H <sub>2</sub> O and 42% He.....	95
Figure 4.53. Activity test results of Micro-Cu-FER_1 sample, 325 °C, 40% methane, 5 or 15% N <sub>2</sub> O, 3% H <sub>2</sub> O and balance He.....	96
Figure 4.54. Activity test results of Micro-Cu-FER_1 sample with and without calcination, 325 °C, 40% methane, 15% N <sub>2</sub> O, 3% H <sub>2</sub> O and 42% He.....	97
Figure 4.55. Activity test results of Micro-Cu-FER and Meso-Steam-Cu-FER samples, 325 °C, 40% methane, 15% N <sub>2</sub> O, 3% H <sub>2</sub> O and 42% He.....	98
Figure 4.56. Activity test results of Micro-Cu-FER and Meso-CTABr-Cu-FER samples, 325 °C, 40% methane, 15% N <sub>2</sub> O, 3% H <sub>2</sub> O and 42% He.....	99
Figure 4.57. Activity test results of Micro-Cu-SSZ-39 samples, 325 °C, 40% methane, 15% N <sub>2</sub> O, 3% H <sub>2</sub> O and 42% He .....	100
Figure 4.58. Activity test results of Micro-Cu-FER_1 after regeneration steps, 325 °C, 40% methane, 15% N <sub>2</sub> O, 3% H <sub>2</sub> O and 42% He .....	101
Figure 4.59. Activity test results of Micro-Cu-FER_3R after regeneration steps, 325 °C, 40% methane, 15% N <sub>2</sub> O, 3% H <sub>2</sub> O and 42% He .....	102
Figure 4.60. Activity test results of Micro-Cu-FER_1 with reactant or helium heating, 325 °C, 40% methane, 15% N <sub>2</sub> O, 3% H <sub>2</sub> O and 42% He.....	103
Figure 4.61. Activity test results of Micro-Cu-FER_1 after regenerations, 325 °C, 40% methane, 15% N <sub>2</sub> O, 3% H <sub>2</sub> O and 42% He.....	104

Figure 4.62. Activity test results of Micro-Cu-FER with different Cu/Al ratios, 325 °C, 40% methane, 15% N <sub>2</sub> O, 3% H <sub>2</sub> O and 42% He .....	105
Figure 4.63. Activity test results of Micro-Cu-SSZ-39 with different Cu/Al ratios, 325 °C, 40% methane, 15% N <sub>2</sub> O, 3% H <sub>2</sub> O and 42% He .....	106
Figure 4.64. Activity test results of Micro-Cu-SSZ-39_2 with respect to time....	107
Figure 4.65. Activity test results of Micro-Cu-SSZ-13 with different Cu/Al ratios, 325 °C, 40% methane, 15% N <sub>2</sub> O, 3% H <sub>2</sub> O and 42% He .....	108
Figure 4.66. Activity test results of Nano-Cu-FER with different Cu/Al ratios, 325 °C, 40% methane, 15% N <sub>2</sub> O, 3% H <sub>2</sub> O and 42% He .....	109
Figure 4.67. Activity test results of Micro-Cu-FER_1 with different H <sub>2</sub> O contents, 325 °C, 40% methane, 15% N <sub>2</sub> O, 0-9% H <sub>2</sub> O and 42% He.....	110
Figure 4.68. Activity test results of Nano-Cu-FER_1 with different H <sub>2</sub> O contents, 325 °C, 40% methane, 15% N <sub>2</sub> O, 0-9% H <sub>2</sub> O and 42% He.....	111
Figure 4.69. Activation energy plot of Nano-Cu-FER_1 a) MeOH and b) Methane .....	112
Figure 4.70 Activation energy plot of Nano-Cu-FER_2 a) MeOH and b) Methane .....	113
Figure 4.71. Activation energy plot of Micro-Cu-FER_1 a) MeOH and b) Methane .....	113
Figure 4.72. Activation energy plot of Micro-Cu-FER_2 a) MeOH and b) Methane .....	113
Figure 4.73. Activation energy plot of Micro-Cu-FER_3 a) MeOH and b) Methane .....	114
Figure A.1. Deconvoluted <sup>27</sup> Al and <sup>29</sup> Si MAS NMR of samples (a-b) Nano-Na <sup>+</sup> -FER, (c-d) Micro-NH <sub>4</sub> <sup>+</sup> -FER.....	139

## LIST OF ABBREVIATIONS

### ABBREVIATIONS

MTM	Methane to Methanol
MTO	Methane to Olefins
MTG	Methane to Gasoline
MMO	Methane Monooxygenase
DME	Dimethyl Ether
SDA	Structure Directing Agent
FTIR	Fourier Transform Infrared Spectroscopy
UV–Vis	Ultraviolet and Visible (UV–Vis) Spectroscopy
EXAFS	Extended X-Ray Absorption Fine Structure
XANES	X-Ray Absorption Near Edge Structure
XAS	X-Ray Absorption Spectroscopy
DFT	Density Functional Theory
XRD	X-Ray Diffraction
BJH	Barrett, Joyner, and Halenda Adsorption Model
ICP-OES	Inductively Coupled Plasma - Optical Emission Spectrometry
TEM	Transmission Electron Microscopy
SEM	Scanning Electron Microscopy
MAS NMR	Magic-Angle-Spinning Nuclear Magnetic Resonance
H <sub>2</sub> -TPR	H <sub>2</sub> -Temperature-Programmed Reduction

## LIST OF SYMBOLS

### SYMBOLS

T	Temperature, °C
P	Pressure, bar
$\lambda$	Wavelength, Å
d	Particle Size, nm
X	Conversion, %
S	Selectivity, %
r	Rate, $\mu\text{mol}/\text{g}_{\text{cat}}/\text{h}$
TOF	Turnover Frequency, mol CH <sub>3</sub> OH/mol Cu/h



## CHAPTER 1

### INTRODUCTION

#### 1.1 Methane as a Feedstock

Methane is a plentiful and economically feasible gas that serves as the raw material for a variety of large-molecule chemical compounds. Methane accounts for 70–90% of natural gas, making it a promising source of energy and chemicals. Given the current reliance on finite crude oil inventories for energy and chemical synthesis, many experts in the field consider it a transitional fuel for the twenty-first century [1], [2], [3]. Natural gas utilization has skyrocketed in recent years owing to the shale gas production technologies. The International Energy Outlook 2021 reference case found that global natural gas consumption was 4000 billion m<sup>3</sup> in 2020 [4]. Methane is classified as a greenhouse gas, and its emission into the atmosphere has negative implications including climate change. In 2023, the average global concentration of methane had reached to 1920 ppb [5]. It is especially concerning because methane has greater potential to cause global warming when compared to carbon dioxide, by a factor of 25 over a 100-year period [6]. This explains why methane is frequently burned to carbon dioxide in oil fields around the world, reducing its potency as a greenhouse gas as can be seen from Figure 1.1. Unfortunately, this method leads to the loss of a valuable potential feedstock. In 2022, the total amount of flared gas measured was 139 billion m<sup>3</sup>, with a market cost of around \$72 billion [7]. This emphasizes the importance of finding more effective and sustainable ways to handle methane and reduce its emissions.

The remote location of crude oil sources prevents the use of natural gas, and transporting the natural gas in gaseous form in pipes over long distances is impractical. Converting the natural gas into liquid form (by liquefaction) is also not a viable solution since methane's boiling point at atmospheric pressure is -164 °C,

and maintaining the liquid form at acceptable temperatures during transportation is not sustainable. Furthermore, methane is difficult to convert on-site due to its chemical inertness. Therefore, these processing constraints restrain the efficient methane utilization, resulting in its primary disposal via flaring [8].

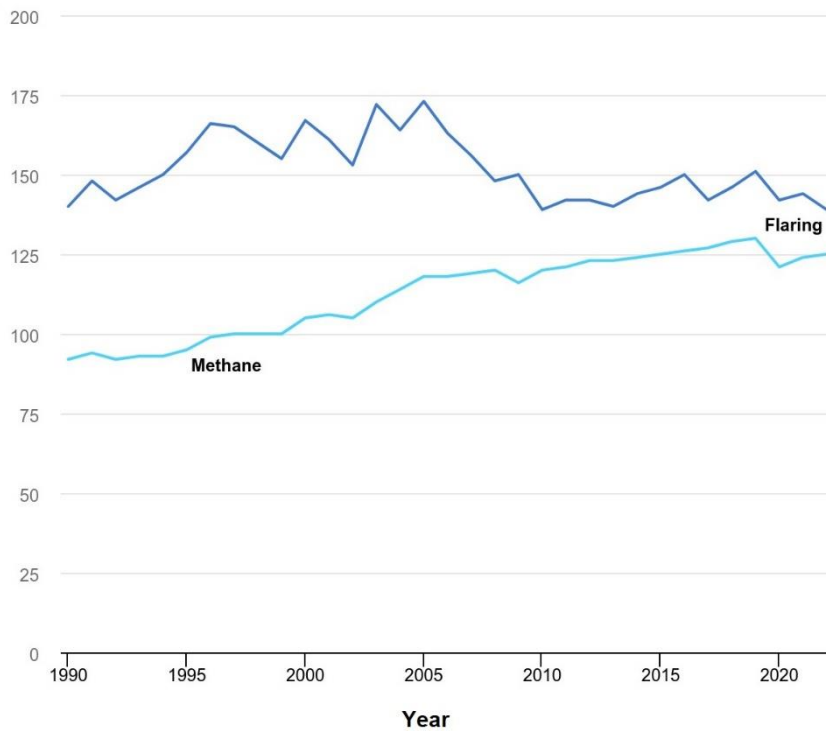


Figure 1.1. Global emissions coming from methane and methane flaring between 1990 and 2022 (units in bcm) [9]

Conventionally, two major ways are used for converting methane into liquid hydrocarbons: methane-to-gasoline and Fischer-Tropsch synthesis. Both processes use steam reforming to produce syngas, a mixture of carbon monoxide and hydrogen, as illustrated in Equations 1.1, 1.2, and 1.5. The syngas is then subsequently converted into the desired end products. Steam reformation is catalyzed by alumina-supported nickel and occurs at high temperatures of up to 1000 °C, resulting in large operating and maintenance costs. In a typical methane steam reforming plant, unreacted methane from the primary unit is fed into a secondary unit, which reforms it with oxygen and steam at even higher temperatures than the primary unit. The

resulting syngas can be catalytically converted into methanol, offering an indirect route for methane synthesis, as demonstrated in Equations 1.3 and 1.4.

To avoid the energy-intensive aspect of steam reforming, direct conversion of methane to methanol has been proposed as an alternative way. Researchers worldwide are interested in direct pathways involving the partial oxidation of methane to methanol, as shown in Equation 1.6. When compared to the standard steam reforming method, this strategy tries to simplify the process while also consuming less energy [10].

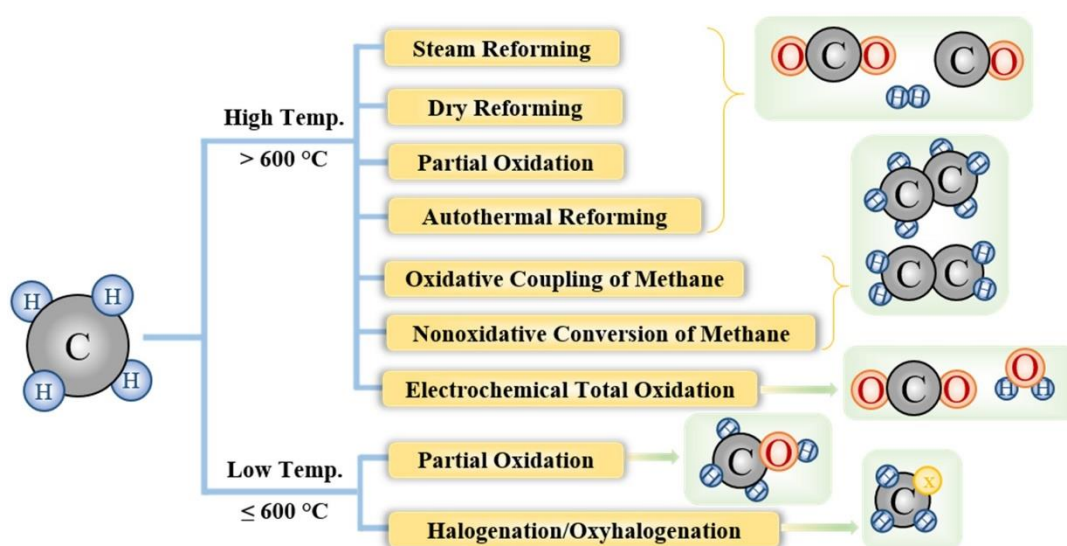


Figure 1.2. Methane conversion routes and end products [11]

In addition, methane can be transformed into a variety of valuable products using various chemical processes, as shown in Figure 1.2. However, the direct conversion of methane into methanol and its derivatives will be discussed for the purposes of this study. Methanol production is driven primarily by its importance as an essential industrial chemical since methanol is a critical feedstock in the chemical industry for the productions of formaldehyde, acetic acid, methyl tertiary butyl ether, an important gasoline additive that improves fuel performance, and dimethyl ether. Furthermore, methanol serves as a precursor to the manufacture of various other useful compounds, such as formaldehyde, and propylene [11]. Methanol-to-

hydrocarbons (MTH) research, which covers methanol-to-gasoline (MTG) and methanol-to-olefins (MTO) technology, has grown rapidly in recent years. It has been revealed that the catalyst and operation conditions influence the technology's selectivity to different types of hydrocarbons.

The capacity to efficiently convert methane into methanol and its derivatives holds great promise for extending natural gas applications and uses while also opening up new paths for the production of lucrative chemical goods. For more than a century, the academic and industrial sectors have been concerned about the waste of such a valuable resource. Hence, there is an increasing interest in discovering new techniques to extract valuable molecules from natural gas, as well as alternative strategies to maximize the potential of this abundant resource. Because it is difficult to comprehend, methane chemistry has earned the title of "Holy Grail of Catalysis" [12].

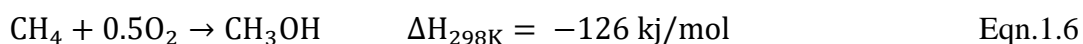
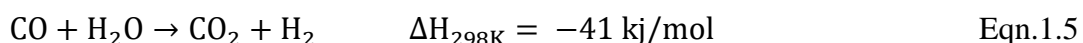
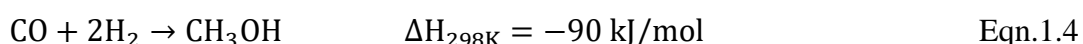
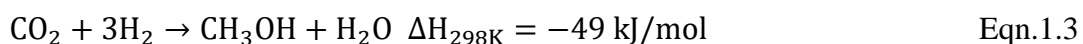
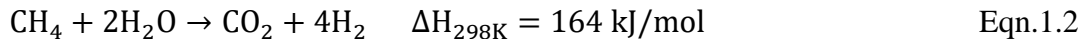
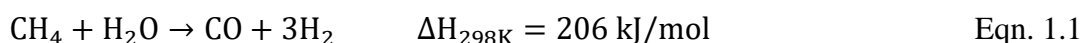
## **1.2 Methanol Production**

The global dependency on fossil fuels could be reduced by using cleaner alternative energy, methanol. Moreover, the carbon footprint of methane could be eliminated by the direct conversion of methane to methanol. Conventional techniques for producing methanol involve syngas, which is produced via gasifying of coal, steam reforming of methane or naphtha. Additionally, methane (natural gas) or carbon dioxide (CO<sub>2</sub>) can also be directly oxidized or reduced using hydrogen while producing methanol.

Despite having half the volumetric energy density (15.6 MJ/L) of gasoline (34.2 MJ/L) and diesel (38.6 MJ/L), methanol is useful since it can be used as a fuel or can be combined with gasoline to boost octane. The Environmental Protection Agency (EPA) approved the use of 15,000 methanol-powered automobiles in the 1990s, but the program was suspended due to rising natural gas prices. CRI and Geely have recently conducted pilot programs to relaunch methanol-powered automobiles in

Europe and China using green methanol derived from recycled CO<sub>2</sub>. At ambient temperature, methanol can also be used to generate electricity in a direct methanol fuel cell (DMFC), which reduces oxygen at the cathode to produce water and oxidizes methanol at the anode to make CO<sub>2</sub> [13].

Syngas is commonly used to produce methanol, and it comprises 2 to 8% CO<sub>2</sub> in a CO/CO<sub>2</sub>/H<sub>2</sub> stream. Methane steam reforming (Equations 1.1 and 1.2), naphtha steam reforming, and coal gasification are the primary sources of syngas. Depending on the source, the feed's CO/CO<sub>2</sub>/H<sub>2</sub> ratios vary. According to Equation 1.5, CO<sub>2</sub> is now added to syngas up to 30% of the total carbon content, while the water-gas shift reaction (WGS) balances the feed's H<sub>2</sub> concentration. CO<sub>2</sub> hydrogenates at a much higher rate than CO (Equation 1.3), hence adding CO<sub>2</sub> to syngas enhances methanol output [14].



### 1.3 Studies in The Literature and Industry on The Catalytic Methane to Methanol Conversion Process

Methane can be converted into methanol through two distinct pathways known as the indirect and direct methane to methanol (MTM) reactions as can be seen in Figure 1.3.

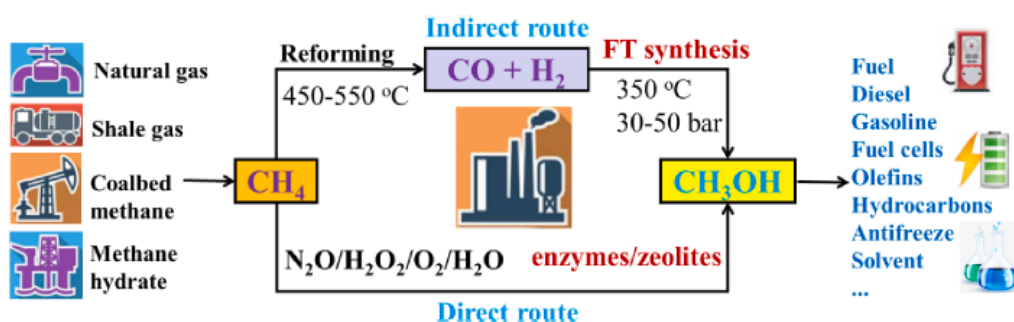


Figure 1.3. MTM production methods [15]

### 1.3.1 Indirect Methane to Methanol Conversion

The industrial process for converting methane to methanol primarily employs the indirect method, also referred to as the syngas route. In this syngas route, the conversion process occurs in two steps. Initially, methane is subjected to steam reforming at high temperatures (450–550 °C) and relatively high pressures (30 bar) using a Ni/Al<sub>2</sub>O<sub>3</sub> catalyst, resulting in the production of syngas. In the subsequent step, the syngas is transformed into methanol at high pressures (30–100 bar) and milder temperatures (250–350 °C) using a Cu/ZnO/Al<sub>2</sub>O<sub>3</sub> catalyst. The chemical reactions involved in these steps are represented in Equations 1.1, 1.2 and 1.4 respectively. However, the limited lifespan of Ni-supported catalysts under these reaction conditions poses a challenge despite the advantages of using them to prevent undesired coke formation during the process. Currently, the most economically viable approach for converting methane into valuable products is the syngas route, which typically achieves a high methanol selectivity of around 99%, yielding 65–75% of the desired product [10].

The current process of methane to methanol conversion using the syngas route is indeed energy-intensive, primarily due to the high operating temperatures and pressures involved. Additionally, the need for expensive heat transfer equipment contributes to the high capital costs, making this route economically viable only for large-scale production. One of the main drawbacks of this process is the low methanol selectivity at the high temperature and pressure operating conditions. This

means that a considerable amount of the methane can be transformed into undesirable byproducts, such as acetone or methyl ethyl ketone, which may be difficult to separate efficiently via distillation. Because of the high cost and energy requirements of industrial operations, there is a growing interest in developing alternative processes that can function in milder environments. This search is especially important for small-scale applications, where converting methane to methanol on-site is desirable. Methane flaring can be avoided by taking a more efficient and less energy-intensive strategy, and the produced methanol can be conveniently transported to where it is required [11].

### **1.3.2 Direct Methane to Methanol Conversion**

The direct MTM process converts  $\text{CH}_4$  directly into methanol, eliminating the need for additional production of syngas in the indirect industrial method. This partial oxidation of methane to methanol at modest temperatures is regarded as one of the most coveted achievements in chemical reactions. The reason is that activating methane and selectively producing methanol at lower temperatures present significant challenges in the field of catalysis and chemical engineering. MTM can be classified into two processes: stepwise and continuous, and stepwise process depicted in Figure 1.4. The stepwise method, also known as the chemical looping or 3-step process, involves three main stages. Firstly, the catalyst is activated at elevated temperatures (400–500 °C) using an oxidant to form active sites. Subsequently,  $\text{CH}_4$  reacts with the activated form of catalyst at milder temperatures (25–200 °C). Finally, the produced methanol needs to be extracted from the catalyst's surface due to the low reaction temperatures, requiring an additional extraction step using various solvents like acetonitrile solution or steam [16].

Copper exchanged zeolites have shown high methanol selectivity (>95%) using stepwise processes. However, the constant cooling and heating between different steps prolong the reaction time, and the extraction step may lead to product dilution, which is a drawback.

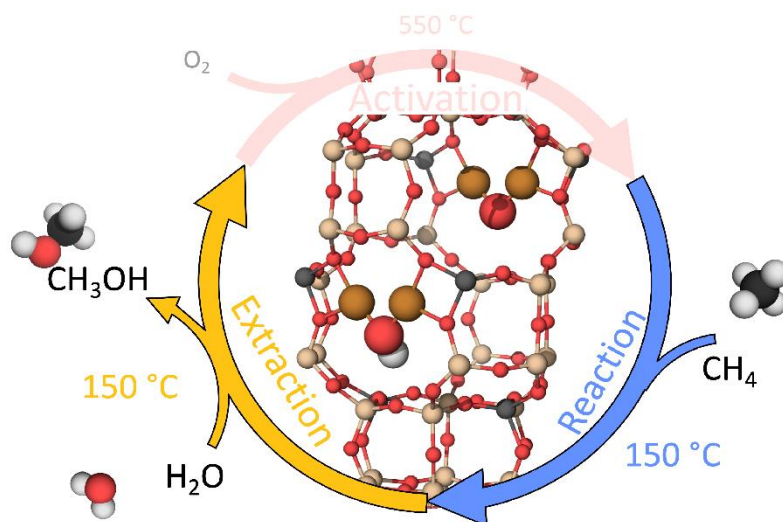


Figure 1.4. Stepwise MTM Process [17]

However, in the continuous catalytic process, the reactants, including the oxidant (N<sub>2</sub>O or O<sub>2</sub> or H<sub>2</sub>O<sub>2</sub>), CH<sub>4</sub>, and sometimes H<sub>2</sub>O, are fed at the same time into the catalyst bed. The reaction occurs in the gas phase at temperatures of 200–350 °C, eliminating the need for extraction and activation stages. However, direct methane to methanol process poses certain challenges [16].

#### 1.4 The Challenges in Direct Methane Conversion to Methanol

The partial oxidation of methane to methanol is hampered by two major barriers. The first problem is to break the C–H bond in methane. Because of its perfectly symmetrical tetrahedral structure, methane is a stable hydrocarbon. Because of its 440 kJ/mol dissociation energy, activating the methane C–H bond may require severe conditions. Secondly, retaining and isolating methanol as a product under such conditions is thermodynamically challenging. The dissociation energy of the C–H bond in methanol is roughly 47 kJ/mol lower than the C–H bond in methane [18].

The concern with direct methane conversion is that methane and its intermediates such as methoxy species can be oxidized to more thermodynamically favorable

molecules such as carbon monoxide (CO) and carbon dioxide (CO<sub>2</sub>), resulting in low selectivity of methanol. The choice of oxidant is also fundamental because it influences the reaction's kinetic energy barrier. Using O<sub>2</sub> as an oxidant for direct MTM requires more activation energy than other oxidizing agent, N<sub>2</sub>O and H<sub>2</sub>O<sub>2</sub>, which readily liberate O atoms. As a result, direct MTM with O<sub>2</sub> requires greater temperatures or pressures, which could cause overoxidation. On the other hand, using N<sub>2</sub>O as an oxidant may allow the selective synthesis of oxygenate products that cannot be formed with O<sub>2</sub> [16].

### **1.5 The Performance Targets for Feasibility of MTM**

In 1995, Foulds and Gray presented technical and economic evaluations of direct methane-to-methanol systems conducted in the late 1980s and early 1990s. This research found that having high methanol selectivity is more important than optimizing overall methane conversion [19]. The minimum conversion rate is estimated to be around 5%, with selectivity values of around 80% at 5% methane conversion and 70% at 10% conversion required for nearly similar performance compared to conventional procedures [20]. Another review performed by a prominent engineering contractor at the time suggested an even higher criterion of 95% selectivity at 10% conversion for a competitive process. An industrial analysis based on heat transfer cost indices revealed that a direct methane to methanol process with 2.5% methane conversion and 80% methanol selectivity would have capital costs that were approximately 15% higher than conventional methods, though this estimate is subject to some uncertainty [21]. More recently, Baliban et al. incorporated direct methane to methanol examples in comprehensive research that optimized several natural gasses to liquid fuel processes. In one scenario, a direct oxidation process with 13% methane conversion and 63% methanol selectivity, followed by methanol-to-gasoline (MTG) conversion, resulted in final gasoline product costs that were about 15% higher than steam reforming routes, even on a small scale of 1 kbd (thousand barrel per day) [22]. Examining the data reveals that

reaching a higher selectivity of around 75% will result in roughly the same expenses, which is consistent with Foulds and Gray's previous findings.

These performance requirements pose substantial obstacles, but it is critical to recognize the potential for inventive process engineering to overcome the apparent disadvantages of direct conversion methods. However, it is clear that in order to compete with proven techniques targeting traditional methanol markets, a high selectivity of roughly 75% with considerable once-through conversions (equivalent to or greater than 5%) will be required. In practice, something higher than this amount is likely to be necessary to provide a compelling incentive for significant advances in catalytic process development. These targets exceed the performance levels obtained thus far with molecular oxygen as the oxidant, implying that a successful system will require features that prevent further oxidation of the methanol product. This is critical since methanol is widely regarded as far more reactive than methane feedstock [23].

The selective partial oxidation of methane to methanol with molecular oxygen is a very exothermic reaction (Equation 1.6). The process is slightly more exothermic than producing methanol from syngas (see Equation 1.4), but substantially less than Fischer-Tropsch synthesis ( $\text{CO} + 2\text{H}_2 \rightarrow \text{-(CH}_2\text{)-} + \text{H}_2\text{O}$ , with  $\Delta H$  ranging from -150 to -160  $\text{kJ mol}^{-1}$  for typical products). However, the undesired productions of CO or  $\text{CO}_2$  during the process dramatically increase the heat release. For instance, the partial oxidation of methane to methanol is approximately 70% more exothermic than Fischer-Tropsch synthesis, even with 20% selectivity to  $\text{CO}_2$ . Therefore, achieving high  $\text{CH}_3\text{OH}$  selectivity is crucial for managing heat release in reaction systems, especially when seeking for comparable efficiencies of  $\text{CH}_3\text{OH}$  production to industrial Fischer-Tropsch synthesis [23].

When considering systems that use molecular oxygen, it is critical to consider the selectivity of oxygen usage. For example, if only one oxygen atom from the  $\text{O}_2$  molecule is integrated into the methanol product (similar to the well-known methane monooxygenase system) and there is no other sacrificial reductant, the maximum

theoretical methanol selectivity is 80% ( $5\text{CH}_4 + 4\text{O}_2 \rightarrow 4\text{CH}_3\text{OH} + \text{CO}_2 + 2\text{H}_2\text{O}$ ). To overcome this limitation and obtain more selectivity, techniques for incorporating both oxygen atoms into the methanol product must be developed. On the other hand, methane can be selectively converted to formaldehyde or acetic acid, both of which are important industrial methanol derivatives, with only 50% oxygen selectivity [22].

## 1.6 The Types of Catalyst Used in MTM

It was discovered that the direct conversion of methane to methanol at room temperature using  $\text{O}_2$  is mediated by methane monooxygenase. The main feature of these enzymes is that they contain copper and iron in their structure. These copper and iron structures were found to be produced by forming Cu/Fe-oxo clusters. Since it is very difficult to adapt these natural enzymes to the industrial structure, catalysts are needed. Although iron catalysts are also included in the literature, studies have focused on copper-zeolite catalysts in the recent period due to their high selectivity values [24], [25]. Structures formed by copper zeolites with zeolite and enzyme with copper can be seen in Figure 1.5. Zeolites are microporous aluminosilicate minerals with negative charges that serve as anchoring sites for metal cations, resulting in Cu-oxo patterns after thermal treatment. Because of the spatial confinement properties of zeolites, multiple Cu-oxo motifs with varying coordination structures and geometries can be well stabilized in small size. Furthermore, the stable structure of zeolites can effectively shield the active Cu-oxo sites on the framework from the severe reaction conditions (for example, hydrothermal) [26]. For decades, copper exchanged zeolites have been extensively researched and used in selective  $\text{CH}_4$  oxidation to methanol [27].

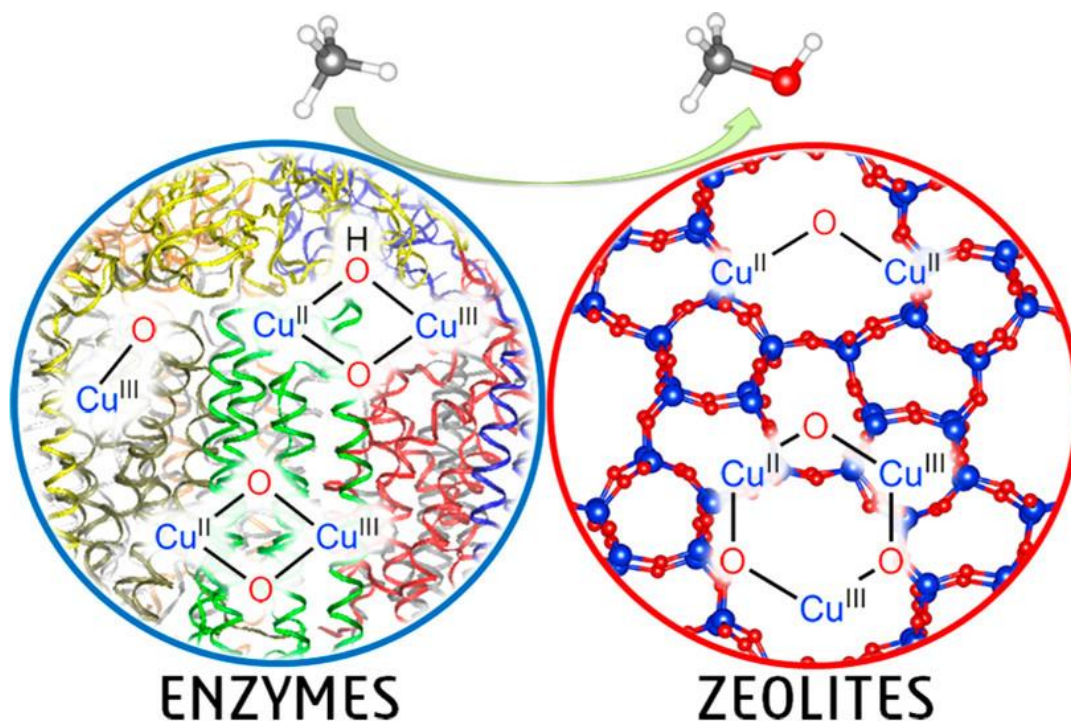


Figure 1.5. Enzymes and zeolites active center representation [28]

## 1.7 Zeolites

Zeolites are solid and crystalline inorganic compounds having a microporous structure. These materials are composed of TO<sub>4</sub> tetrahedra, with T representing elements such as Si, Al, P, Ge, and B, among others. The structure of zeolites consists of very small channels and cavities with diameters ranging from 0.3 to 1.5 nanometers. When heated rapidly, zeolites release water and display characteristics that interested the Swedish mineralogist A.F. Cronstedt, who discovered zeolites in 1756 [29]. He used the term 'zeolite', which means 'stones that boil' since the word zeolite is derived from the Greek words "zeo" and "lithos". These minerals, which are predominantly silicates, can be found naturally in volcanic locations, alkaline desert lake sediments and soils, and marine sediments [30].

There are roughly 45 known natural zeolites, but their limited structures and compositions, combined with the presence of contaminants, limit their commercial

applications to animal feed, pet litter, and water filtration. Nonetheless, there have been descriptions of alternative applications. Industrial processes such as adsorption, ion-exchange, and catalysis primarily use synthetic zeolite materials. These synthetic zeolites are exceedingly pure, with well-defined compositions and pore sizes. The International Zeolite Association's database currently includes over 250 distinct zeolite structures [31].

Zeolites play an important role in our daily lives and are widely used as sorbents and ion-exchangers in detergents. They also play an important role as industrial catalysts in the production of liquid fuels and intermediates for a variety of industries such as petrochemicals, chemical, and pharmaceutical [32]. Zeolites stand out for their outstanding physicochemical features and great usefulness. Furthermore, they have the additional benefit of being ecologically friendly, safe, and sustainable, making them a popular choice for a variety of applications as 'green' alternatives. For example, they can replace chlorine in swimming pools, polyphosphates in detergents, and mineral acids such as hydrochloric, hydrofluoric, or sulfuric acid in a variety of catalytic industrial processes [33], [34].

### **1.7.1 Synthesis of Zeolites**

Zeolites are typically synthesized hydrothermally in a gel employing inorganic cations (such as  $\text{Na}^+$ ,  $\text{K}^+$ , and  $\text{Li}^+$ ) or organic amines/ammonium cations (e.g., tetramethylammonium; TMA, tetraethylammonium; TEA, tetrapropylammonium; TPA) as structure guiding agents. These SDAs play an important function in determining the creation of particular zeolite structures [35], [36], [37]. The gel combination includes sources of tetrahedral atoms (e.g., Al, Si), SDA, and mineralizer ( $\text{OH}^-$ ). This combination is subsequently heated under autogenous pressure in a Teflon-lined stainless-steel autoclave for a set period of time, typically at temperatures ranging from 373 K to 523 K [33], [36], [37], [38]. Several parameters influence the synthetic process and zeolite formation, including source material selection, gel aging, solvent type, gel composition, pH value, and

crystallization temperature and duration. In this investigation, various structure-directing agents were used to create ideal zeolites. FER zeolite was manufactured using piperidine, whereas SSZ-13 zeolite was synthesized using trimethyladamantylammonium hydroxide. Finally, tetramethylpiperidinium hydroxide was used to synthesize SSZ-39 zeolite [39], [40], [41], [42].

### **1.7.2 Structure of Zeolites**

All zeolite frameworks are formed by joining primary building units (PBU), also known as tetrahedra ( $TO_4$ ), in a repeating pattern. Secondary building units (SBU) are more complex building blocks constructed by joining multiple PBUs together, such as tetrahedral rings with four and six members (4MR, 6MR, respectively). Additionally, composite building units (CBUs) such as double-six-membered rings (d6MRs) are formed by assembling various types of SBUs. The arrangement of these building units dictates the specific zeolite structure that emerges, and they play an important role in controlling the crystallization process [43].

Zeolites with small pores, including 6-membered rings (6MR) and 8-membered rings (8MR), with pore diameters ranging from 0.25 to 0.45 nanometers. Medium pore zeolites with 10-membered rings (10MR) have pore diameters ranging from 0.45 to 0.60 nanometers, whereas big pore zeolites with 12-membered rings (12MR) have pore sizes of 0.6 to 0.8 nanometers [41]. Micropores in zeolites can take the shape of interconnecting channels or cages, resulting in a multidimensional porous structure. The variety in pore size and shape in zeolites allows for shape-selective catalysis, which implies that the reaction's product distribution is determined by the shape and size of molecules that may fit into the pores. This distinguishing feature of zeolites plays an important role in determining the results of various reactions [44].

### **1.7.3 Si/Al Ratio of Zeolites**

The Si/Al ratio is a major characteristic for zeolites because Al content influences cation exchange capability while Si content impacts thermal stability. Thus, when the Si/Al ratio increases, zeolites lose ion-exchange capability but gain thermal stability. These features influence zeolites' applications. For example, low Si/Al ratio zeolites have a high ion-exchange capacity, making them an ideal ingredient for detergent applications. Zeolites with rich Si are employed in catalysis because of their distinctive features, including ion-exchange capacity, large pore volume, high surface area, crystallinity, strong acidity, high thermal stability, and variable pore diameters in zeolites. The Si/Al ratio also affects the relationship between H<sub>2</sub>O and zeolite [45].

### **1.7.4 Brønsted Acidity of Zeolites**

Zeolites include two types of acid sites: Brønsted and Lewis. Brønsted acid sites are produced by bridging hydroxyl groups with framework Si and Al, while extra-framework cations mostly operate as Lewis acid sites [46]. The acidity of a zeolite is an important property that may be regulated using the Si/Al ratio. Increasing the Si/Al ratio of a zeolite leads to decreasing Al content, which is directly proportional to Brønsted acidity [47]. Two zeolites with similar Si/Al ratios may have varying Brønsted acidity because to their distinct frameworks [48].

## **1.8 Zeolites Used in This Study**

Three different zeolite framework types of FER, AEI and CHA were used in this study.

### 1.8.1 FER (Ferrierite)

Ferrierite (FER) zeolite is an industrialized zeolite with effective catalytic capabilities employed in skeletal isomerization of n-alkene, methanol to olefin conversion, N<sub>2</sub>O breakdown, CO<sub>2</sub> hydrogenation, methanol or ethanol dehydration, and dimethyl ether carbonylation. FER is a medium-pored zeolite with two vertically intersecting channels. There are two channels: an 8-membered ring (MR) channel ( $3.4 \times 5.4 \text{ \AA}$ ) along the [010] direction, and a 10-membered ring (10-MR) channel ( $4.3 \times 5.5 \text{ \AA}$ ) along the [001] direction and frame density of  $17.6 \text{ T}/1000 \text{ \AA}^3$ . Many efforts have been made in recent decades to synthesize and modify FER zeolites, as FER zeolite is industrially used in the skeletal isomerization of n-butene. As a result, FER zeolites with varying basic composition, shape, hierarchical structure, acid strength, and catalytic characteristics have been effectively synthesized utilizing various methods [49], [50]. Figure 1.6 shows the framework structure of FER zeolite [51].

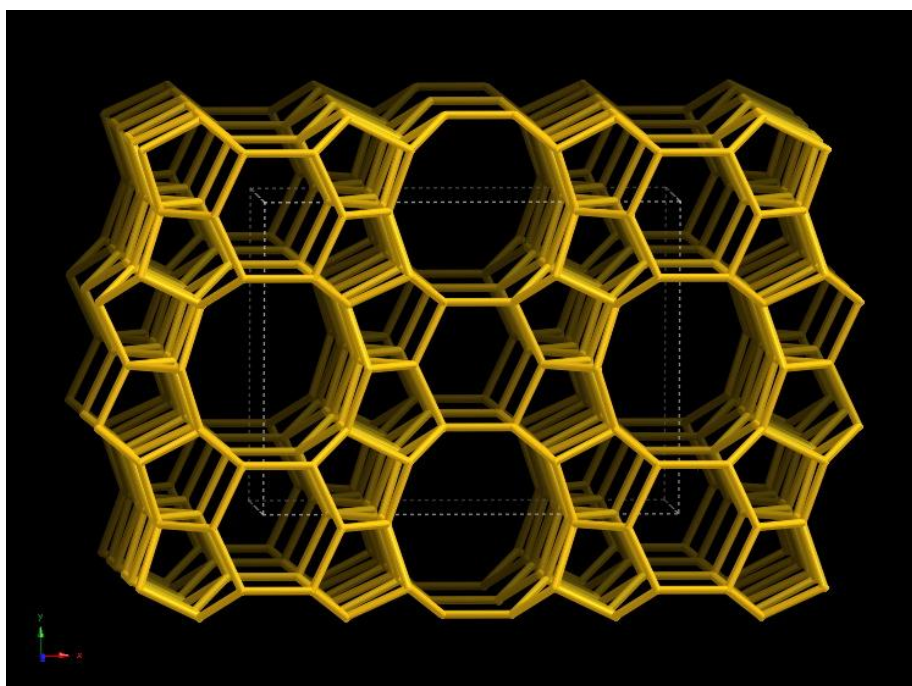


Figure 1.6. FER Framework viewed along [001] [51]

### 1.8.2 AEI (SSZ-39)

SSZ-39 is an AEI-type zeolite with an orthorhombic structure and  $Cmcm$  space group. Its unit cell dimensions are  $a=13.6770\text{\AA}$ ,  $b=12.6070\text{\AA}$ , and  $c=18.4970\text{\AA}$ , with a frame density of 15.1 T atoms per  $1000\text{\AA}^3$ . The framework structure is linked to the three-dimensional 8-membered ring channel system via a binary six-membered ring (6-MR) unit, resulting in the AEI lattice [52]. Figure 1.7 illustrates a uniform pore with a diameter of  $3.8 \times 3.8\text{\AA}$  [53]. Both CHA and AEI kinds have the same channel size, but AEI's cavities are pear-shaped cages. AEI-type zeolites have a surface area of  $499\text{ m}^2\text{g}^{-1}$  and a total pore volume of  $0.27\text{ cm}^3\text{g}^{-1}$ , with  $0.20\text{ cm}^3\text{g}^{-1}$  being microporous. Zones et al. first synthesized SSZ-39 in 1997, and it has subsequently been used in a variety of catalytic applications including selective catalytic reduction of  $\text{NO}_x$ , methanol to olefins, methane to methanol, and ethane conversion processes [52], [54], [55].

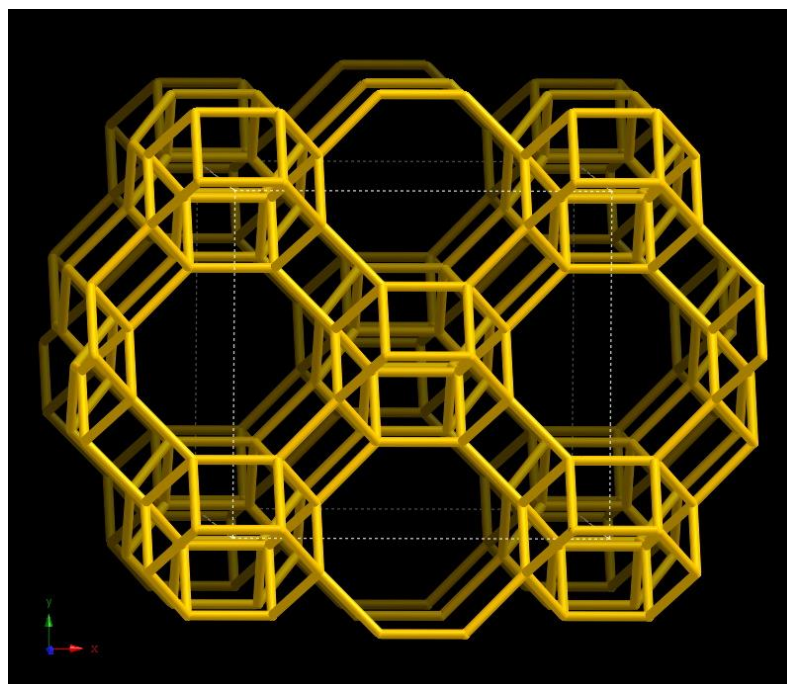


Figure 1.7. AEI Framework viewed along [001] [53]

### 1.8.3 CHA (SSZ-13)

SSZ-13 belongs to the CHA type zeolite family. It has a rhombohedral structure with R-3m space group and unit cell dimensions of  $a=13.6750 \text{ \AA}$ ,  $b=13.6750 \text{ \AA}$ , and  $c=14.7670 \text{ \AA}$ . The framework density is  $15.1 \text{ T atoms}/1000 \text{ \AA}^3$  [56]. The zeolite is identified by layers of double six-membered rings (6-MR) connected by four-membered rings. CHA zeolite has a three-dimensional pore system with ellipsoidal-shaped big cages and eight-membered ring apertures of roughly  $(3.8 \times 3.8 \text{ \AA})$  (as seen in Figure 1.8) [56], [57]. SSZ-13 has a BET surface area of about  $710 \text{ m}^2\text{g}^{-1}$  and a micropore volume of  $0.25\text{--}0.30 \text{ cm}^3\text{g}^{-1}$  [58]. Its unusual combination of small pores and relatively large cavities makes it extremely appealing due to its strong physiochemical capabilities and outstanding potential as a catalyst for a variety of applications. Notably, it has potential as a catalyst for the  $\text{NH}_3$ -SCR process and the catalytic conversion of methane to methanol. These characteristics have sparked substantial interest in the scientific community [59].

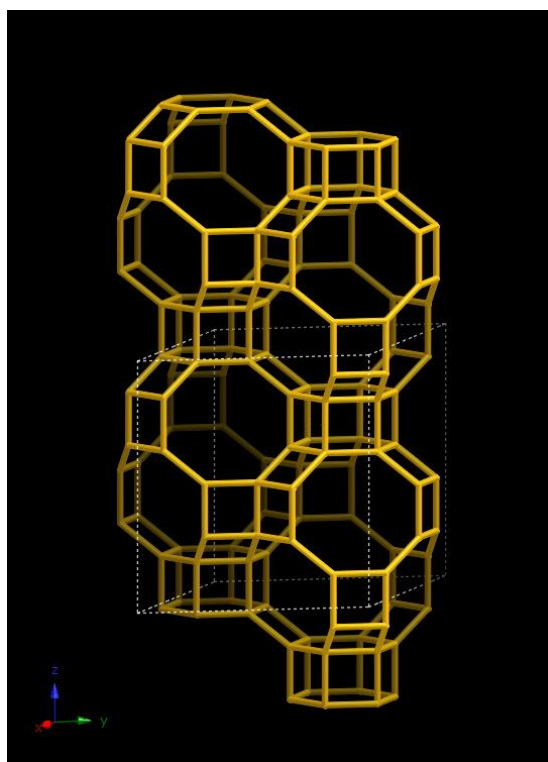


Figure 1.8. AEI Framework viewed along [001] [56]

## 1.9 The Objective of This Study

The scope of this study is to produce methanol from methane using continuous MTM process using  $\text{N}_2\text{O}$  as oxidizing agent with the aims of achieving methanol selectivity similar to stepwise MTM process (~85%) and increasing methanol production rate higher than  $500 \mu\text{mol}\cdot\text{h}^{-1}\text{g}^{-1}$  at atmospheric pressure and at temperature ranges of 310–325 °C. In this work, copper-exchanged zeolites are studied to improve  $\text{CH}_3\text{OH}$  selectivity and to prevent the overoxidation of methane to CO and  $\text{CO}_2$ . Additionally, the effects of Cu/Al molar ratio (ranging from 0.02 to 0.35), zeolite framework type (FER, AEI, CHA) and  $\text{H}_2\text{O}$  concentration in the feed stream (0 to 9%) on  $\text{CH}_3\text{OH}$  production and selectivity during the continuous MTM process are investigated. Lastly, nano-sized and mesoporous FER zeolites are synthesized by hydrothermal method to investigate the zeolite structure effect on MTM process since the highest performance is observed over FER zeolites.



## CHAPTER 2

### LITERATURE REVIEW

In this section, the identification of active sites, their possible formation process, catalytic activity test results and reaction mechanism in the latest literature are included and it is focused on copper exchanged zeolites.

#### 2.1 The Types, Identification and Formation of Cu Active Sites

Zeolites with different frameworks of MFI, CHA, MOR, AEI and FER have specific structure properties, including ring sizes, channel sizes and the distributions of Al sites. These properties are significant while determining the Cu active sites of the coordination structure in Cu-exchanged zeolites. The zeolite frameworks exhibit a variety of Cu<sup>2+</sup> coordination structures composed of monocopper, single Cu<sup>2+</sup> ions and multi-copper oxo clusters. Determining and understanding the coordination structures of copper motifs that serve as active sites in MTM reactions is still challenging. Recently, copper active sites and coordination structures in zeolites have been defined using ex-situ and in-situ spectroscopy studies as well as theoretical calculations, which contain valuable information. Therefore, Cu-zeolites with well-defined coordination structures of Cu active sites can be successfully prepared and good catalytic performance in MTM can be achieved. In this section, description of how these active sites are identified by different techniques, especially UV–Vis, and how active sites are formed will be provided.

##### 2.1.1 The Identification of The Types of Cu Active Sites

Recently, Cu-exchanged zeolites have been broadly examined with emphasis on the identification of Cu active sites due to their potential for direct MTM reactions. In

order to summarize, Cu active sites and the coordination structure of these sites are given in Table 2.1.  $\text{Cu}_x\text{O}_y$  clusters in zeolites have been demonstrated to be active species for MTM process since they activated C–H bonds of methane. Groothaert et al. found  $\text{Cu}_x\text{O}_y$  clusters in ZSM-5 using UV–Vis and Raman spectroscopy analyses [60], [61]. They showed the presence of bis( $\mu$ -oxo)dicopper  $[\text{Cu}_2(\mu\text{-O})_2]^{2+}$  active species by the existence UV–Vis absorption bands at  $\sim 22700\text{ cm}^{-1}$  of the Cu/ZSM-5 sample that was activated by  $\text{O}_2$ . Additionally, they mentioned that mono( $\mu$ -oxo)dicopper  $[\text{Cu}_2^{\text{II}}(\mu\text{-O})]^{2+}$  species were active in MTM process according to the results of Raman spectroscopy, exhibiting bands at  $456\text{ cm}^{-1}$ ,  $870\text{ cm}^{-1}$ , and  $1725\text{ cm}^{-1}$ . Moreover, the bands of bis( $\mu$ -oxo) ( $[\text{Cu}_2(\mu\text{-O})_2]^{2+}$ ) and superoxo species ( $[\text{Cu}(\eta^2\text{-O}_2)]^{2+}$ ), located at  $600\text{ cm}^{-1}$  and  $1100\text{ cm}^{-1}$ , were not found in Raman spectroscopy results, which was attributed to the possibility that they were not active sites of Cu/ZSM-5 for MTM process [62]. Li et al. also suggested  $[\text{Cu}_2^{\text{II}}(\text{O}_2)]^{2+}$  and  $[\text{Cu}_2^{\text{II}}(\mu\text{-O})]^{2+}$  species in Cu-exchanged ZSM-5 as the active sites for MTM process according to the theoretical calculations [63] and the  $\mu$ -( $\eta^2$ - $\eta^2$ )peroxodicopper  $[\text{Cu}_2^{\text{II}}(\text{O}_2)]^{2+}$  species were found to be the precursor of  $[\text{Cu}_2^{\text{II}}(\mu\text{-O})]^{2+}$  motif according to UV–Vis spectroscopy [64]. Moreover, copper-oxo clusters  $[\text{Cu}_3(\mu\text{-O})_3]^{2+}$  were also suggested as active sites of Cu/ZSM-5 for MTM process using EXAFS and DFT studies [65], [66]. Recently, Tang et al. used a low-damage HAADF-STEM imaging technique to verify the presences of mono-Cu and multi-Cu species ( $[\text{Cu}_2(\mu\text{-O})]^{2+}$ ,  $[\text{Cu}_3(\mu\text{-O})_3]^{2+}$  motifs) in Cu-ZSM-5 [67].

Recent studies exhibited that dicopper oxo clusters could be stabilized in small-pore zeolite structures like AEI and CHA.

In Cu-modified CHA zeolites, Tsuchimura et al. found that mono( $\mu$ -oxo)dicopper species are responsible for direct conversion of methane to methanol using in situ UV–Vis spectroscopy [68].

Ipek et al. identified trans- $\mu$ -1,2-peroxo copper(II) ( $[\text{Cu}_2(\text{O})_2]^{2+}$ ) sites after  $\text{O}_2$  activation in Cu/SSZ-13 and Cu/SSZ-39 zeolites by in-situ Raman spectroscopy. Upon activation of Cu/SSZ-13 zeolite using  $\text{O}_2$ , vibrational bands at 360, 510, 580,

and  $837\text{ cm}^{-1}$  are formed indicating the presence of  $[\text{Cu}_2(\text{trans-}\mu\text{-1,2-O}_2)]^{2+}$  motifs. Nevertheless, these motifs were unstable due to decreased Raman intensity after a long period at room temperature. Additionally, they also found mono( $\mu$ -oxo)dicopper  $[\text{Cu}_2^{\text{II}}(\mu\text{-O})]^{2+}$  species that were more stable than  $[\text{Cu}_2(\text{trans-}\mu\text{-1,2-O}_2)]^{2+}$  species, as demonstrated by the distinctive Raman band at  $617\text{ cm}^{-1}$  [69].

Table 2.1. Cu active sites and coordination structures

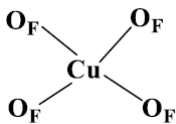
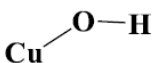
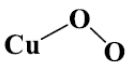
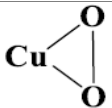
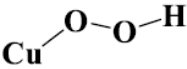
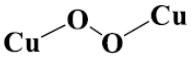
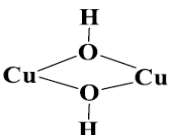
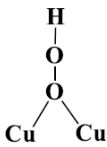
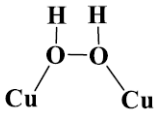
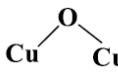
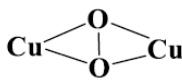
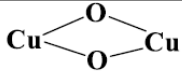
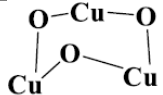
Active Sites	Structure	UV-Vis Band $\text{cm}^{-1}$	References
Bare Cu(II)		13 600-20 000	[70], [71]
Monocopper $[\text{Cu(II)OH}]^+$		41 000	[72], [73]
$\eta^1$ -superoxo copper(II) $[\text{CuOO}]^+$		n.a	[62], [74]
$\eta^2$ -superoxo copper(II) $[\text{CuOO}]^+$		n.a	[62], [75]
$\eta^1$ -hydroperoxo copper(II) $[\text{CuOOH}]^+$		n.a	[62], [74]
Trans- $\mu$ -1,2-peroxo dicopper(II) $[\text{Cu}_2(\mu\text{-O})_2]^{2+}$		n.a	[69], [76]
Bis( $\mu$ -hydroxy) dicopper(III) $[\text{Cu}_2(\mu\text{-OH})_2]^{2+}$		n.a	[74], [77]

Table 2.1. Cu active sites and coordination structures (Continued)

Active Sites	Structure	UV-Vis Band $\text{cm}^{-1}$	References
$\mu$ -1,1-hydroperoxo dicopper(II) $[\text{Cu}_2(\mu\text{-OOH})]^{2+}$		n.a	[74]
Bis( $\mu$ -hydroxo) dicopper $[\text{Cu}_2(\mu\text{-OH})_2]^{2+}$		32 000- 30 000	[78]
Mono( $\mu$ -oxo) dicopper $[\text{Cu}_2(\mu\text{-oxo})]^{2+}$		22 700	[68]
$\mu$ -( $\eta^2:\eta^2$ ) peroxo dicopper(II) $[\text{Cu}_2(\mu\text{-O})_2]^{2+}$		29 000-27 000	[62], [64]
Bis( $\mu$ -oxo) dicopper(III) $[\text{Cu}_2(\mu\text{-O})_2]^{2+}$		32 700	[60], [61]
Trinuclear Cu-oxo cluster $[\text{Cu}_3(\mu\text{-O})_3]^{2+}$		31000	[65], [66]

Guo et al. ascribed the bis( $\mu$ -oxo)dicopper  $[\text{Cu}_2(\mu\text{-O})_2]^{2+}$  motifs, confined in SSZ-13, as active sites for MTM process as shown by Raman band at  $\approx 610 \text{ cm}^{-1}$  (with 532 nm laser source) [79]. However,  $[\text{Cu}_2^{\text{II}}(\mu\text{-O})]^{2+}$  motif with a Cu–O–Cu angle of  $100^\circ$  also exhibited Raman band at  $\approx 609 \text{ cm}^{-1}$ , thereby the ascription of bis( $\mu$ -oxo)dicopper  $[\text{Cu}_2(\mu\text{-O})_2]^{2+}$  motifs was unclear [62].

It has been reported that binuclear and trinuclear copper-oxo complexes as active sites for the MTM process were probably present in large porous zeolites such as MOR and MAZ. Vanelderen et al. found two  $[\text{Cu}_2^{\text{II}}(\mu\text{-O})]^{2+}$  motifs in MOR zeolite with similar coordination structure. These motifs were responsible for the activation of C–H bond of methane, as shown by Raman and UV–Vis analyses [80].

Sushkevich et al. revealed that the micropores in MOR zeolites (i.e. 8 MR) could maintain a stable coordination structure of  $[\text{Cu}_2^{\text{II}}(\mu\text{-O})]^{2+}$ , which is the active sites in the selective anaerobic oxidation of MTM using  $\text{H}_2\text{O}$  as oxygen source. This was proven by in-situ IR, where the interaction of methane with  $[\text{Cu}_2^{\text{II}}(\mu\text{-O})]^{2+}$  sites produced bands corresponding to  $\text{CH}_3\text{O}$  and  $\text{CH}_3\text{OH}$  species, as well as  $\text{Cu}^+$  formation by  $\text{Cu}^{2+}$  reduction [81]. On the other hand, Vilella et al. reported that trans- $\mu$ -1,2-peroxo Cu complexes exhibited the highest stable coordination structure in MFI and MOR zeolites having larger ring sizes of 10 MR and 12 MR as a result of theoretical calculations [76].

Zheng et al. and Mahyuddin et al. suggested that tricopper clusters ( $[\text{Cu}_3(\mu\text{-O})_3]^{2+}$  motifs) were the possible active sites for low-temperature MTM process and these clusters could be stabilized in MOR zeolites according to DFT calculations, spectroscopic and kinetic studies [82], [83].

Theoretical analysis suggested that Cu-zeolites could form bigger multicopper clusters due to their thermodynamic stability and multicopper clusters become more stable as their size increases due to stable Cu-O connections. Researchers hypothesized that bigger multicopper clusters in MOR zeolite, such as  $[\text{Cu}_4\text{O}_4]^{2+}$ ,  $[\text{Cu}_5\text{O}_5]^{2+}$ , or  $[\text{Cu}_6\text{O}_7]^{2+}$  species, could be active sites for MTM process. However, the experimental proof has not yet been reported [84], [85], [86].

UV-Vis, FTIR and XAS and DFT studies proposed that monocopper  $[\text{Cu}(\text{II})\text{OH}]^+$  and bare monocopper Cu(II) motifs in the zeolite rings could be the active sites for MTM process [73], [87], [88]. Monocopper ( $[\text{Cu}(\text{II})\text{OH}]^+$ ) motifs are generally found in ring frameworks having a single Al site, while bare monocopper Cu(II) motifs are typically found in small zeolite rings (i.e. 6 MR). These motifs can be identified using FTIR and  $\text{H}_2$ -TPR analyses. For instance, FTIR spectra of Cu/SSZ-13 revealed two bands at 900 and 950  $\text{cm}^{-1}$  in the T-O-T bond vibration region, where T is Si or Al. These bands corresponded to the bare single Cu(II) site on 6 MR and the  $[\text{Cu}(\text{II})\text{OH}]^+$  site on 8 MR. Moreover, the two forms of monocopper(II) motifs interact differently with zeolite frameworks, resulting in varying  $\text{Cu}^{2+}$  reduction

capacities; therefore, H<sub>2</sub>-TPR profiles show these two different monocopper sites at different reduction temperatures. For instance, bare Cu(II) site on 6 MR had a higher reduction temperature of ~350 °C than [Cu(II)OH]<sup>+</sup> site on 8 MR with the reduction temperature of ~210°C due to stronger interaction [72].

Sushkevich et al. also indicated that the two interacting [Cu(II)OH]<sup>+</sup> sites in MOR zeolite could be active sites for methane activation. The formation of these sites after using high Si/Al ratio resulted in improved production of methanol as shown by in-situ NMR and IR studies [89]. On one hand, Sun et al. suggested that [Cu(II)OH]<sup>+</sup> sites in CHA were formed from bare Cu(II), [Cu<sub>2</sub>(μ-O)]<sup>2+</sup> and [Cu<sub>2</sub>(μ-O)<sub>2</sub>]<sup>2+</sup> sites by hydrolysis, thus promoting the activity of MTM process [90]. On the other hand, several researchers proposed that [Cu(II)OH]<sup>+</sup> species were only the precursor of [Cu<sub>2</sub>(μ-O)]<sup>2+</sup> and [Cu<sub>2</sub>(μ-O)<sub>2</sub>]<sup>2+</sup> sites not the active sites [71].

Furthermore, some studies proposed that the bare monocopper(II) or copper single-atom sites on two Al sites in 6 MR of ZSM-5 and SSZ-13 could be the active sites in MTM processes [70], [73]. For instance, Zhou et al. found that the bare Cu(II) sites located at 6 MR in Cu/SSZ-13, identified by in-situ UV–Vis bands at 13600–20000 cm<sup>-1</sup>, was the active sites in continuous MTM process, since these sites disappeared after introducing methane and steam [73]. Nevertheless, Ipek et al. stated that the bare Cu(II) sites in SSZ-13 and SSZ-39, identified by UV–Vis bands at 13600, 16600, and 20000 cm<sup>-1</sup>, were inactive species in stepwise MTM [69], [91], while Knorpp et al. proposed that the bare Cu(II) site in 6 MR from Cu-Omega (Cu-MAZ) was not reactive to methane [92].

On the investigation of the dicopper active sites in zeolite structure, Woertink et al. identified the coordination structure of [Cu<sub>2</sub><sup>II</sup>(μ-O)]<sup>2+</sup> motifs in ZSM-5 (located on 10 MR) as active sites in the form of two Cu atoms (Cu···Cu distance of 3.29 Å, < Cu–O–Cu of 139°) aligned with O atoms near Al sites and shared a bridging O atom. In addition to ZSM-5, they also examined the coordination structure of [Cu<sub>2</sub><sup>II</sup>(μ-O)]<sup>2+</sup> motifs in MOR, and proposed that the coordination structure was linked to the barrier

of motifs in activating C–H bonds of methane using cluster-modelled DFT calculations and spectroscopy studies [62].

Mahyuddin et al. elucidated additional coordination mechanisms for  $[\text{Cu}_2^{\text{II}}(\mu\text{-O})]^{2+}$  motifs of Cu/MOR. The coordination chemistry of these motifs caused varying Cu–O–Cu angles, which further impacted the activation of C–H bond of methane due to the repulsive interaction between methane and  $[\text{Cu}_2^{\text{II}}(\mu\text{-O})]^{2+}$  site [82]. According to the literature, the decrease in Cu–O–Cu angle promoted methane activation and lowered the energy required to dissociate C–H bonds. For instance, Decreasing the Cu–O–Cu angle from 134.2 ° to 84.1 ° due to varied coordination environments led to a decrease in required C–H bond dissociation energy from 68.1 to 45.1 kJ/mol [93]. Additionally, one study also emphasized that decreasing both Cu–O–Cu angle and Cu–Cu distance could enhance the conversion of methane [94].

In addition to studies on active sites of zeolites with medium and large pore sizes, studies on the coordination chemistry of dicopper-oxo complexes have focused on zeolites with small pores. Ipek et al. suggested three stable structures of dicopper-oxo in Cu/SSZ-13. The first one was the trans- $\mu$ -1,2-peroxo dicopper(II) site containing Cu–O and Cu–Cu bonds with the distances of 1.82–2.65 Å and 3.98 Å, respectively, where two Cu atoms were bridged to Al sites on 6 MR and 8 MR. The second one was the  $[\text{Cu}_2^{\text{II}}(\mu\text{-O})]^{2+}$  motif hosted on 8MR, with Cu–O distance of 1.76 Å and Cu–O–Cu angle of 95 °. The third one,  $[\text{Cu}_2(\mu\text{-O})_2]^{2+}$  peroxodicopper(II) site hosted on 8 MR, was anchored on isolated Al site and adjacent silanol defect, having different coordination structure from the first one [69].

There are also other studies proposing coordination structures for trinuclear Cu-oxo  $[\text{Cu}_3(\mu\text{-O})_3]^{2+}$  sites, anchored on Al pair sites, hosted on 8 MR of MOR, as active sites. However, the Cu–O–Cu angles of the  $[\text{Cu}_3(\mu\text{-O})_3]^{2+}$  motifs were stated to be different because of the nonconformity of coordination chemistry, which differentiated the ability of the bridging O atoms to activate the methane C–H bond [75], [94]. It was also observed that there were similar coordination properties of  $[\text{Cu}_3(\mu\text{-O})_3]^{2+}$  sites in CHA and MAZ zeolites.

Compared to multicopper-oxo clusters, monocopper species such as  $[\text{Cu}(\text{II})\text{OH}]^+$  and bare  $\text{Cu}(\text{II})$  sites were noted to be different in that they possessed simpler coordination structures. For instance, Cu atom isolated by OH ligand could be anchored to Si–O–Al site on zeolite ring. Such monocopper coordination structure was stated to be available in Cu-zeolites having high Si/Al ratio and/or low Cu content [95]. Furthermore, the coordination structure of single  $\text{Cu}(\text{II})$  sites hosted on 6 MR was investigated using DFT calculations. Single  $\text{Cu}(\text{II})$  sites confined on 6 MR exhibited four different coordination modes due to Al distribution, resulting in a four-fold coordination structure in which Cu cations coordinate with O atoms near the Al and Si sites. It was also stated that experimental EPR signals could be used to differentiate between coordination modes [96].

Overall, Cu-zeolites can possess active sites with various coordination structures due to differences in ring size, Al distribution, Cu/Al ratios and the topology of zeolites due to different frameworks. For instance, it has been reported that there were eight coordination structures of Cu active sites in CHA zeolites at 8 MR and four structures were the most stable structures. In CHA,  $\text{Cu}^+$  and  $[\text{Cu}(\text{OH})]^+$  when there is less  $\text{O}_2$ ,  $[\text{Cu}_2^{\text{II}}(\mu\text{-O})]^{2+}$  when there is  $\text{O}_2$  but not  $\text{H}_2\text{O}$ ,  $[\text{Cu}_2^{\text{II}}(\mu\text{-OH})_2]^{2+}$  is more stable when there is  $\text{H}_2\text{O}$  [77]. Additionally,  $[\text{Cu}_2^{\text{II}}(\mu\text{-O})]^{2+}$  sites have different coordination modes in zeolite frameworks. Hence, various Cu active sites can contribute to the activity of MTM process through different coordination structures [97]. Investigations into the presence of several Cu active sites in zeolites could help to understand the mechanism of MTM process. Nevertheless, the determination of Cu active sites is quite challenging due to the complicated structural coordination in Cu-zeolites and the limit of available characterization techniques.

### 2.1.2 Cu Active Site Formation

Several studies have indicated that  $[\text{Cu}(\text{II})(\text{H}_2\text{O})_n]^{2+}$ -exchanged zeolites subjected to dehydration and oxidation, followed by the formation of Cu-oxo active species such as  $\text{Cu}_x\text{O}_y$  clusters and  $[\text{CuOH}]^+$  monomer after calcination or high-temperature

activation. The formation of active species with unique coordination structure in Cu-zeolites is influenced by several parameters like activation temperature and time, dehydration and oxidation conditions, gas atmosphere, zeolite synthesis methods, as well as Si/Al and Cu/Al ratios [15], [75]. In studies conducted by Paolucci et al. and Borfecchia et al., the dehydration and oxidation of Cu-SSZ-13 were investigated using DFT calculations and spectroscopic analyses including XAS, XES, FTIR [84], [88]. They revealed that the Cu-oxo motif formation as active site in zeolites was relied on the gas atmosphere and dehydration temperature. For instance, they observed that  $[\text{CuOH}]^+$  monomer was present in SSZ-13 at about 250 °C. When temperature was between 250–350 °C, this monomer became more stable in O<sub>2</sub>-containing environment. Moreover, at temperatures above 350 °C, these species transformed into bare Cu(II) species [78], [88].

In the literature, it was stated that high temperature activation of Cu-exchanged zeolites having high Cu loadings with Cu/Al>0.1 could show the formation of Cu<sub>a</sub>O<sub>b</sub> motifs (a≥2). For instance, Ipek et al. observed the formation of dicopper  $[\text{Cu}_2\text{O}_2]^{2+}$  and  $[\text{Cu}_2\text{O}]^{2+}$  species over high Cu-containing SSZ-13 zeolite by dehydration reaction between two neighboring  $[\text{CuOH}]^+$  sites. They stated that the formation of these species was favored by the close proximity of  $[\text{CuOH}]^+$  intermediates [75].  
Larsen

Larsen et al. stated that Cu(I) and  $[\text{CuO}]^+$  structures were formed after the loss of water ligands in zeolites having high Cu content. However, since the  $[\text{CuO}]^+$  structures were not stable, they transformed into trans- $\mu$ -1,2-peroxo dicopper  $[\text{Cu}_2\text{O}_2]^{2+}$  species. At high temperatures (>350 °C) with the help of O<sub>2</sub>, these structures further transformed into mono-( $\mu$ -oxo) dicopper(II)  $[\text{Cu}_2\text{O}]^{2+}$  [84].

Smeets et al. used UV–Vis analyses to demonstrate the mechanism for formation of  $[\text{Cu}_2(\mu\text{-O})]^{2+}$  motifs during O<sub>2</sub> activation. They revealed that after activation of auto-reduced Cu(I)/ZSM-5 sample using O<sub>2</sub>, a UV-Vis band at approximately 29000 cm<sup>-1</sup> was obtained, which was later attributed to the formation of  $\mu$ -( $\eta^2$ : $\eta^2$ ) peroxo  $[\text{CuOOCu}]^{2+}$  motifs as O<sub>2</sub> precursor. Then, they found that with temperature increase

in He or O<sub>2</sub> atmospheres, [Cu<sub>2</sub>(μ-O)]<sup>2+</sup> species was formed (according to UV–Vis band at ~22700 cm<sup>-1</sup>), and the band at 29000 cm<sup>-1</sup> disappeared, indicating that the formation of [Cu<sub>2</sub>O]<sup>2+</sup> active sites was relevant with [CuOOCu]<sup>2+</sup> precursor [64]. Furthermore, Mahyuddin et al. suggested the formation pathway of μ-oxo-bridged [Cu<sub>2</sub>O]<sup>2+</sup> motifs in Cu(I)/MOR. They also stated that the formation of larger tricopper cluster ([Cu<sub>3</sub>(μ-O)<sub>3</sub>]<sup>2+</sup>) active sites were more complex than the formation of monocopper(II) and dicopper-oxo cluster sites [98].

Ikuno et al. conducted similar studies on the investigation of active sites in MOR zeolites. They observed the presence of [Cu<sub>3</sub>(μ-O)<sub>3</sub>]<sup>2+</sup> active sites even at low activation temperatures of ≈50 °C with using O<sub>2</sub>/N<sub>2</sub>O mixture [99]. There are also other theoretical studies on the formation of [Cu<sub>3</sub>(μ-O)<sub>3</sub>]<sup>2+</sup> active sites in the literature on different zeolite frameworks [28], [98].

Furthermore, dicopper-oxo and tricopper-oxo clusters could be formed after N<sub>2</sub>O oxidation of the reduced Cu(I) cations of Cu-exchanged zeolites. Several researchers investigated the formation mechanism of [Cu<sub>2</sub>O]<sup>2+</sup> with N<sub>2</sub>O activation of Cu(I)/ZSM-5. After heat treatment at 100 °C using N<sub>2</sub>O, [Cu<sub>2</sub>(μ-O)]<sup>2+</sup> species was formed according to UV–Vis analysis. During this activation, the two Cu(I) cations donated two electrons for N–O cleavage of N<sub>2</sub>O and obtained an oxo to form the [Cu<sub>2</sub>O]<sup>2+</sup> motif, as well as N<sub>2</sub> [62], [100].

Several studies indicated that Cu-zeolites could be activated anaerobically (in presence of H<sub>2</sub>O) at high temperatures. This anaerobic activation resulted in the creation of [Cu<sub>2</sub>O<sub>2</sub>]<sup>2+</sup> and [Cu<sub>2</sub>O]<sup>2+</sup> active sites by the delivery of active oxygen by OH<sup>-</sup> groups or water. For example, the combination of two [CuOH]<sup>+</sup> motifs in the zeolite framework formed a mono-(μ-oxo) dicopper [Cu<sub>2</sub>O]<sup>2+</sup> motif by desorbing water where the active O atom originated from the OH<sup>-</sup> group of [CuOH]<sup>+</sup> site. Additionally, Sushkevich et al. suggested that water provided O atom for the reoxidation of Cu(I) species formed by methane oxidation on [Cu<sub>2</sub>O]<sup>2+</sup> active sites in MOR.

Besides, the amount of Cu loading, and Si/Al ratio of zeolites were indicated to have a significant role in forming Cu active sites with diverse coordination structures, in addition to activation conditions such as gas environment and temperature. For instance, the production of Cu-oxo motifs, as well as their coordination structures in CHA and AEI zeolites, were linked to Cu and Al concentration, where higher Al amount in Cu/SSZ-13 promoted the bare Cu(II) sites formation, higher Cu loading, and lower Si/Al ratio resulted in the formation of higher concentration of  $\text{Cu}_x\text{O}_y$  clusters in Cu/SSZ-13 sample [75].

## 2.2 Activity Test of Cu-Zeolites

Research on DMTM using Cu-zeolites has primarily focused on two different processes: stepwise and continuous catalytic as mentioned before. Cu active site centers on zeolite require high-temperature activation (300–550 °C), whereas activation of methane is accomplished at lower temperatures (~200 °C) to prevent over-oxidation. Most investigations on MTM use a stepwise procedure, often consisting of three phases. Cu-zeolites are activated at high temperatures through oxidative activation, followed by a methane reaction at around 200 °C and methanol extraction from active Cu sites using steam or a solvent at 20–200 °C as mentioned before. This technique avoids over-oxidation, resulting in good selectivity of methanol. However, the activation of Cu-zeolites at high-temperature, as well as the extraction via solvent-based such as methanol, are costly. Moreover, the absence of constant feed, changing reaction temperature is problem and as a result, this procedure may not be convenient for an industrial setting. The continuous catalytic process of  $\text{CH}_4$ ,  $\text{O}_2$  (or  $\text{N}_2\text{O}$ ),  $\text{H}_2\text{O}$ , and Cu-zeolites at 200–350 °C eliminates the requirement for high-temperature activation and solvent extraction and it is easy for application to the industry.

Table 2.2 summarizes activity test results of Cu-zeolites for MTM in stepwise or continuous processes over the past 6 years. Only a few works use continuous DMTM with  $\text{O}_2$ ,  $\text{H}_2\text{O}$ , or  $\text{N}_2\text{O}$  as the oxidant but in Table 2.2, we focused on continuous

catalytic process to compare them our results. The continuous catalytic method shows great potential in the production of methanol from methane, but there are still some gaps in the understanding of this field. First of all, the introduction of multiple gases makes it difficult to understand the active sites. Moreover, the complex structure of zeolites makes this situation even more difficult to understand. However, given the advantages over stepwise, such as constant gas flow with lower and constant temperature, it is better to concentrate on this area.

According to a study in the literature, H<sub>2</sub>O acts as a soft oxidant. In addition to stabilization of intermediates and desorption of methanol in the reaction mechanism, it also prevents conversion to CO and CO<sub>2</sub> by overoxidation. However, it is still controversial that it acts as a direct oxygen source in methanol production. [81].

Narsimhan et al. investigated the continuous catalytic DMTM process on Cu-zeolites. Although activated Cu-zeolites were exposed to pure CH<sub>4</sub> at 210°C to initiate the continuous reaction, a mixture of CH<sub>4</sub>, O<sub>2</sub> and H<sub>2</sub>O was subsequently introduced to the catalysts at the same temperature. Although the Cu-zeolite surface stoichiometrically absorbed a significant concentration of methanol, the yield in the continuous catalytic process was rather modest (0.9-1.8 μmol·h<sup>-1</sup>g<sup>-1</sup>) [101]. However, this study did not demonstrate the oxidizing effect of H<sub>2</sub>O in the MTM process.

Returning to the water discussion, Koishybay et al. studied the continuous conversion of MTM over Cu/SSZ-13 under anaerobic conditions (CH<sub>4</sub> + H<sub>2</sub>O) as shown in Table 2.2. In this study, although initially quite high methanol desorption was observed, after about 200 min, the continuous catalytic process reached a consistent but low methanol production rate of 0.013 mol/molCu/h and 6.05 μmol·h<sup>-1</sup>g<sup>-1</sup> as shown in Table 2.2 [102].

Some scientists have used isotope and in situ FTIR to prove that H<sub>2</sub>O, not O<sub>2</sub>, is involved in methanol production. Sun et al. conducted tests using CHA, MOR, MFI with copper exchanged into the continuous catalytic method by introducing a gas mixture containing 2% H<sub>2</sub>O and 50 to 3000 ppm O<sub>2</sub>. As a result, very high methanol

selectivity (91%), a TOF value of 0.54 (molCH<sub>3</sub>OH/molCu/h) and 195 μmol·h<sup>-1</sup>g<sup>-1</sup> methanol production were achieved at 300 °C (see Table 2.2), which is well ahead of previous studies [103]. According to this study operating reaction at 300°C in MTM provides the transformation cycle of Cu<sup>2+</sup>-Cu<sup>+</sup>, and giving higher methane conversions.

Another study investigated how reaction temperature affects continuous MTM. A low O<sub>2</sub>/CH<sub>4</sub> ratio (lower than 0.0005) improves methanol selectivity and prevents overoxidation to CO<sub>2</sub> [104]. Yet, the use of H<sub>2</sub>O as an oxidant in this process is still debated due to the possibility of impurities such as O<sub>2</sub>. Zhou et al. studied the activity of continuous MTM conversion under anaerobic conditions at different reaction temperature, similar to the previous work [73]. They attempted to eliminate O<sub>2</sub> impurities from deionized water by heating it in the flow of He. Cu-zeolites exhibit a "volcanic" trend in anaerobic conversion performance as reaction temperature rises, with Cu/CHA zeolite performing best at 350°C [73].

Although H<sub>2</sub>O is claimed to be an oxidant and evidence is presented in the studies mentioned above and in Table 2.2, the effect of H<sub>2</sub>O is still controversial as it would be very difficult to prevent systemic errors. In the most recent study, although the exact effect of H<sub>2</sub>O cannot be explained, it is thought to be involved in the formation of activated sites rather than oxidant. They found outstanding results in terms of TOF and methanol production using AEI (SSZ-39) type zeolite as can be seen from Table 2.2 [105], [106].

Table 2.2. Activity test results given in the literature

<b>Cu-Zeolite</b>	<b>Cu/Al</b>	<b>Si/Al</b>	<b>Process Type</b>	<b>Oxidant</b>	<b>T<sub>Activation</sub> (°C)</b>	<b>T<sub>Reaction</sub> (°C)</b>	<b>Methanol Production <math>\mu\text{mol}\cdot\text{h}^{-1}\text{g}^{-1}</math></b>	<b>TOF mol/molCu/h</b>	<b>S (%)</b>	<b>Ref.</b>
MOR	0.13	11.3	Stepwise	O <sub>2</sub>	500	200	---	0.28	88	[107]
MOR	0.36	11.3	Stepwise	O <sub>2</sub>	500	200	---	0.26	91	[107]
CHA	0.16	12.1	Stepwise	O <sub>2</sub>	500	200	---	0.10	85	[107]
CHA	0.49	12.1	Stepwise	O <sub>2</sub>	500	200	---	0.17	86	[107]
ZSM-5	0.45	11.5	Stepwise	O <sub>2</sub>	450	200	---	0.19	58	[108]
SSZ-13	0.35	12	Stepwise	O <sub>2</sub>	450	200	31*	0.06	---	[109]
SSZ-39	0.26	10	Stepwise	O <sub>2</sub>	450	200	36*	0.09	---	[109]
Omega	0.29	6	Stepwise	O <sub>2</sub>	450	200	86*	0.09	---	[110]
FER	0.38	9	Stepwise	O <sub>2</sub>	450	200	10*	0.02	---	[110]
MOR	0.15	7.5	Continuous	Steam	---	350	---	0.017	100	[111]
MOR	0.19	15	Continuous	Steam	---	350	---	0.022	100	[111]
SSZ-39	0.22	6.3	Continuous	N <sub>2</sub> O	---	325	499	1.02	34	[112]
SSZ-13	0.10	9.7	Continuous	N <sub>2</sub> O	---	300	24	0.157	59	[112]

Table 2.2. Activity test results given in the literature (Continued)

<b>Cu-Zeolite</b>	<b>Cu/Al</b>	<b>Si/Al</b>	<b>Process Type</b>	<b>Oxidant</b>	<b>T<sub>Activation</sub> (°C)</b>	<b>T<sub>Reaction</sub> (°C)</b>	<b>Methanol Production <math>\mu\text{mol}\cdot\text{h}^{-1}\text{g}^{-1}</math></b>	<b>TOF mol/molCu/h</b>	<b>S (%)</b>	<b>Ref.</b>
MOR	0.15	8.9	Continuous	N <sub>2</sub> O	---	300	55	0.22	54	[112]
CHA	0.8	17.8	Continuous	CO/O <sub>2</sub>	---	200	53	0.08	---	[113]
SSZ-13	0.33	10	Continuous	O <sub>2</sub>	---	225	---	0.013	---	[103]
SSZ-13	0.22	23	Continuous	O <sub>2</sub>	---	270	19.2	0.13	---	[114]
SSZ-13	0.23	11	Continuous	O <sub>2</sub>	---	300	195	0.54	91	[103]
MOR	0.27	10.9	Continuous	O <sub>2</sub>	---	300	---	0.015	18	[103]
ZSM-5	0.27	12.8	Continuous	O <sub>2</sub>	---	300	---	0.1	18	[103]
CHA	0.13	5	Continuous	O <sub>2</sub>	---	300	---	0.7	79	[68]
CHA	0.08	10	Continuous	O <sub>2</sub>	---	300	---	0.9	88	[68]
CHA	0.12	13	Continuous	O <sub>2</sub>	---	300	---	1.7	68	[68]
SSZ-39	0.06	10	Continuous	N <sub>2</sub> O	---	350	~2100	23.2	~50	[106]
SSZ-39	0.03	7.3	Continuous	N <sub>2</sub> O	---	350	~950	15.8	~55	[106]
SSZ-39	0.10	9.7	Continuous	N <sub>2</sub> O	---	350	~1800	11.7	~50	[106]

Table 2.2. Activity test results given in the literature (Continued)

<b>Cu-Zeolite</b>	<b>Cu/Al</b>	<b>Si/Al</b>	<b>Process Type</b>	<b>Oxidant</b>	<b>T<sub>Activation</sub> (°C)</b>	<b>T<sub>Reaction</sub> (°C)</b>	<b>Methanol Production <math>\mu\text{mol}\cdot\text{h}^{-1}\cdot\text{g}^{-1}</math></b>	<b>TOF mol/molCu/h</b>	<b>S (%)</b>	<b>Ref.</b>
SSZ-39	0.22	9.7	Continuous	N <sub>2</sub> O	---	350	~800	2.4	~20	[106]

\*  $\mu\text{mol}\cdot\text{g}^{-1}$

## 2.3 Reaction Mechanism Studies

Many mechanisms for stepwise processes have been proposed in the literature. These described mechanisms may not be applicable to the continuous catalytic process due to the differences in reaction conditions and steps. In the stepwise process, high temperatures are needed to provide mono( $\mu$ -O) dicopper active centers in zeolites, whereas no activation is needed in the continuous process. In addition, the coexistence of  $H_2O$  and oxidant favors the formation of hydroxylated copper species more than other species. At the same time, the regeneration mechanism of these hydroxylated copper species should be considered in the same way. In the continuous catalytic method,  $CH_4$ ,  $N_2O$  or  $O_2$  and  $H_2O$  hydrolyze copper-zeolites, resulting in the formation of monomeric copper species. These samples are usually the closest candidates to become active sites.

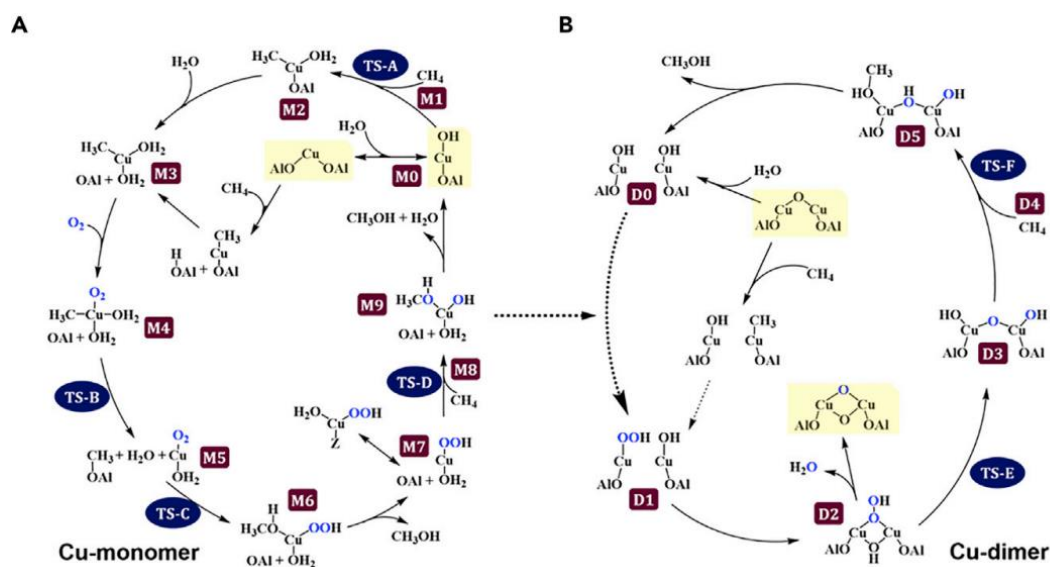


Figure 2.1. Possible reaction mechanism on the Cu-monomer  $[CuOH]^+$  (A) and Cu-dimer  $[Cu_2O]^{2+}$  (B) in a continuous DMTM using DFT simulation [103]

Li et al. proposed two different mechanisms for the conversion of methane to methanol by copper zeolites in a continuous catalytic method using their own DFT study and experimental studies in the literature. In the mechanisms in Figure 2.1, one

pathway is explained through the monomer structure, while the other is explained through the dimer active site.

In the first mechanism in Figure 2.1 A, the CH<sub>4</sub> molecule is adsorbed on the monomer structure. H<sub>2</sub>O molecule also coordinated on the complex structure and formed a new complex structure. In this study, H<sub>2</sub>O was involved not only in methanol desorption but also in the complex structure formed before O<sub>2</sub> in the mechanism. Since N<sub>2</sub>O dissociation takes place at the surface and O is formed, we can think that O<sub>2</sub> is involved in the mechanism in this way in our study. It has been claimed that O<sub>2</sub> adsorbs to copper and forms a four-coordinated complex. CH<sub>3</sub>-O-Al structure was formed immediately afterwards. H<sub>2</sub>O was also added to this structure and took part in the mechanism again. As can be seen in M6 in Figure 2.1, the H atom formed as a result of H<sub>2</sub>O dissociation joined the copper center, while CH<sub>3</sub> formed a new complex structure with the remaining OH groups. The molecule desorbed from this complex structure with the help of H<sub>2</sub>O is CH<sub>3</sub>OH. The CuOOH or hydrated CuOOH remaining after desorption is very important for subsequent conversions. O<sub>2</sub> is involved in the regeneration of the monomer active site and the continuation of the reaction. As can be seen from these reasons, O<sub>2</sub> and especially H<sub>2</sub>O are essential for methanol production in the continuous catalytic method [103]

The mechanism in Figure 2.1 B describes the mechanism formed by the Cu-dimer structure. However, compared to stepwise, the roles of these active sites in the continuous catalytic method differ. These Cu-dimer active sites, which are involved in the breaking of C-H bonds in the stepwise method, hydrolyze at high temperature in the continuous catalytic method to form two Cu-monomer active sites. After the formation of these monomers ([CuOH]<sup>+</sup>), the activation of methane and the formation of methanol continues as shown in Figure 2.1 A [103].

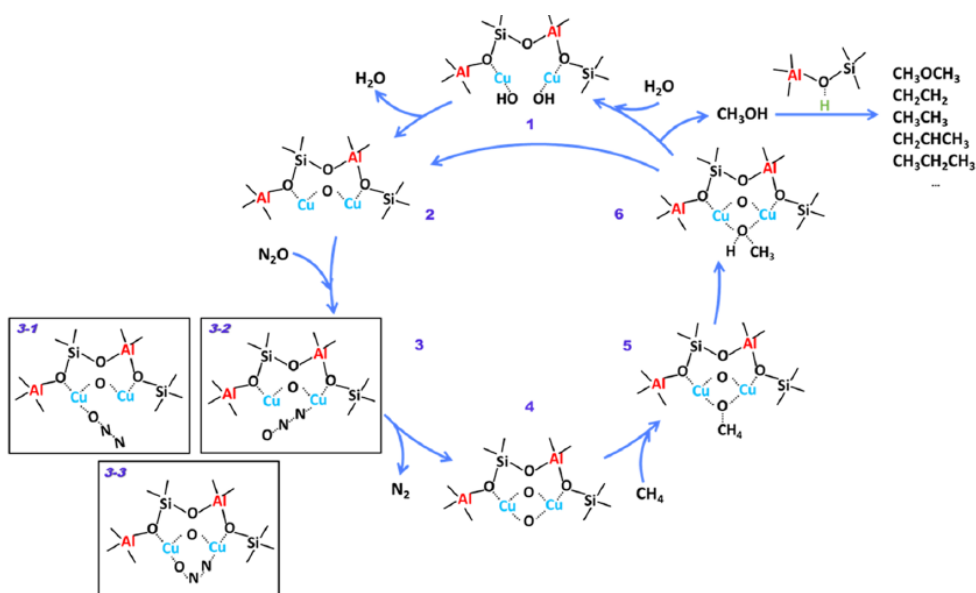


Figure 2.2. Possible reaction mechanism for Cu/SSZ-39 [105]

In another study in the literature, active sites and reaction mechanism were proposed on Cu/SSZ-39 zeolites in a scenario using  $N_2O$  as oxidant. Only here, in Figure 2.2  $H_2O$  is depicted as a molecule that is immediately dehydrolyzed in the reaction mechanism. It is a great controversial that  $H_2O$ , which is thought to be involved in both the desorption of methanol and the formation of the active site, and even stated to be a soft oxidant, is not included in the mechanism. In this mechanism,  $CuOH$  structure is dehydrated and bis( $\mu$ -oxo) dicopper active sites are formed. After activation,  $N_2O$  adsorbs on this active site and forms O and  $N_2$ . The O atom coming from here is thought to be the active O on the active site. This O atom breaks the C-H bond by adsorbing  $CH_4$  and transforms it into methoxy and H structures. After methanol is formed, it can be converted into DME by utilizing the acid sites in the zeolite structure. Again, methanol and DME can be converted into olefins. CO and  $CO_2$  can also be formed as a result of the breakage of methoxy structures or oxidation of methanol with  $N_2O$  [105].

As it can be understood from the 3 different mechanism examples given above, it is very difficult to understand and clarify the reaction mechanism in the continuous catalytic method. While the reaction is carried out by the continuous catalytic

method, very complex situations can be facilitated since the C-H bond cleavage, desorption of methanol, the effect of H<sub>2</sub>O to active sites and zeolite structures, the conversion of methanol to DME, methanol and DME to olefins, the formation of CO and CO<sub>2</sub> and the regeneration of active sites occur simultaneously. Moreover, Cu cation mobility in Cu-zeolites plays a crucial role in understanding continuous MTM reactions when H<sub>2</sub>O and CH<sub>4</sub> are continuously supplied into the system [115].

Cu-zeolites may include several active species at the same time, such as [CuOH]<sup>+</sup>, [Cu<sub>2</sub>O]<sup>2+</sup>, [Cu<sub>2</sub>O<sub>2</sub>]<sup>2+</sup>, and [Cu<sub>3</sub>O<sub>3</sub>]<sup>2+</sup> in addition to their hydroxylated counterparts. This could lead to many reaction pathways for continuous MTM processes. Current research is ambiguous on the reaction mechanisms, which require further confirmation by tests and theoretical calculations.

## CHAPTER 3

### EXPERIMENTAL METHODOLOGY

This section includes the synthesis and preparation processes of catalysts, their characterization, instrument features, operating procedures and catalytic activity set-up.

#### 3.1 Catalyst Synthesis and Preparation

##### 3.1.1 Micro-H<sup>+</sup>-FER

Commercially obtained zeolite (NH<sub>4</sub><sup>+</sup>-Ferrierite, Si/Al=10, Alfa Aesar) was used. H<sup>+</sup>-Ferrierite was obtained following heat treatment of NH<sub>4</sub><sup>+</sup>-Ferrierite at 550 °C as explained in more detail in the following section.

##### 3.1.2 Nano-H<sup>+</sup>-FER

Nano-FER zeolite was synthesized by hydrothermal method with the help of CTABr (Sigma, 98% purity) and Piperidine (Acros, 99% purity) using a molar ratio of 1 SiO<sub>2</sub>: 0.0314 Al<sub>2</sub>O<sub>3</sub>: 0.066 Na<sub>2</sub>O: 0.4 PI: 17 H<sub>2</sub>O: 0.01 CTABr. 12.52 g of Ludox HS-40 (Aldrich), 0.485 g of Sodium Aluminate (Sigma Aldrich), 0.158 g of NaOH (Merck, 99%), 18 g of DI H<sub>2</sub>O and 0.17 g CTABr were stirred for 30 minutes at 25°C. It was then transferred to a Teflon-lined autoclave and maintained at 110 °C for 36 hours with a rotating speed of 45 rpm in the tumbling oven. After 36 h, the gel was quenched and 2.83 g of piperidine was added to the mixture. The resulting mixture was kept at 150°C for 132 more hours at a rotating speed of 60 rpm. The final mixture was filtered and washed with de-ionized (DI) water using a centrifuge at 4000 rpm until a pH value of 7 was observed. The recovered solid was dried at 60

°C overnight. Samples of Nano-Na<sup>+</sup>-FER were calcined at 550 °C for 5 hours under 40 sccm air flow. After NH<sub>4</sub><sup>+</sup>-exchange using 1 M NH<sub>4</sub>NO<sub>3</sub> solutions, Nano-Na<sup>+</sup>-FER were transformed into H<sup>+</sup>-FER, which were noted as Nano-H<sup>+</sup>-FER. This method was adapted from the work by Wang et al. [116].

### **3.1.3 Steam-Meso-H<sup>+</sup>-FER**

NH<sub>4</sub><sup>+</sup>-Ferrierite (Si/Al=10) was obtained from Alfa Aesar. 2 g of NH<sub>4</sub><sup>+</sup>-Ferrierite was placed into a ½ inch quartz tube and calcined at 550 °C under 50 sccm air flow for 4 h using a heating rate of 5 °C min<sup>-1</sup>. Resulting H<sup>+</sup>-Ferrierite was cooled to 450 °C under air flow. Then, steam treatment was performed at 450 °C for 3 hours with a water flow rate of 0.44 mL.min<sup>-1</sup>. The sample was dried under air flow overnight. Then, 1 g sample was washed in 50 mL 0.2 M HCl acid solution at 80 °C to remove the extra Al sites in the framework structure. The solution was then filtered and washed using DI water. The sample dried in the oven at 60 °C overnight and named Steam-Meso-H<sup>+</sup>-FER. This method was adapted from the work applied for ZSM-5 [117].

### **3.1.4 CTABr-Meso-H<sup>+</sup>-FER**

Mesoporous Ferrierite was prepared by recrystallization method using CTABr as a mesopore forming agent. Ferrierite (NH<sub>4</sub><sup>+</sup>-Ferrierite, Si/Al=10, Alfa Aesar), NaOH (Sigma-Aldrich), CTABr (ISOLAB) and deionized water were used as raw materials. In a typical synthesis, 1.67 g of H<sup>+</sup> FER and 0.83 g of CTABr were stirred with 50 mL of 0.25 mol L<sup>-1</sup>. NaOH solution for 30 min at room temperature. The suspension was hydrothermally treated at 130 °C in a Teflon-lined stainless-steel autoclave for 72 h. After quenching the autoclave with water, the solid was filtered using vacuum filtration (using 200 nm pore sized cellulose acetate membranes) and washed with deionized water until a pH of 7 was obtained. Finally, the product was dried at 80°C in the oven overnight. The resulting zeolite was then ion-exchanged in

NH<sub>4</sub>NO<sub>3</sub> solution. Details are stated in the following section. The procedure was taken by adapting the conditions from the Cheng et al. [118].

### **3.1.5 Micro-H<sup>+</sup>-SSZ-39**

An SSZ-39 (AEI type zeolite) was hydrothermally synthesized by mixing 38.75 g of tetramethyl piperidinium hydroxide (Sachem, Inc., 35.3 wt.%) as SDA, 103.1 g of DI (de-ionized) water, 77.50 g of sodium silicate solution (Merck, 37 wt.%) for 30 minutes at 25 °C. After observing a clear mixture, 7.28 g NH<sub>4</sub>-USY (Alfa Aesar, Zeolite Y, Si/Al = 12) was added very slowly to the solution and the stirred for half an hour. The synthesis solution was then transferred to 6 pieces of 33 mL Teflon-lined autoclaves and hydrothermally treated at 150 °C for one week under rotation at 50 rpm. Crystals were filtered using vacuum filtration, washed with DI H<sub>2</sub>O and dried at 80 °C overnight.

For the removal of ANA phases, 1 M HCl solution was prepared. 100 mL of 1 M HCl solution per 1 gram of zeolite is used for acid-washing at 80 °C for 3 hours. After the acid treatment, zeolite was washed with DI water. Calcination was performed in a static furnace at 120 °C for 1 h and 550 °C for 6 h (heating rate of 2 °C/min). The NH<sub>4</sub><sup>+</sup>-exchange procedure for Micro-Na-SSZ-39 was performed using a 1 M NH<sub>4</sub>NO<sub>3</sub> solution (100 mL solution per gram zeolite) at 80 °C for 3 h. This procedure was repeated two times. After washing the sample using hot DI water, heat treatment was performed at 120 °C for 1 hour. The procedure was adapted from the procedures given by Ipek et al. and Dusselier et al. [75], [119].

### **3.1.6 Micro-H<sup>+</sup>-SSZ-13**

An SSZ-13 (CHA type zeolite) was synthesized using hydrothermal method with a similar procedure given by Pham et al using a solution having a molar composition of 1 SiO<sub>2</sub>: 0.035 Al<sub>2</sub>O<sub>3</sub>: 0.5 TMAdaOH: 20 H<sub>2</sub>O. 108 g of N, N, N-trimethyl-1-adamantanamonium hydroxide solution (TMAdaOH, Sachem, 30 wt.%) as SDA and

3.574 g  $\text{Al}(\text{EtO})_3$  (Sigma Aldrich, 97wt.%) as aluminum source were mixed for one hour at RT to dissolve the aluminum ethoxide. At the same time, 65.1 g tetraethyl orthosilicate (TEOS, Merck, 98 wt.%) were transferred to the 24 g  $\text{H}_2\text{O}$  (DI) drop wisely and stirred for one hour at 25 °C. The final mixture of TEOS and  $\text{H}_2\text{O}$  were added to the SDA+ $\text{Al}(\text{EtO})_3$  mixture drop wisely. Total mixture was stirred for 2 hours. This mixture was then transferred to 6 Teflon-lined autoclaves. The synthesis gels were hydrothermally treated at 150 °C for seven days under internal pressure in the static furnace. Zeolite crystals were filtered using centrifuge, washed with DI  $\text{H}_2\text{O}$  and dried at 80 °C overnight. Calcination was made in a static furnace 120 °C for 1 h and 580 °C for 8 h (using a heating rate of 2 °C  $\text{min}^{-1}$ ). The procedure was adapted from the procedure given by Pham et al. [120].

## **3.2 Ion-Exchange Procedure**

Various ion-exchanges of the prepared zeolites have been performed for different purposes.  $\text{Na}^+$ -exchange was performed in zeolites to provide more copper loading, to understand the Bronsted acid site effect, and in the procedure before cobalt-exchange. In order to make use of the Bronsted acid sites,  $\text{Na}^+$ -form zeolites were firstly exchanged to  $\text{NH}_4^+$ -form and then heat treated to obtain the  $\text{H}^+$ -form. Cobalt-exchange was carried out to investigate the possible Al pairs in the framework of the prepared zeolites. Finally, copper-exchange was carried out to create an active site in the reaction.

### **3.2.1 $\text{Na}^+$ -Exchange**

For  $\text{Na}^+$ -exchange, 0.02 M sodium nitrate (99% Sigma Aldrich) solution was prepared. 1 g of zeolite was stirred in 100 mL of solution at 60 °C for 3 hours. It was then filtered using vacuum filtration and washed using deionized water. This procedure was repeated 3 times. It was ensured that the pH did not fall below 5.2 throughout the procedures. For Micro-FER, after  $\text{Na}^+$  exchange,  $\text{Cu}^{2+}$ -exchange was

also performed. Moreover, before the cobalt-exchange. Na<sup>+</sup>-exchange was also applied for Micro-FER and Nano-FER. But for these zeolites, Na<sup>+</sup>-exchange was performed at 80 °C for 7 hours for 3 times [121].

### 3.2.2 NH<sub>4</sub><sup>+</sup>-Exchange

NH<sub>4</sub><sup>+</sup>-exchange was performed using an aqueous mixture of ammonium nitrate (NH<sub>4</sub>NO<sub>3</sub>, Sigma Aldrich, 99% by weight) (100 mL solution per gram of zeolite). For NH<sub>4</sub><sup>+</sup>-exchange of Nano-Na<sup>+</sup>-FER, 1 M NH<sub>4</sub>NO<sub>3</sub> solution, for Micro-Na<sup>+</sup>-SSZ-39, 2.5 M NH<sub>4</sub>NO<sub>3</sub> solution was prepared. The solution was stirred for 3 hours at 80 °C for ion-exchange, while pH and temperature values were monitored throughout the process. 3 hours later, the zeolites were filtered using cellulose acetate membrane on vacuum filters with 200 nm pore size or centrifuged, washed using deionized H<sub>2</sub>O, and dried at 80 °C under static conditions for one hour. This exchange procedure was redone one more time using the same conditions and exchanged zeolite. Finally, the heat treatment was done NH<sub>4</sub><sup>+</sup>-zeolites at 550 °C for 5 h in a static oven using a heating rate of 2 °C min<sup>-1</sup>. The resulting zeolite was designated as Micro/Nano-H<sup>+</sup>-Zeolite.

### 3.2.3 Cu<sup>2+</sup>-Exchange

Cu<sup>2+</sup>-exchange was made by exchanging the H<sup>+</sup>-form of the zeolites in copper (II) acetate solution at different temperatures. Generally 1 g of H<sup>+</sup>-zeolite was treated in 250 mL of aqueous solutions containing copper (II) acetate monohydrate (Merck, 99% by weight) at varying concentrations (0.0003M–0.1M). The exchange procedure was performed for 2.5 to 24 h at 25 °C, depending on the desired extent of exchange. After the exchange, obtained Cu<sup>2+</sup>-zeolites were filtered or centrifuged, washed using 500 mL of deionized water, and dried overnight at 80 °C. For Cu<sup>2+</sup>-exchange of FER samples, the temperature was increased to 60 °C (for 3 h of exchange time) to overcome the ion-exchange limitations of FER.

### **3.2.4 Co<sup>2+</sup>-Exchange**

Co<sup>2+</sup>-exchange (Cobalt (II) nitrate hexahydrate, Merck, 98%) was performed by treating 1 g of Nano-Na<sup>+</sup>-FER or Micro-Na<sup>+</sup>-FER in 100 mL of 0.25 M cobalt (II) nitrate solutions at 80 °C for 7 hours. The exchange procedure was repeated two more times [106].

### **3.3 Characterization Methods and Techniques**

In order to understand the phase types and purities X-ray Diffraction, for surface area and pore volumes N<sub>2</sub> physisorption experiments at -196 °C, for elemental compositions Inductively Coupled Plasma-Optical Emission Spectrometer, for topology Scanning Electron Microscopy, for copper metal and defect sites Transmission Electron Microscopy, for Al and Si structures Magic Angle Spinning NMR Spectroscopy and finally for active sites UV–Vis and Raman spectroscopy performed.

#### **3.3.1 N<sub>2</sub> Physisorption at 77K**

N<sub>2</sub> physisorption experiments were performed using a surface area and pore volume analyzer (Micromeritics Tristar II 3020) located at the METU Chemical Engineering Department. Samples were degassed in a vacuum set-up (Micromeritics VacPrep 061) at 300 °C for 6 hours under 150 μmHg vacuum conditions before N<sub>2</sub> adsorption studies. Following degassing, the sample holders were filled with N<sub>2</sub> (Oksan, 99.999%) and sealed before being transferred to the surface area and pore volume analyzer. The samples were then degassed at room temperature for 30 more minutes before the free volume tests that were conducted using, He (Oksan, 99.999%). Following the free volume measurements, vacuum treatment at room temperature was performed for an additional two hours. Finally, N<sub>2</sub> adsorption and desorption experiments were carried out at relative pressures (P/P<sub>0</sub>) ranging from 10<sup>-5</sup> to 0.98

and a constant temperature of  $-196\text{ }^{\circ}\text{C}$ . The statistical thickness, t-plot, method was applied to calculate the micropore volumes. The Barret-Joyner-Halenda (BJH) adsorption model was used to calculate the pore size distributions. The mesopore volume was calculated by subtracting the t-plot micropore volume from the single point pore volume at  $P/P_0 = 0.98$ .

### **3.3.2 X-Ray Diffraction (XRD) Analysis**

Powder X-Ray Diffraction (XRD) patterns were obtained at METU Central Laboratory using a Rigaku Ultima-IV X-ray diffractometer. A scan rate of  $1^{\circ}\text{ min}^{-1}$  was employed within the  $2\theta$  range of  $2\text{--}50^{\circ}$ . Cu  $K\alpha$  cathode tube ( $\lambda = 1.5418\text{ \AA}$ ) operated at 40 kV and 30 mA. XRD analysis was performed following the calcination of synthesized or ion-exchanged materials. This analysis was used to investigate the zeolite crystal structure.

### **3.3.3 Elemental Analysis**

The elemental compositions of the prepared samples were analyzed using an inductively coupled plasma-optical emission spectrometer (Perkin Elmer Optime4300DV, ICP-OES) located at METU Central Laboratory. The samples were initially dissolved in an HF/HNO<sub>3</sub> solution overnight. Some samples' Si, Al, and Cu concentrations were also measured using an Energy Dispersive X-ray Spectrometer (EDX) QUANTA 400F Field Emission SEM at METU Central Laboratory. EDX worked at a voltage of 20 kV and scanned at least four separate locations.

### **3.3.4 Scanning Electron Microscopy (SEM)**

Scanning Electron Microscopy (SEM) was used to analyze the morphology of the prepared zeolites. SEM analysis was conducted at METU Central Laboratory utilizing a QUANTA 400F Field Emission microscope at 20 kV and at METU

Chemical Engineering Department utilizing a TESCAN VEGA3 at 15–20 kV. Prior to analysis, the calcined samples were coated with a combination of Pd and Au.

### **3.3.5 Transmission Electron Microscopy (TEM)**

TEM (Transmission Electron Microscope) analysis was performed using Jeol 2100F HRTEM, High Resolution Transmission Electron Microscope located at METU Central Laboratory. Orius SC1000 Model 832 11 Megapixel CCD was used as the camera, carbon coated film grid and CF200-Cu Carbon film grid were used as the grid. The samples were powdered suspended in ethyl alcohol, mixed in an ultrasonic cleaner for 45 minutes, and then a drop was placed on the grid with a micropipette and left to dry for at least one night.

### **3.3.6 $^{27}\text{Al}$ and $^{29}\text{Si}$ Magic Angle Spinning Nuclear Magnetic Resonance**

The  $^{29}\text{Si}$  and  $^{27}\text{Al}$  MAS NMR spectra of Micro- $\text{NH}_4^+$ -SSZ-39 was analyzed on a Bruker Superconducting FT NMR Spectrometer Avance TM 300 MHz WB at METU Central Laboratory. The equipment includes a high-power Ultrashield<sup>TM</sup> 300 MHz magnet and a 4 mm MAS probe. Before the analysis, the calcined samples were hydrated at room temperature.

$^{27}\text{Al}$  and  $^{29}\text{Si}$  MAS-NMR spectra of Nano- $\text{Na}^+$ -FER and Micro- $\text{NH}_4^+$ -FER were obtained using JEOL NMR Spectrometer Ultrashield<sup>TM</sup> 500 MHz equipped with 5 mm standard probe located at Eskişehir Osmangazi University Central Research Laboratory.  $\text{AlNO}_3$  standard is taken before each sample. The analysis was obtained with a relaxation time of 5 second and a spin rate of 6kHz.

### **3.3.7 In-Situ Raman Spectroscopy**

Dispersive Raman spectra were applied using a Raman microscope spectrometer (Renishaw inVia) located at the METU Central Laboratory, equipped with a CCD

detector and 532 nm laser source. Raman spectra were collected using 1–10 mW power of laser, 10 s integration time in between the range of 100–1400  $\text{cm}^{-1}$ . Raman spectra were scanned under ambient environment for catalyst closed on both sides.

For  $\text{N}_2\text{O}$  activation, approximately 50 milligrams of hydrated powder form of catalyst were placed in the NMR reactor (approximately 1 cm fluid bed). Catalyst was filled between quartz wool in the NMR tube and deployed in the middle of the furnace for better heating control. The total inlet flow rate of the feed mixture (30%  $\text{N}_2\text{O}$  and a balanced amount of helium) was set at 40  $\text{cm}^3 \text{min}^{-1}$ . A heater with an Ordell OM04 temperature controller was used to heat the reactor. The temperature of the system was increased to 325  $^\circ\text{C}$  using a heating rate of 10  $^\circ\text{C min}^{-1}$  and kept constant at this temperature for 2 hours. The temperature was then cooled to 100  $^\circ\text{C}$  and the  $\text{N}_2\text{O}$  flow was stopped while the helium flow continued. The gas flow from both-side the NMR tube were closed with the help of a blowtorch at approximately 80  $^\circ\text{C}$ .

### **3.3.8 In-Situ Diffuse Reflectance UV–Visible Spectroscopy**

In-situ Diffuse Reflectance UV–Vis spectra were obtained using a UV–Vis spectrophotometer (Shimadzu UV–2600) equipped with a diffuse reflectance cell (ISR2600+). UV–Vis spectra of the hydrated Cu-zeolites were obtained from obtained pellets prior to the treatments. Then, 2 g of sample (Micro/Nano-Cu-FER/SSZ-39) was heated to 325  $^\circ\text{C}$  under He (Hatgaz, 99.999%) flow, which was then switched to 50%  $\text{N}_2\text{O}$  (Hatgaz, 99.9%) and 50% He flow for 2 h. After 2 h, the  $\text{N}_2\text{O}$  flow was turned off and the sample was cooled to room temperature in He flow prior to the spectra ( $\text{N}_2\text{O}$  treatment). Then the sample was heated back to 325  $^\circ\text{C}$ , where it was treated under 50%  $\text{N}_2\text{O}$  and 6%  $\text{H}_2\text{O}$  and 44% He flow for 1 h. The sample was cooled to room temperature under He flow prior to another spectra ( $\text{N}_2\text{O}+\text{H}_2\text{O}$  treatment). Finally, the sample was treated at 325  $^\circ\text{C}$  using 40%  $\text{CH}_4$  flow for 1 h prior to the spectra ( $\text{CH}_4$  treatment). The spectra range was selected as 200–1400 nm.

### 3.4 Reaction System and Procedure

The methane to methanol conversion reaction was carried out in a quartz tubular reactor having an inner diameter of 7 mm and an outer diameter of 9 mm. The reactor was mounted on a furnace and the furnace temperature was controlled using a temperature controller with a thermocouple placed on oven near the center of the catalyst bed. Zeolite powder was pelletized at 60 psi pressure for 4 minutes and sieved using a sieve to a particle size of 250–500  $\mu\text{m}$ . Particle size was an important parameter as it would affect both the pressure drop and the mass transfer rate. Zeolites were fixed in the reactor with the help of glass wool and placed in the middle of the furnace heating zone. The catalyst bed length was kept at approximately 0.9–1.3 cm. The flow rate of helium (Hatgaz, 99.999% purity), nitrous oxide (Hatgaz, 99%) and methane (Hatgaz, 99.995%) gases were controlled with separate mass flow controllers (ALICAT, MC-100SSCM-D).  $\text{H}_2\text{O}$  was introduced into the feed gas stream by directing the gas stream into a container of deionized water maintained at room temperature, resulting in a pressure of 3 kPa  $\text{H}_2\text{O}$  at 25 °C. All gas lines were heated to >60 °C to prevent any condensation. The effluent was directed to a gas chromatograph (GC, Agilent 7820A) equipped with a Pora-Plot Q column (CP7554, 25 m, 0.53 mm, 20  $\mu\text{m}$ ) and a CP-Molsieve 5Å column (CP7538, 25 m, 0.53 mm, 50  $\mu\text{m}$ ). Gas chromatograph (GC) was used for the quantification of methanol and other gases produced. The thermal conductivity detector and flame ionization detector were operated simultaneously to detect the products. Qualitative and quantitative analysis of  $\text{N}_2$ , CO,  $\text{CO}_2$ ,  $\text{N}_2\text{O}$ ,  $\text{CH}_4$ , dimethyl ether (DME),  $\text{C}_2\text{H}_6$ ,  $\text{C}_2\text{H}_4$ ,  $\text{C}_3\text{H}_6$ ,  $\text{C}_3\text{H}_4$ , and  $\text{C}_4+$  was performed using single-point calibration of a standard gas sample. Methanol calibration was performed by saturating inert He with methanol vapor at 25 °C and 0 °C.

Approximately 0.3 g of hydrated Cu-zeolite having a particle size of 250–500  $\mu\text{m}$  was placed in the quartz reactor. The heating of the catalyst was performed in two different ways. In the **reactant heating case**, a 100  $\text{cm}^3 \text{min}^{-1}$  feed gas containing different gas compositions of methane, nitrous oxide, water vapor and balance

helium was used to purge the catalyst at room temperature for 20 min. Then a single chromatogram was obtained to determine the feed gas concentrations. The reactor was then heated to the reaction temperature using a heating rate of 5 °C min<sup>-1</sup> and maintained at this temperature (usually 325 °C) during the reaction.

For the **helium heating case**, 100 cm<sup>3</sup> min<sup>-1</sup> He was used to heat the catalyst to the reaction temperature using a heating rate of 5 °C min<sup>-1</sup>. At the reaction temperature, the feed mixture was introduced to the catalyst and chromatogram was started to be taken. During the reaction, the reaction products were sent to the gas chromatograph at intervals of 21 minutes (approximately 16.5 minutes of working and 4.5 minutes of cooling) for MTM-2 GC method whereas 23 minutes (approximately 18 minutes of working and 5 minutes of cooling) for MTM-4 GC method. For all Cu-zeolites, the reaction temperature was chosen as 300–325 °C and the feed composition was 40 mol% CH<sub>4</sub>, 15% N<sub>2</sub>O, 0-9% H<sub>2</sub>O and balance He. As the temperature was increased, the partial pressure of H<sub>2</sub>O varied accordingly. For the reaction system, GHSV was 16000 h<sup>-1</sup>.

The previously established setup was used to regenerate the catalyst and to determine the coke amount. For the regeneration, dry air (Hatgaz, 99.99%) flow rate was set to 75 sccm and the spent catalyst was heat treated to 550 °C for 2 h using a heating rate of 5 °C min<sup>-1</sup>. The effluent CO<sub>2</sub> concentration was measured every 7 minutes using a gas chromatograph (Agilent 7820A). The total CO<sub>2</sub> amount was then computed to determine the overall coke amount. The overall coke amount was normalized using the total reaction time to calculate the coke generation rate. The computed coke rate was also considered in methane conversion rate and product

selectivity calculations. The equations for selectivity and conversions are provided in Equation 3.1-3, and the experimental setup is represented in Figure 3.1.

$$r_{\text{CH}_4} = r_{\text{CH}_3\text{OH}} + r_{\text{CO}_2} + r_{\text{CO}} + r_{\text{Coke}} + 2 \cdot \sum r_{\text{C}_2} + 3 \cdot \sum r_{\text{C}_3} + 4 \cdot \sum r_{\text{C}_4} \quad \text{Eqn. 3.1}$$

$$S_{\text{CH}_3\text{OH}}(\%) = \frac{r_{\text{CH}_3\text{OH}}}{r_{\text{CH}_4}} \cdot 100\% \quad \text{Eqn. 3.2}$$

$$X_{\text{CH}_4} = \frac{r_{\text{CH}_4}}{F_{\text{CH}_4, \text{fed}}} \cdot 100\% \quad \text{Eqn. 3.3}$$

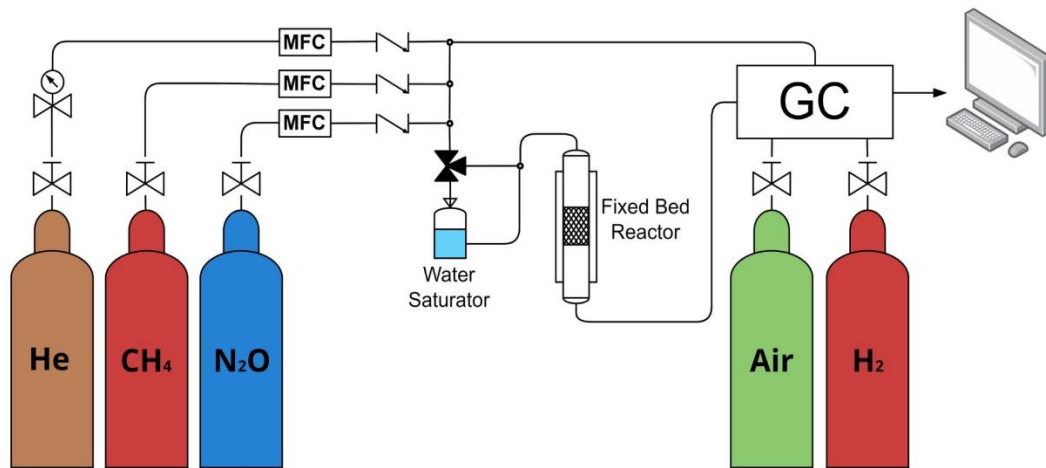


Figure 3.1. The schematic representation of reaction set-up

## CHAPTER 4

### RESULTS AND DISCUSSION

In this section, the characterization results of the catalysts are included, followed by the catalytic activity test results. Reaction test results are divided into two main headings (reactant heating and helium heating) and these processes are given chronologically. Our main purpose here is to show how we try to use the perspective of an engineer/scientist in the study timeframe and to explain why we do the experiments.

#### 4.1 Characterization Results

Within the scope of characterization results, analyses of ICP-OES for elemental analysis, XRD for crystal structure, SEM for morphology, TEM for metal particle size, N<sub>2</sub> physisorption at -196 °C for surface area, pore volume and isotherms, Raman and in-situ diffuse reflectance UV–Vis for active sites were carried out.

##### 4.1.1 Elemental Analysis

Table 4.1 shows the catalysts involved in the studies, the ion-exchange conditions, and resulting Cu/Al and Si/Al ratios. Micro/Meso/Nano gives information about the size of zeolite (Nano) or pore structure (Micro/Meso). CTABr or Steam represents preparation condition of mesoporous zeolite as mentioned Experimental Methodology section. If the catalyst is labeled R, this indicates that catalyst has been tested only using the reactant heating method which is explained in the Section 3.4. The number notation as \_1, \_2, \_3 or \_4 indicates copper amount of zeolite. Their notations generally are given as Cu/Al<0.03 named as \_1, 0.03< Cu/Al< 0.08 named as \_2 and 0.08< Cu/Al< 0.2 named as \_3, finally Cu/Al>0.2 noted as \_4. For the

same zeolite type, if there is more than one same range of Cu/Al ratio for notation; it is represented with the letter A,B,C, and D. Lastly, CuNa represents the catalyst that is exchanged with copper using the Na<sup>+</sup>-form of the zeolite.

Upon testing different starting Cu(II)-concentrations in the exchange solution, Micro-FER is found to be resistant to Cu(II)-exchange at 18 °C. The exchange capacity was improved by increasing the exchange temperature to 23 °C (Doubled Cu concentration with 5 °C temperature difference: Micro-Cu-FER\_1 vs Micro-Cu-FER\_2). Hence, it was found that increasing the temperature of the exchange solution was essential for higher Cu/Al loadings on Micro-FER. SSZ-39 and SSZ-13 were Cu(II)-exchanged under milder conditions compared to Micro-FER. Interestingly, it was also easier to Cu(II)-exchange Nano-FER (using lower Cu(II) concentrations at 18 °C) compared to Micro-FER. These differences are expected due to various parameters affecting the ion-exchange capacity. Different particle sizes of zeolites, different framework structure, ion-exchange solution temperature, mixing speed of the solution, purity of the ion-salts, the form or purity of the zeolites are some examples [122].

There are 18 examples in the Table 4.1. Nine of them were tested using reactant heating method. Micro-Cu-FER\_1 was tested with both reactant heating and helium heating. The remaining eight samples were tested for catalytic activity using helium heating method.

Table 4.1. Ion-exchange conditions and elemental analysis results using ICP-OES

<b>Sample</b>	<b>Solution Cu(II) Molarity</b>	<b>Ion- exchange Time</b>	<b>Ion-exchange Temperature</b>	<b>Resulting Si/Al</b>	<b>Resulting Cu/Al</b>	<b>mmol Cu*g cat<sup>-1</sup></b>
Micro-Cu-FER_2AR	0.006 M	24 h	18 °C	9.0	0.042	0.070
Micro-Cu-FER_2BR	0.012 M	24 h	18 °C	9.3	0.046	0.074
Micro-Cu-FER_2CR	0.03 M	24 h	18 °C	9.0	0.048	0.080
*Micro-CuNa-FER_2DR	0.006 M	24 h	18 °C	9.0	0.054	0.088
Micro-Cu-FER_3R	0.003 M	2.5 h	55 °C	8.5	0.089	0.155
Meso-Steam-Cu-FER_2CR	0.003 M	24 h	22 °C	10.4	0.048	0.070
Meso-CTABr-Cu-FER_3R	0.003 M	24 h	22 °C	6.5	0.144	0.314
Micro-Cu-SSZ-39_3R	0.003 M	24 h	18 °C	7.7	0.135	0.255
Micro-Cu-SSZ-39_4R	0.012 M	24 h	18 °C	7.6	0.359	0.668
Micro-Cu-FER_1	0.003 M	24 h	18 °C	8.8	0.024	0.041
Micro-Cu-FER_2	0.003 M	24 h	23 °C	9.3	0.045	0.072
Micro-Cu-FER_3	0.003 M	3 h	60 °C	9.1	0.137	0.223
Nano-Cu-FER_1	0.0002 M	2.5 h	18 °C	11.9	0.027	0.032

Table 4.1. Ion-exchange conditions and elemental analysis results using ICP-OES (Continued)

<b>Sample</b>	<b>Solution Cu(II) Molarity</b>	<b>Ion- exchange Time</b>	<b>Ion-exchange Temperature</b>	<b>Resulting Si/Al</b>	<b>Resulting Cu/Al</b>	<b>mmol Cu*g cat<sup>-1</sup></b>
Nano-Cu-FER_2	0.002 M	6 h	18 °C	13.1	0.065	0.084
Micro-Cu-SSZ-39_2	0.0003 M	3 h	22 °C	9.6	0.050	0.079
Micro-Cu-SSZ-39_3	0.0007 M	6 h	22 °C	9.1	0.115	0.188
Micro-Cu-SSZ-13_2	0.0003 M	3 h	22 °C	13.2	0.049	0.057
Micro-Cu-SSZ-13_3	0.0007 M	6 h	22 °C	12.6	0.142	0.173

\*Na/Al=0.212

## 4.1.2 X-Ray Diffraction Analysis

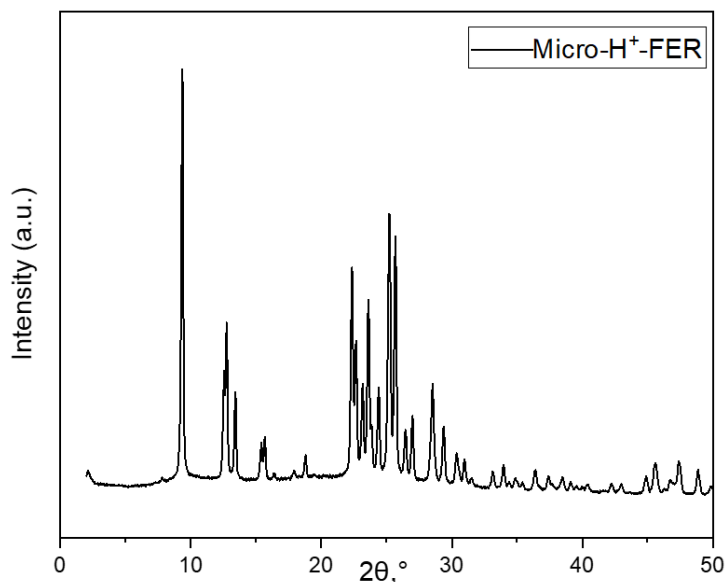


Figure 4.1. XRD pattern of Micro-H<sup>+</sup>-FER

Figure 4.1, Figure 4.2, Figure 4.3, and Figure 4.4 show the X-Ray Diffraction patterns of zeolites in H<sup>+</sup> form. Figure 4.1 shows the X-ray diffraction pattern of the Micro-H<sup>+</sup>-FER sample. When compared with the literature, it is observed that there is no extra phase in the structure. In the steam-treated sample given in Figure 4.2 (Meso-Steam-H<sup>+</sup>-FER), the obtained diffraction intensities show that the phases are similar to the sample in Figure 4.1 (Micro-H<sup>+</sup>-FER) or slightly reduced. The main reason for this is that the dealumination method aimed by the steam process has reduced the crystal size.

Among the 18 prepared samples, 9 of them were tested for activity by reactant heating and sent to XRD before copper addition. Due to the low amount of copper addition, there were no extra peaks in XRD and no change was observed. XRD patterns before and after copper addition can be seen in Figure 4.5, Figure 4.7, Figure 4.8, Figure 4.9.

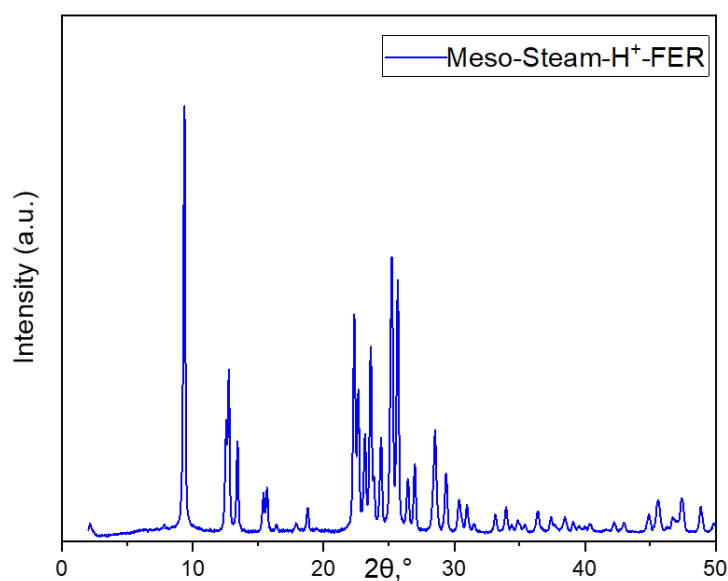


Figure 4.2. XRD pattern of Meso-Steam-H<sup>+</sup>-FER

In the mesoporegen-containing sample in Figure 4.3 (Meso-CTABr-H<sup>+</sup>-FER), both a significant decrease in intensity and an extra diffraction at 2.2° was observed. The d-spacing corresponding to that 2.2 2θ° was found to be 3.96 nm (approximately 4 nm) in the calculation from the Bragg diffraction law. This situation can also be understood by N<sub>2</sub> adsorption. When the literature was examined, it was suggested that the phase formed at this point may be a mesoporous aluminosilicate similar to MCM-41 [123].

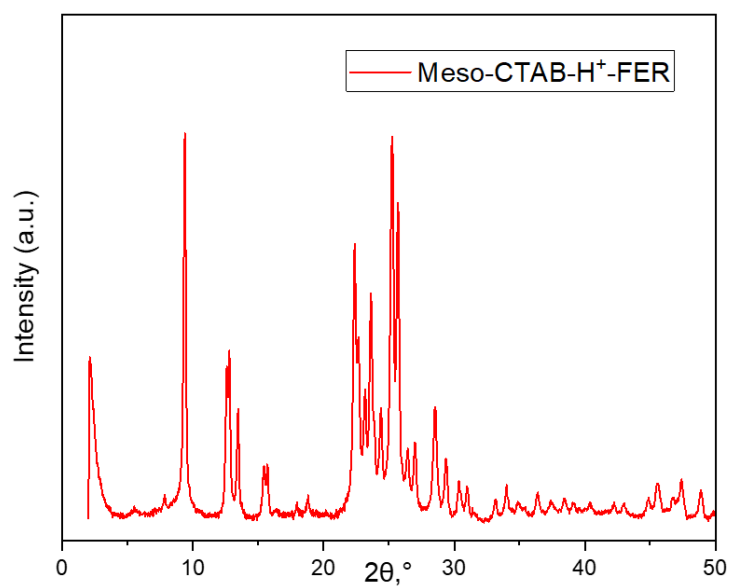


Figure 4.3. XRD pattern of Meso-CTABr-H<sup>+</sup>-FER

The X-ray diffraction pattern of Micro-H<sup>+</sup>-SSZ-39 in Figure 4.4 shows the same diffractions as the AEI frame structure, no extra phase was observed. However, an extra zeolitic phase in low concentrations was detected later using SEM.

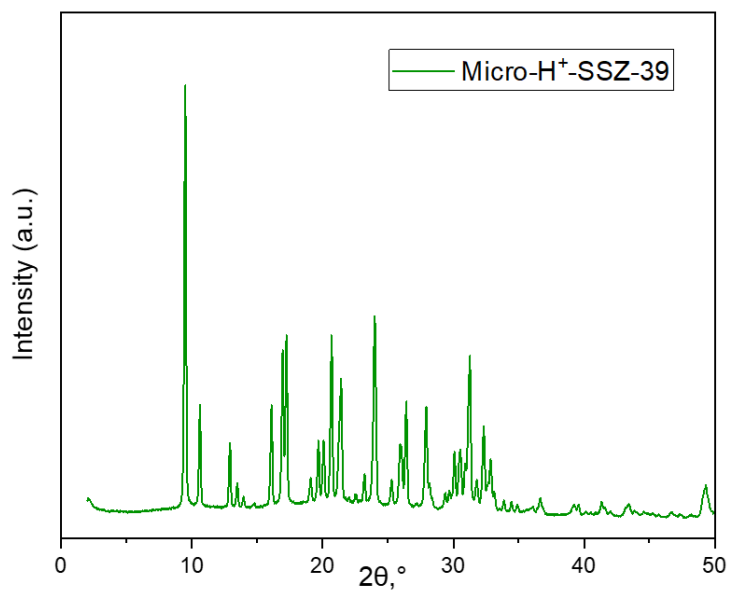


Figure 4.4. XRD pattern of Micro-H<sup>+</sup>-SSZ-39

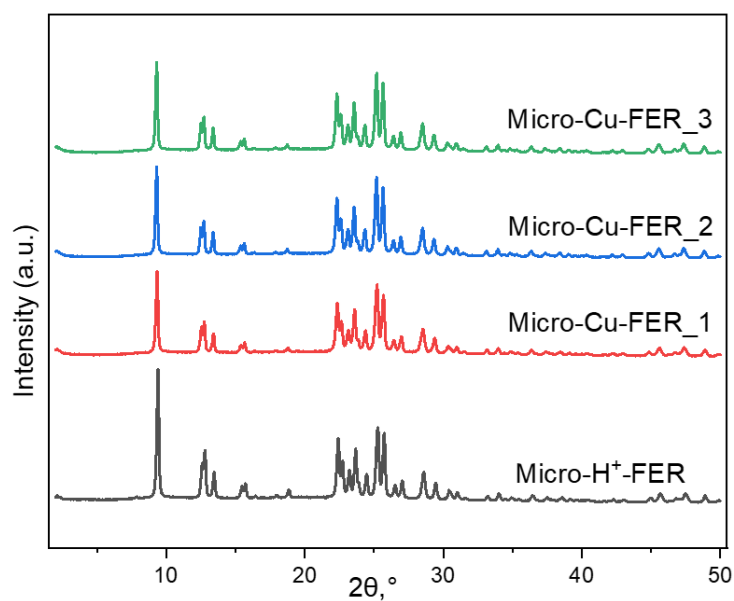


Figure 4.5. XRD patterns of Micro-H<sup>+</sup>-FER and Micro-Cu-FER samples

In the XRD patterns given in Figure 4.5, no differences in the peaks before and after copper exchange were observed as mentioned earlier. No extra phase in FER was observed in all samples. Figure 4.6 shows the XRD pattern of Nano-FER. The lower intensity compared to Micro-FER indicates lower zeolite particle size as expected. No change was observed here as a result of the copper-exchange.

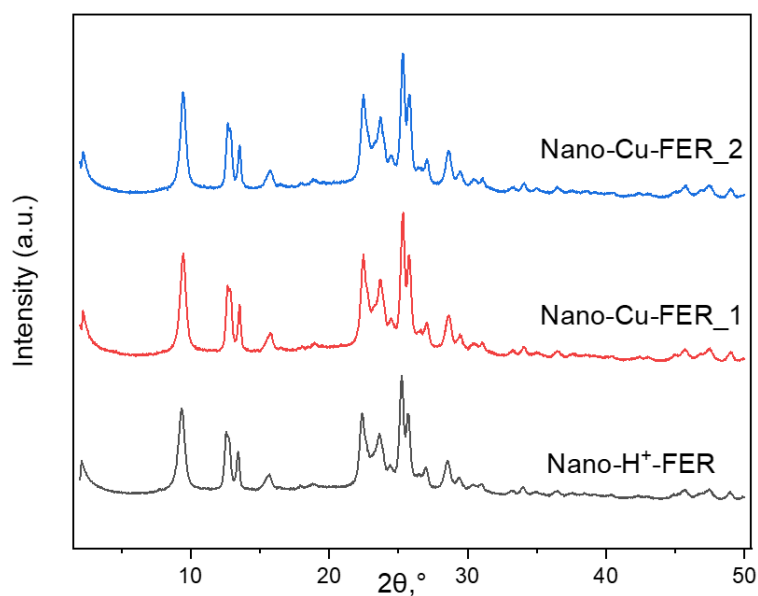


Figure 4.6. XRD patterns of Nano-H<sup>+</sup>-FER and Nano-Cu-FER samples

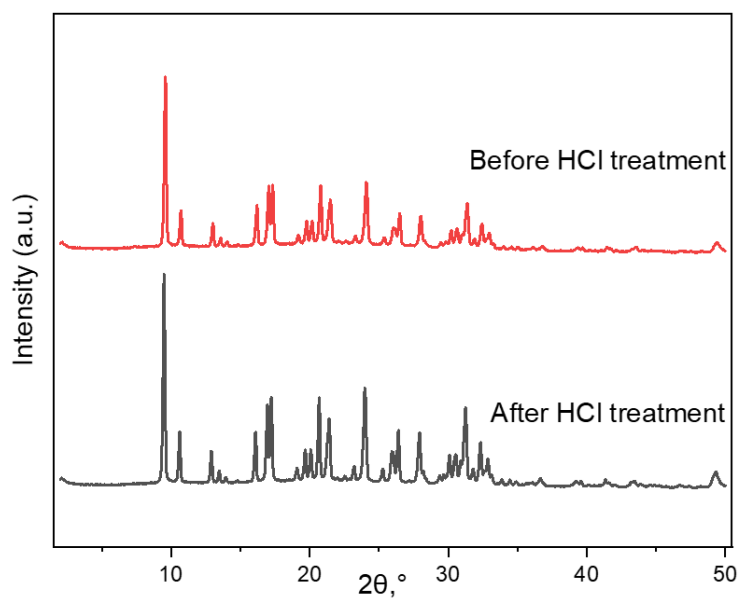


Figure 4.7. XRD patterns of Micro-H<sup>+</sup>-SSZ-39 before and after HCl treatment

Figure 4.7 shows the effect of HCl treatment on SSZ-39. No disappearance of AEI structure nor addition of new phases was observed, but an increase in the intensity was observed after treatment. This shows that the crystallinity in the structure increases. Figure 4.8 also shows SSZ-39 loaded with copper and no change was observed.

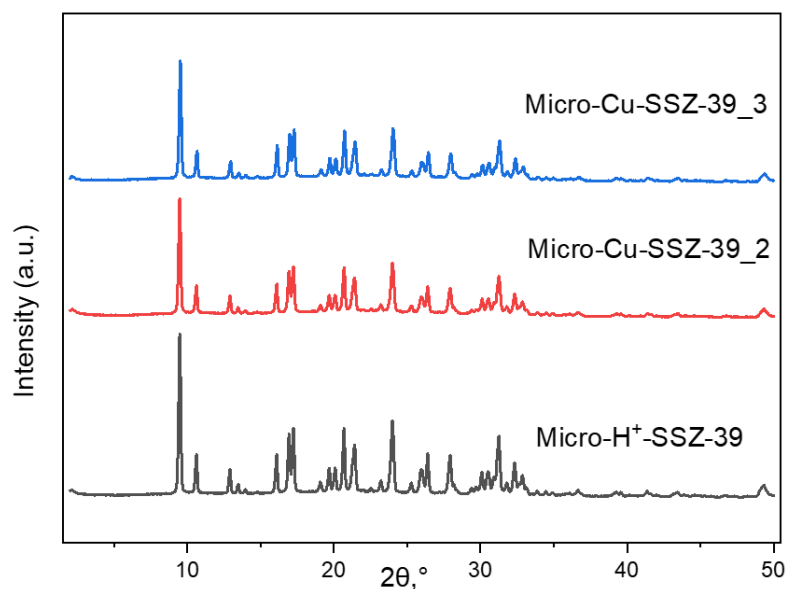


Figure 4.8. XRD patterns of Micro-H<sup>+</sup>-SSZ-39 and Micro-Cu-SSZ-39 samples

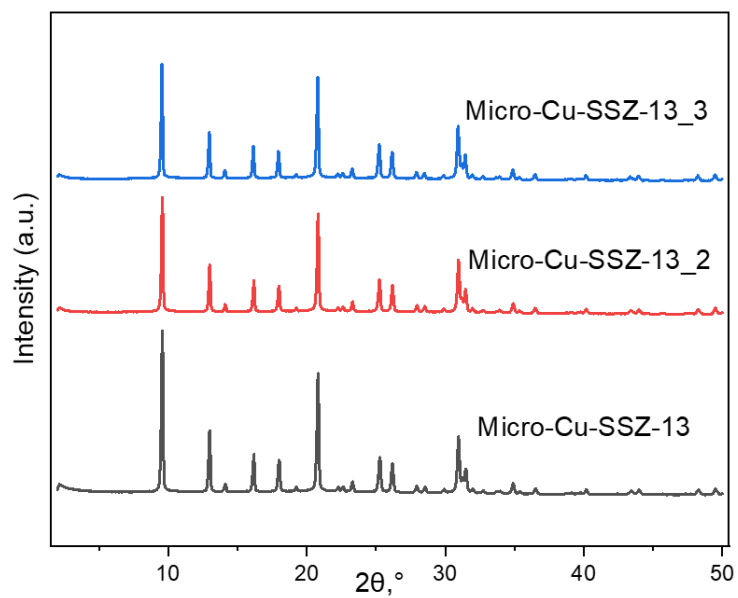


Figure 4.9. XRD patterns of Micro-H<sup>+</sup>-SSZ-13 and Micro-Cu-SSZ-13 samples

Figure 4.9 shows the SSZ-13 (CHA) sample before and after copper exchange. No extra phase was observed. No change was observed after the addition of copper.

### 4.1.3 SEM Analysis

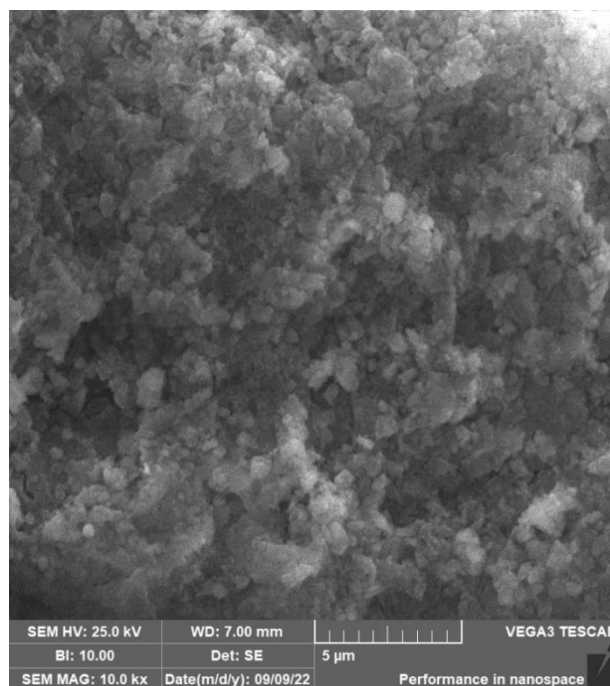


Figure 4.10. SEM Image of Micro-H<sup>+</sup>-FER

Figure 4.10, Figure 4.11, and Figure 4.12 show the SEM images of the 3 zeolites. Particle sizes between 200 nm and 2 μm were calculated in the Micro-H<sup>+</sup>-FER structure with the average of about 20 measurements taken from different regions. Similarly, values between 150 nm and 1.7 μm were observed in the Meso-Steam-H<sup>+</sup>-FER (Figure 4.11) structure. Based on previous characterization methods in the Meso-CTABr-H<sup>+</sup>-FER (Figure 4.12) sample, evidence for the formation of a mesoporous structure similar to the MCM-41 structure was expected. The MCM-41 structure, which has an SEM image in the form of curved circles in the literature [124].

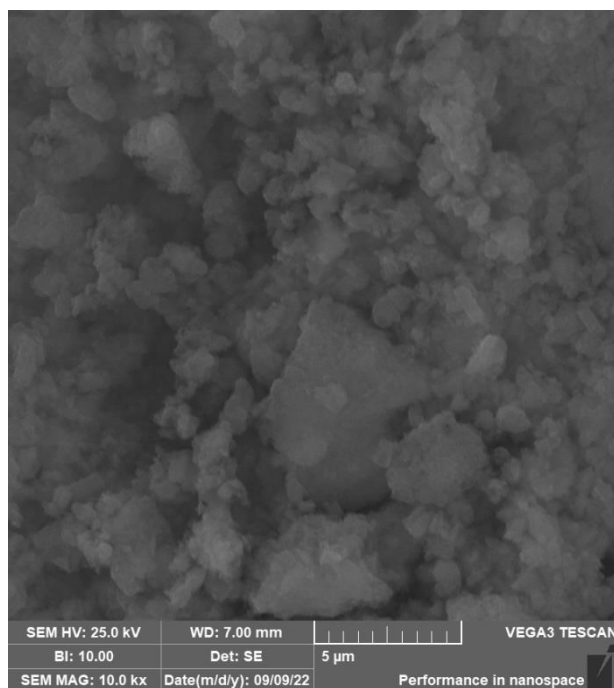


Figure 4.11. SEM Image of Meso-Steam-H<sup>+</sup>-FER

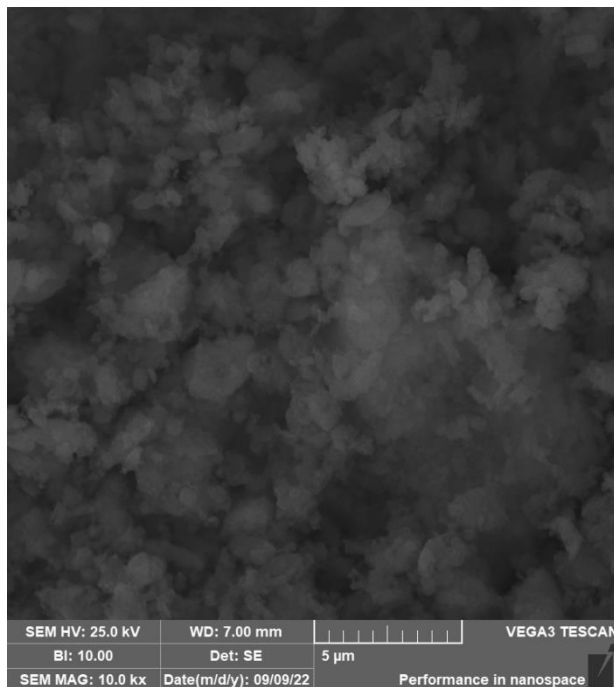


Figure 4.12. SEM Image of Meso-CTABr-H<sup>+</sup>-FER

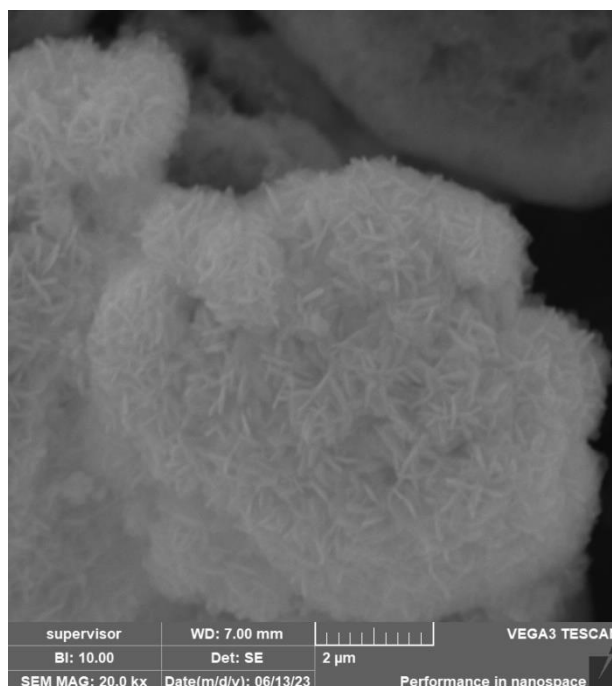


Figure 4.13. SEM Image of Nano-H<sup>+</sup>-FER

According to the SEM image, Nano-H<sup>+</sup>-FER showed sheet-like morphology with 200–400 nm thickness.

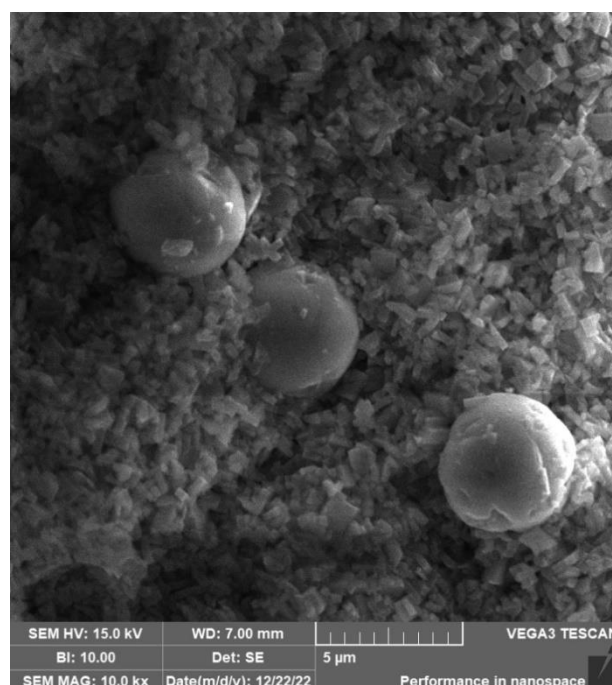


Figure 4.14. SEM Image of Micro-H<sup>+</sup>-SSZ-39 before HCl treatment

When the SSZ-39 structure was examined by SEM, ANA phase in the form of large round balls (ca. 3  $\mu\text{m}$ ) was observed in the structure before HCl treatment (Figure 4.14). Since the concentration of these structures were probably below the XRD detection limit, they could not be detected by XRD. However, in the SEM analysis performed after the treatment with HCl (Figure 4.15), the ANA phase was found much less in the images taken from more than 20 regions compared to before treatment. SSZ-39 possesses rhombohedral morphology with crystal size around 1  $\mu\text{m}$ .

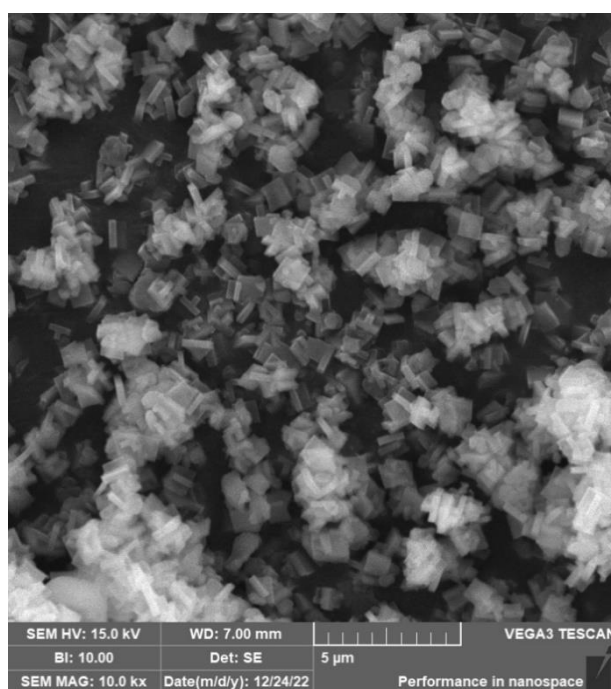


Figure 4.15. SEM Image of Micro- $\text{H}^+$ -SSZ-39 after HCl treatment

SSZ-13 showed elliptical crystals of sizes approximately 2  $\mu\text{m}$  as can be seen from Figure 4.16.

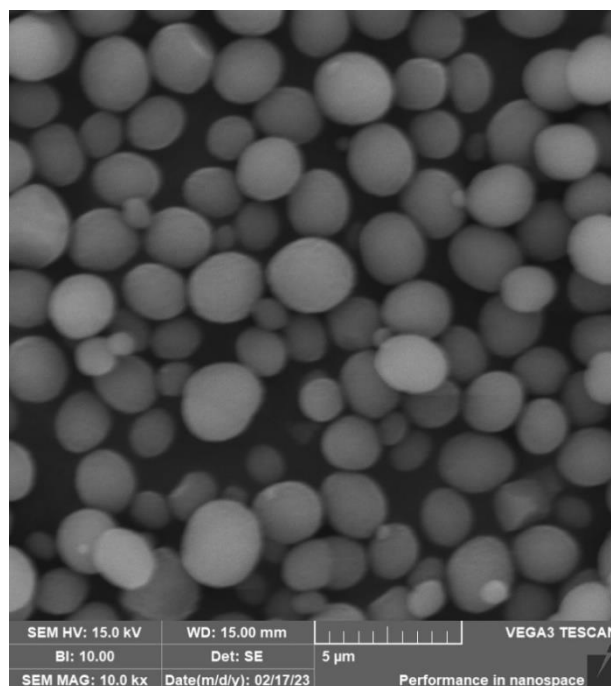


Figure 4.16. SEM Image of Micro-H<sup>+</sup>-SSZ-13

#### 4.1.4 TEM Analysis

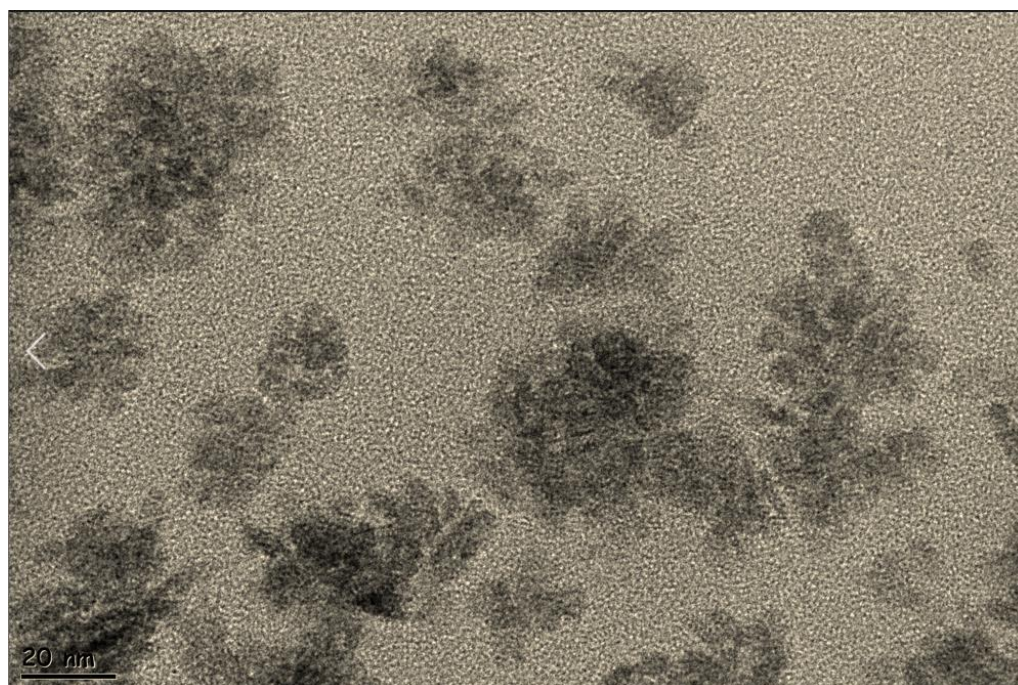


Figure 4.17. HR-TEM Image of fresh Micro-Cu-FER\_1

In order to understand the catalysts in fresh and post regeneration states, the catalysts in fresh and post regeneration states were characterized by High Resolution TEM. TEM images of the fresh state of Micro-Cu-FER\_1 catalyst is given in Figure 4.17. Post regeneration images can also be seen in Figure 4.18. It can be seen that the samples before and after regeneration have similar morphologies if glass wool (black long lines, Figure 4.18) is ignored. Despite the low copper content in the fresh Micro-Cu-FER\_1, darker regions ranging from 6 to 11 Å can be considered as copper oligomers. In the same sample after regeneration shown in Figure 4.18, there are Cu particles between 6 and 11 Å, while very rare darker regions of 16 Å may also indicate coalesced Cu particles. However, in most of the sample there are no regions that could be evidence of copper sintering (Figure 4.18). This may also be due to the very low Cu concentration.

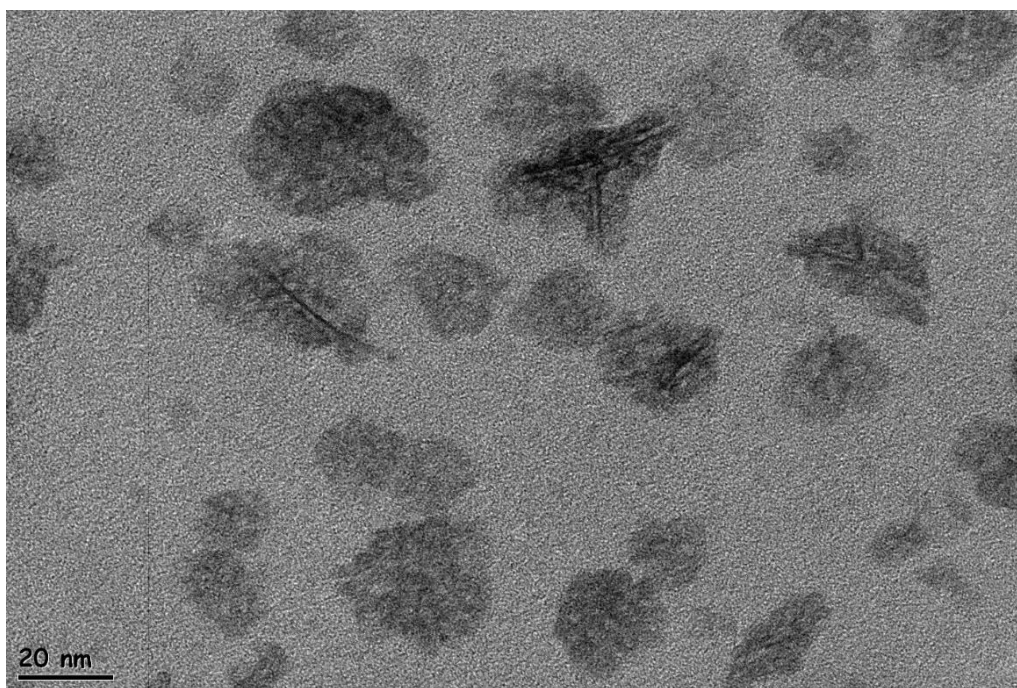


Figure 4.18. HR-TEM Image of Micro-Cu-FER\_1 after reaction

Since such a situation was observed at low copper content, the pre- (fresh) and post-reaction states of Micro-Cu-SSZ-39\_3 were also sent to HR-TEM. However, no functional image could be taken from the post-reaction state due to the equipment problem. As can be seen from Figure 4.19, copper particles of about 4 nm in size

were observed. There are studies in the literature that CuO formation is observed especially in zeolites with Cu/Al ratio above 0.1 [101], [114]. These studies were also supported by d-spacing calculations. In the calculations, the d-spacing of these particles was calculated to be 0.26 nm (see Figure 4.19) with the help of Image J. In the literature, these data were found to belong to the (111) plane of CuO nanoparticles [125].

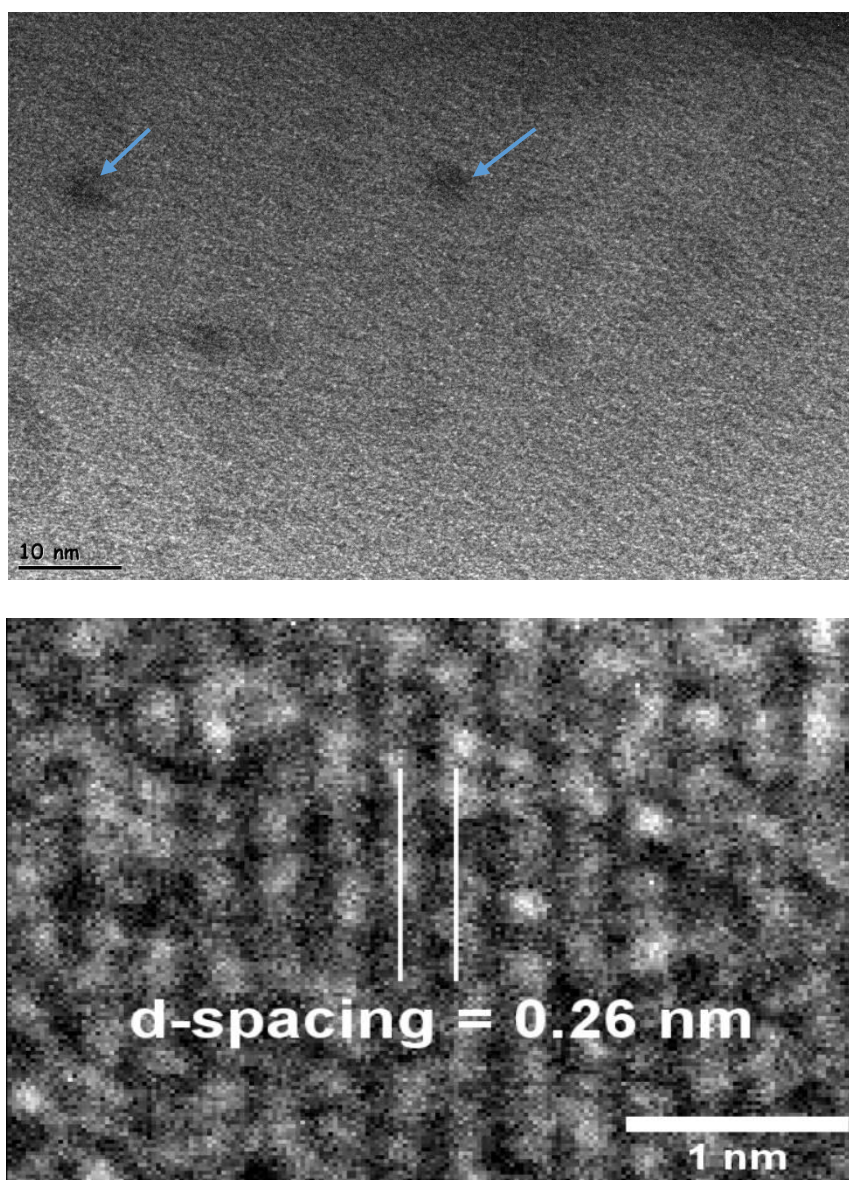


Figure 4.19. HR-TEM Image of fresh Micro-Cu-SSZ-39\_3 (above) and d-spacing calculations (below)

## 4.1.5 N<sub>2</sub> Physisorption at -196°C Analysis

### 4.1.5.1 N<sub>2</sub> Adsorption & Desorption Isotherms

All prepared samples were also analyzed with N<sub>2</sub> adsorption and desorption analysis. N<sub>2</sub> adsorption-desorption isotherms of Micro-H<sup>+</sup>-FER, Meso-Steam-H<sup>+</sup>-FER, Meso-CTABr-H<sup>+</sup>-FER are given in Figure 4.20, Figure 4.21, and Figure 4.22, respectively. Micro-H<sup>+</sup>-FER and Meso-Steam-H<sup>+</sup>-FER samples mainly showed features of Type I isotherm (with few features of Type IV isotherm with H4 hysteresis loop) due to the presence of both micropores and mesopores. However, Meso-CTABr-H<sup>+</sup>-FER sample mainly showed the combined features of Type I and IV due to its mesoporous structure [126].

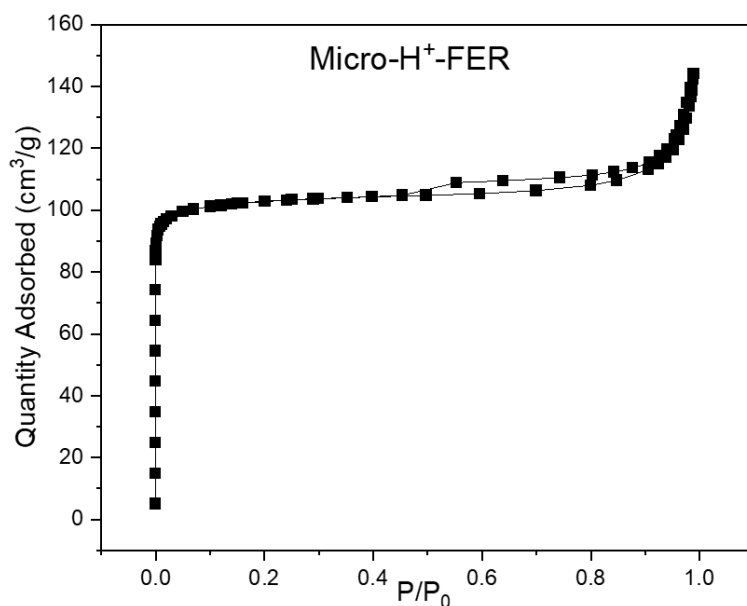


Figure 4.20. N<sub>2</sub> adsorption/desorption isotherms of Micro-H<sup>+</sup>-FER

N<sub>2</sub> adsorption-desorption isotherms of copper-containing micro-sized FER samples are illustrated in Figure 4.24. Similarly, they all showed the features of both Type I and Type IV isotherms.

SSZ-39 and SSZ-13 samples showed only the features of Type I isotherms (see Figure 4.23, Figure 4.26 and Figure 4.27) due to their microporous structure in

accordance with pore volume information given in Table 4.2. Additionally, the N<sub>2</sub> adsorption and desorption isotherms of copper-containing nano-sized FER samples also showed both Type I and Type IV isotherms (see Figure 4.25) because of their microporous structure as well as their highly mesoporous structure.

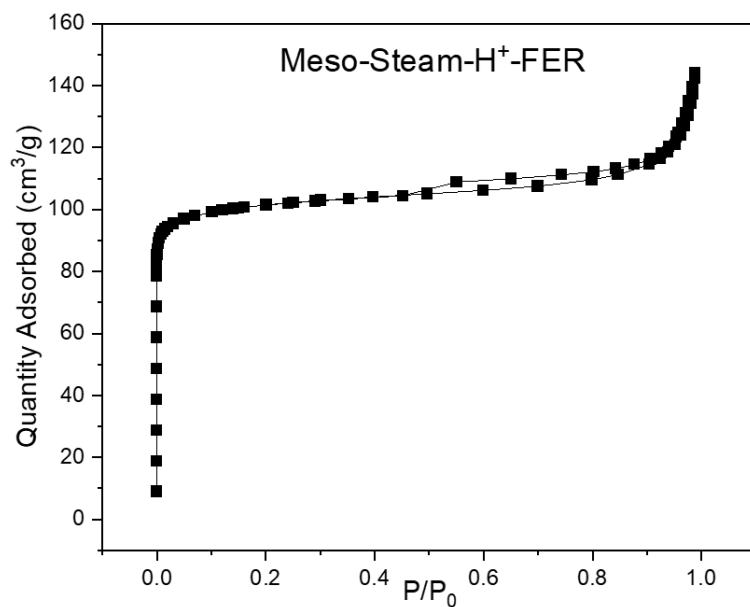


Figure 4.21. N<sub>2</sub> adsorption/desorption isotherms of Meso-Steam-H<sup>+</sup>-FER

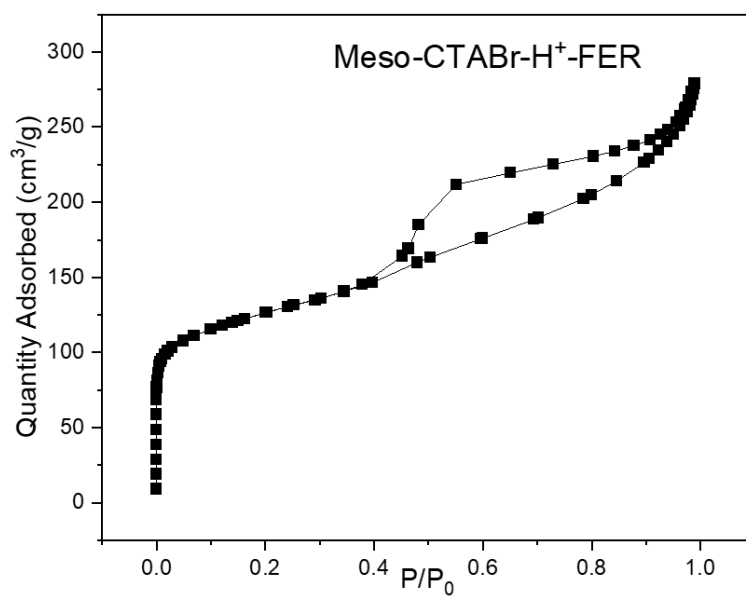


Figure 4.22. N<sub>2</sub> adsorption/desorption isotherms of Meso-CTABr-H<sup>+</sup>-FER

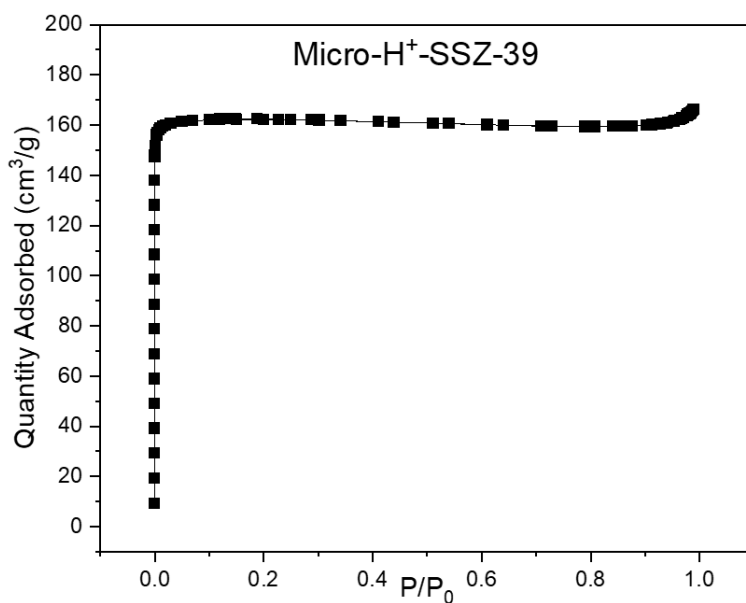


Figure 4.23. N<sub>2</sub> adsorption/desorption isotherms of Micro-H<sup>+</sup>-SSZ-39

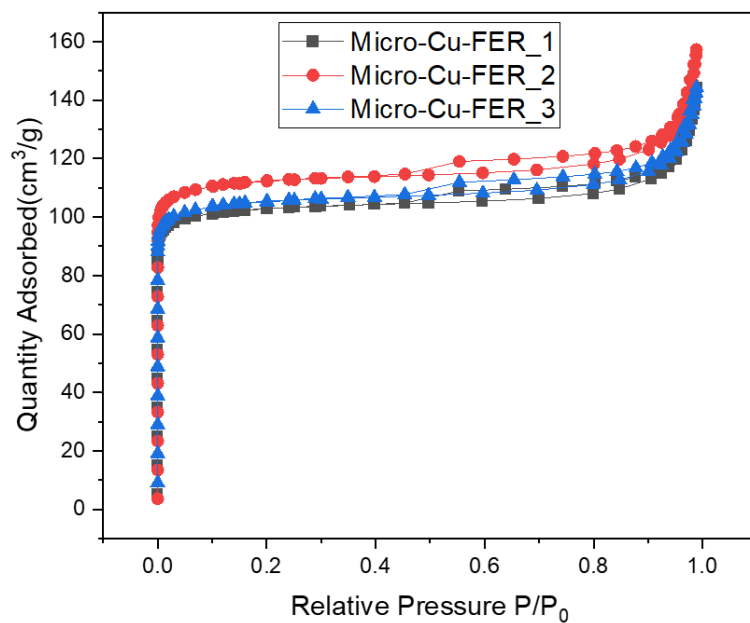


Figure 4.24. N<sub>2</sub> adsorption/desorption isotherms of Micro-Cu-FER

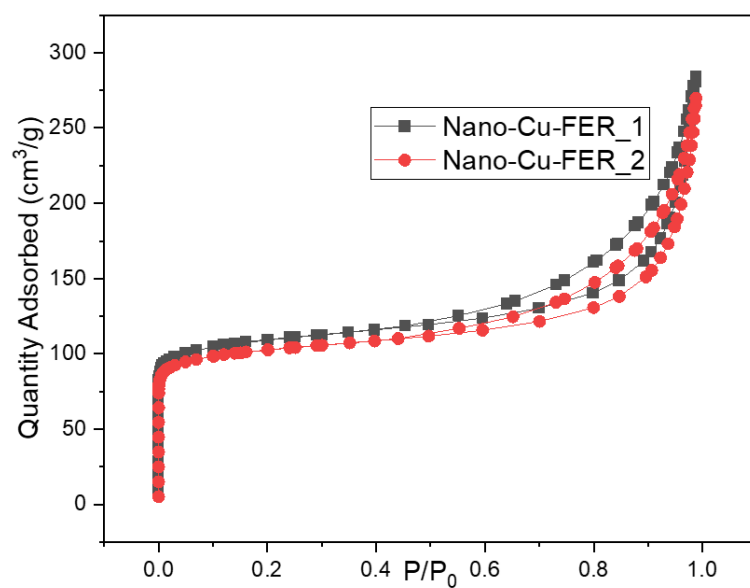


Figure 4.25. N<sub>2</sub> adsorption/desorption isotherms of Nano-Cu-FER

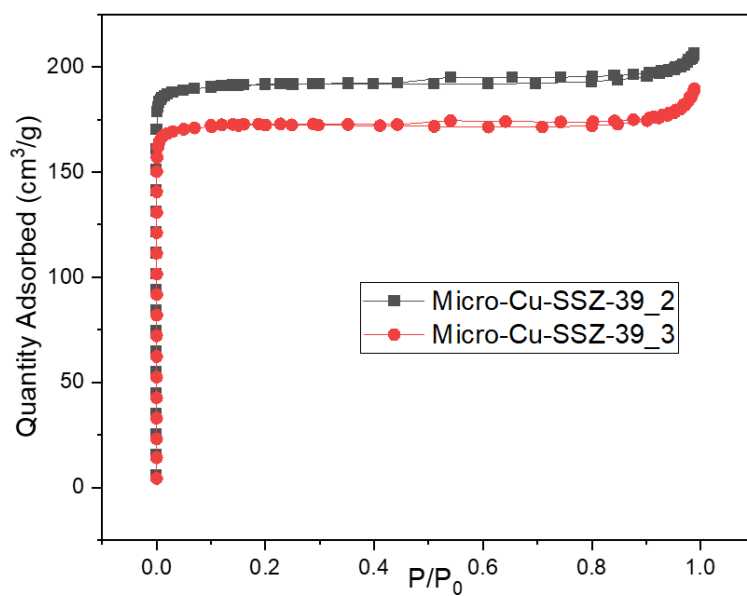


Figure 4.26. N<sub>2</sub> adsorption/desorption isotherms of Micro-Cu-SSZ-39

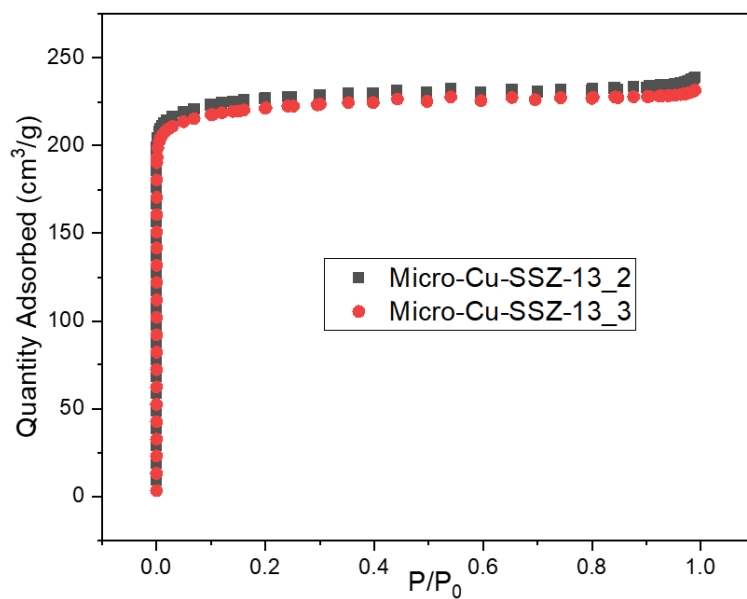


Figure 4.27. N<sub>2</sub> adsorption/desorption isotherms of Micro-Cu-SSZ-13

#### 4.1.5.2 Surface Area and Pore Volume

The surface area and pore volume values of samples are given in Table 4.2. As it can be seen from Table 4.2, among the post-synthesis treatments applied on commercial H<sup>+</sup>-FER, the treatment with CTABr showed increased mesopore volume (from 0.07 cm<sup>3</sup>/g to 0.33 cm<sup>3</sup>/g), while steam treatment did not affect the mesopore volume. Additionally, the copper-exchange to H<sup>+</sup>-FER did not change the pore volume and the surface area of the samples.

Table 4.2. Surface area and pore volume of samples

Catalyst/Zeolite	Langmuir	BET	V <sub>Total</sub> (cm <sup>3</sup> /g)	V <sub>Micro</sub> (cm <sup>3</sup> /g)	V <sub>Meso</sub> (cm <sup>3</sup> /g)
	Surface Area (m <sup>2</sup> /g)	Surface Area (m <sup>2</sup> /g)			
Micro-H <sup>+</sup> -FER	451	306	0.21	0.14	0.07
Meso-Steam-H <sup>+</sup> -FER	447	304	0.21	0.13	0.08
Meso-CTABr-H <sup>+</sup> -FER	583	410	0.42	0.09	0.33
Micro-H <sup>+</sup> -SSZ-39	706	475	0.26	0.25	0.01
Micro-Cu-FER_1	452	306	0.21	0.15	0.06
Micro-Cu-FER_2	493	334	0.23	0.16	0.07
Micro-Cu-FER_3	462	313	0.21	0.15	0.06
Nano-Cu-FER_1	488	335	0.41	0.13	0.28
Nano-Cu-FER_2	458	314	0.39	0.12	0.27
Micro-Cu-SSZ-39_2	834	565	0.32	0.29	0.03
Micro-Cu-SSZ-39_3	751	509	0.29	0.26	0.03
Micro-Cu-SSZ-13_2	995	676	0.37	0.32	0.05
Micro-Cu-SSZ-13_3	971	662	0.36	0.31	0.05

Nano-Cu-FER synthesized with hydrothermal method showed similar surface area and micropore volume values with commercial FER zeolite, while its mesopore

volume ( $\approx 0.3 \text{ cm}^3/\text{g}$ ) was significantly higher than commercial one ( $0.07 \text{ cm}^3/\text{g}$ ). Moreover, Table 4.2 showed that SSZ-39 samples have microporous structure as their mesopore volumes are almost zero.

#### 4.1.5.3 Pore Size Distributions

The pore size distributions of parent and treated (with steam and CTABr) Micro-FER samples are given in Figure 4.28, Figure 4.29 and Figure 4.30, respectively. As shown in the pore size distributions of Micro- $\text{H}^+$ -FER and Meso-Steam- $\text{H}^+$ -FER, these two samples mainly consist of micropores (with pore sizes of  $< 2 \text{ nm}$ ) and a few amounts of mesopores located at around  $20 \text{ nm}$ . However, Meso-CTABr- $\text{H}^+$ -FER sample showed newly formed mesopores at around  $2, 4$  and  $6 \text{ nm}$ , indicating the success of CTABr treatment for mesopore formation in the micro-sized FER sample.

The pore size distributions of Cu-containing FER zeolites (see Figure 4.24) also showed similar distributions with Micro- $\text{H}^+$ -FER and Meso-Steam- $\text{H}^+$ -FER, not showing mesopores. Additionally, the pore size distributions of zeolites SSZ-39 and SSZ-13 did not show mesopore distributions as shown in Figure 4.23, Figure 4.26, Figure 4.27, confirming its microporous structure similar to previous results.

Lastly, copper-containing nanosized FER samples showed pore distributions at around  $40\text{-}50 \text{ nm}$  (see Figure 4.33) most likely due to the intra-crystalline structure of the nano-sized FER.

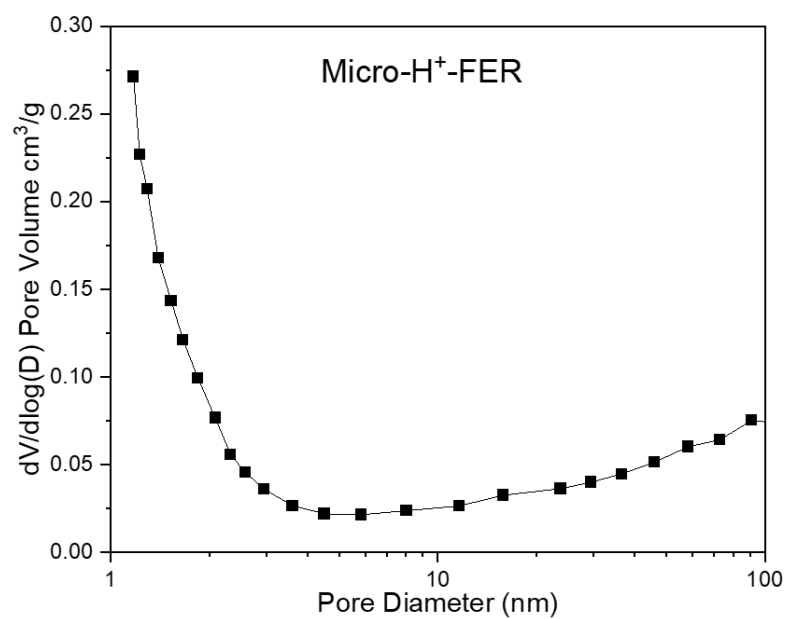


Figure 4.28. BJH adsorption pore size distribution of Micro-H<sup>+</sup>-FER

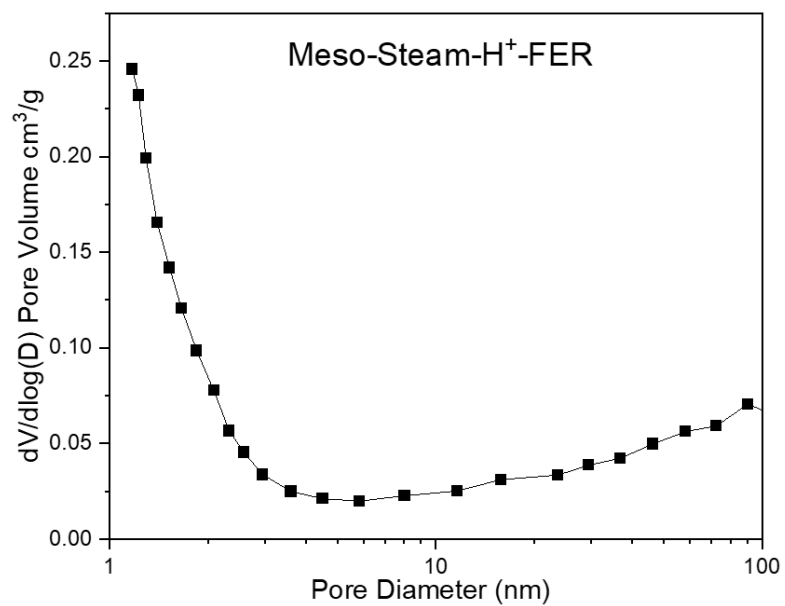


Figure 4.29. BJH adsorption pore size distribution of Meso-Steam-H<sup>+</sup>-FER

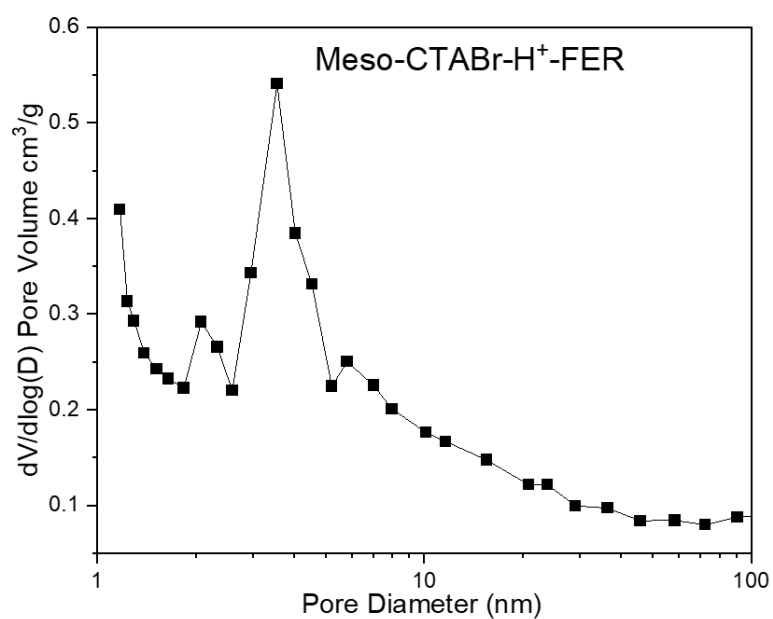


Figure 4.30. BJH adsorption pore size distribution of Meso-CTABr-H<sup>+</sup>-FER

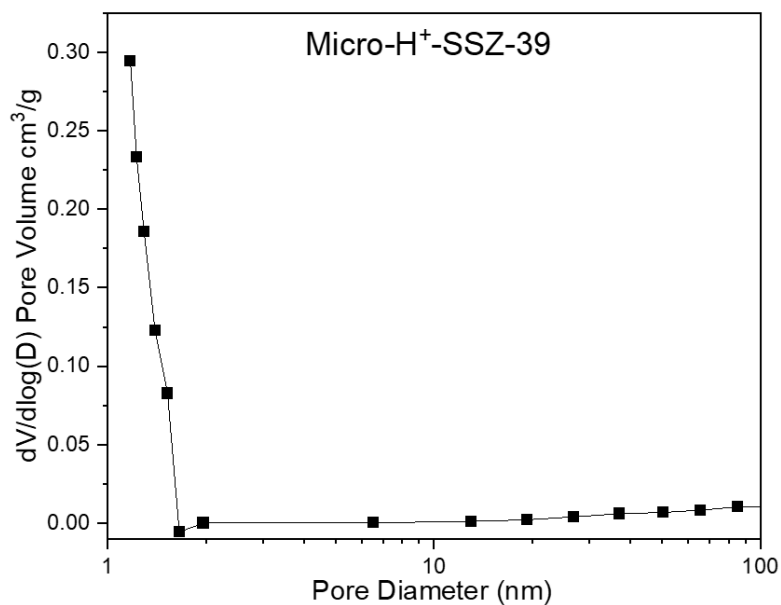


Figure 4.31. BJH adsorption pore size distribution of Micro-H<sup>+</sup>-SSZ-39

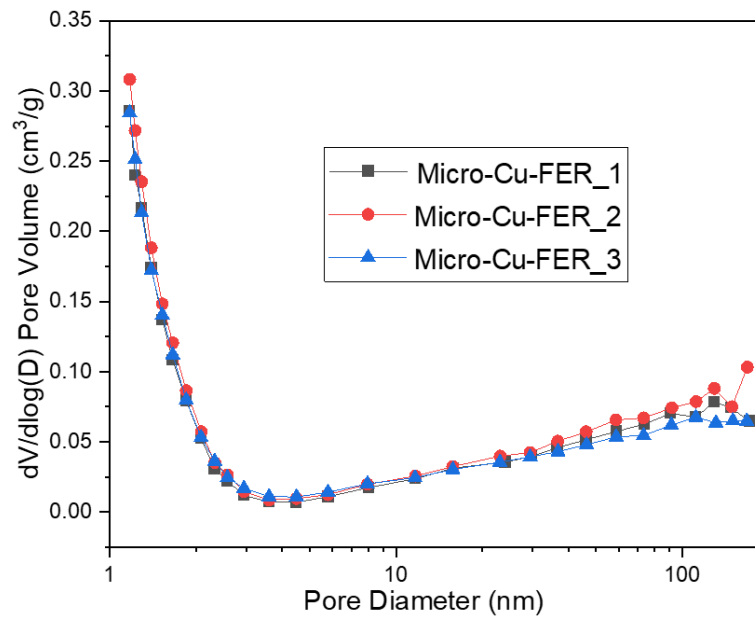


Figure 4.32. BJH adsorption pore size distributions of Micro-Cu-FER

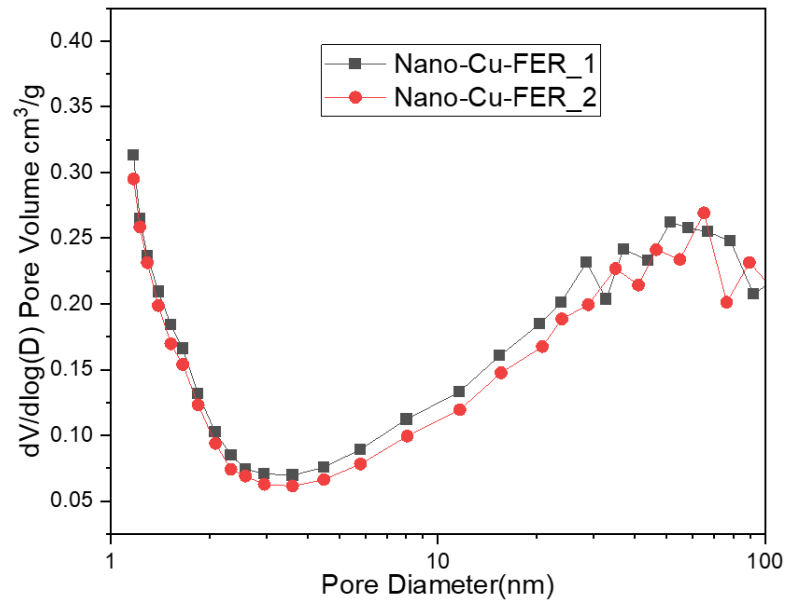


Figure 4.33. BJH adsorption pore size distributions of Nano-Cu-FER

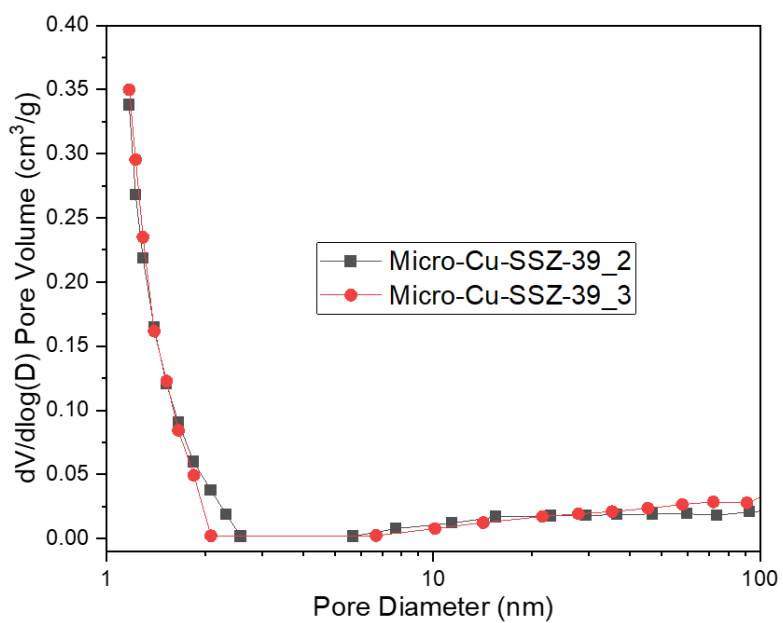


Figure 4.34. BJH adsorption pore size distributions of Micro-Cu-SSZ-39

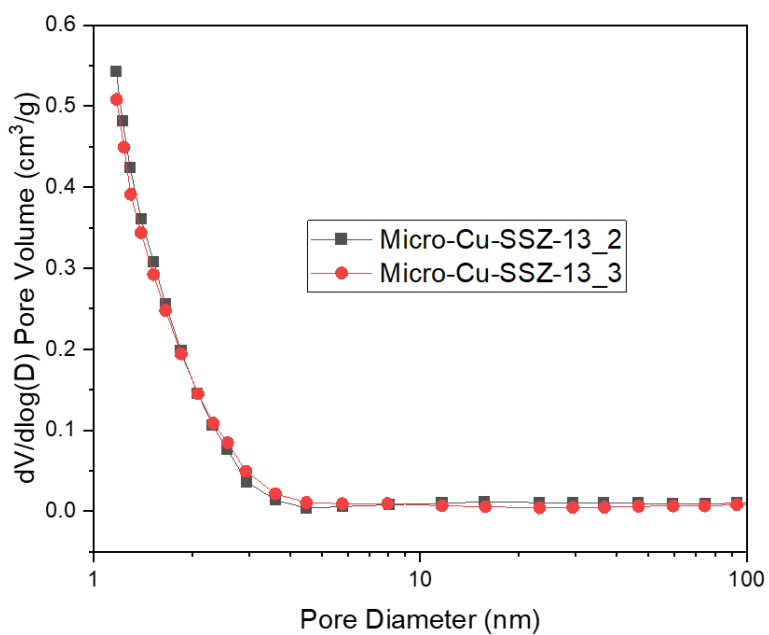


Figure 4.35. BJH adsorption pore size distributions of Micro-Cu-SSZ-13

#### 4.1.6 $^{27}\text{Al}$ MAS NMR

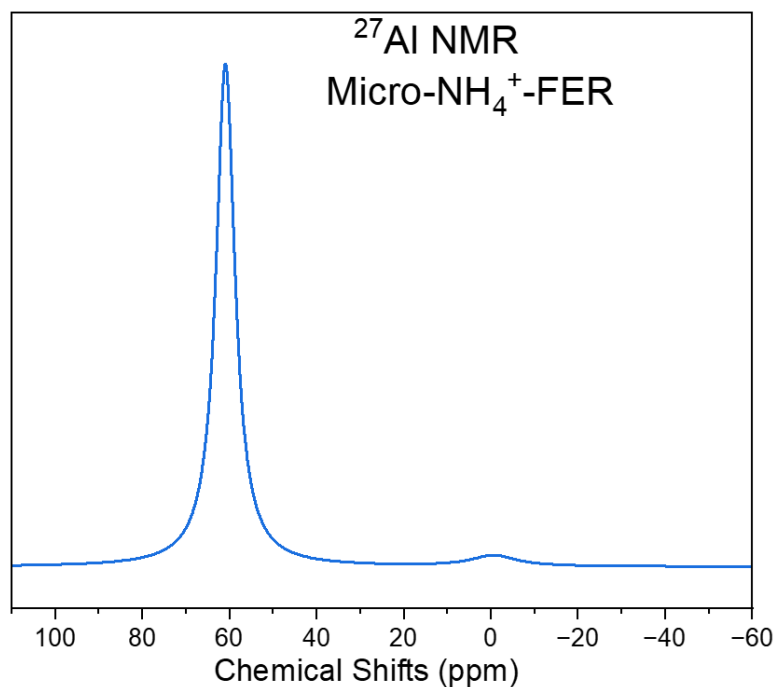


Figure 4.36.  $^{27}\text{Al}$ -MAS-NMR Spectra of Micro- $\text{NH}_4^+$ -FER

Figure 4.36, Figure 4.37 and Figure 4.38 show the  $^{27}\text{Al}$  MAS NMR plots of Micro- $\text{NH}_4^+$ -FER, Meso-Steam- $\text{NH}_4^+$ -FER, Micro- $\text{NH}_4^+$ -SSZ-39. In Figure 4.36 and Figure 4.37, the FER structures have peaks at about 60 ppm. This indicates the tetrahedral coordinated Al sites in the framework structure of the zeolite. However, Figure 4.37 shows Al sites located outside the framework structure of the zeolite (extra framework Al sites). This peak at about 0 ppm means that aluminum species in the sample are six coordinated to oxygen. After calculating the areas on both sides with the help of the integral, 28% of the Al sites were found to be outside the structure. The Si/Al value in Table 4.1 calculated for Meso-Steam- $\text{NH}_4^+$ -FER with ICP-OES is 10.4. However, when we consider the extra framework Al content, Si/ $\text{Al}_F$  ( $\text{Al}_F$ : framework Al) value becomes 14.4.

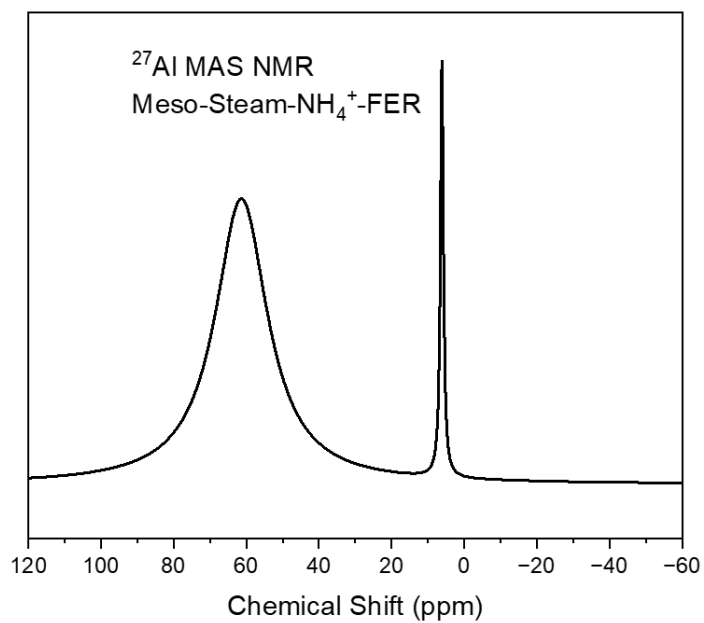


Figure 4.37.  $^{27}\text{Al}$ -MAS-NMR Spectra of Meso-Steam-NH<sub>4</sub><sup>+</sup>-FER

Figure 4.38 shows a similar peak at approximately 63 ppm. In addition, no extra framework Al sites were observed by  $^{27}\text{Al}$  MAS NMR for Micro-NH<sub>4</sub><sup>+</sup>-SSZ-39.

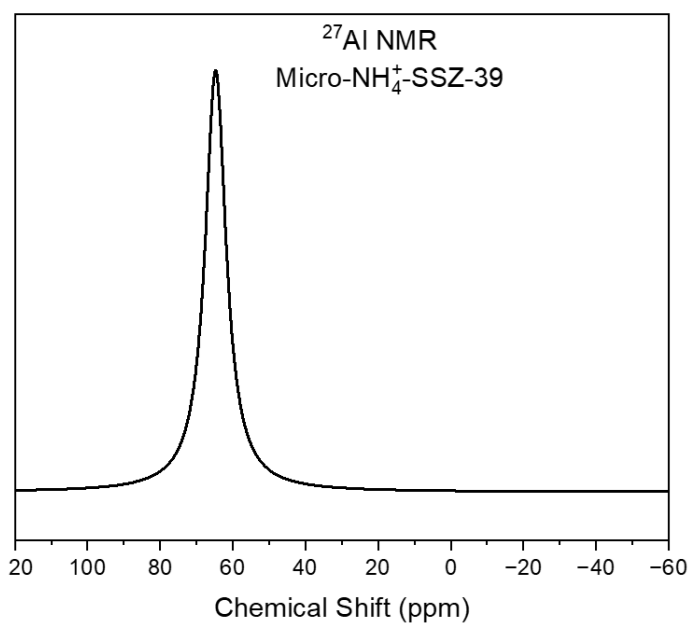


Figure 4.38.  $^{27}\text{Al}$ -MAS-NMR Spectra of Micro- $\text{NH}_4^+$ -SSZ-39

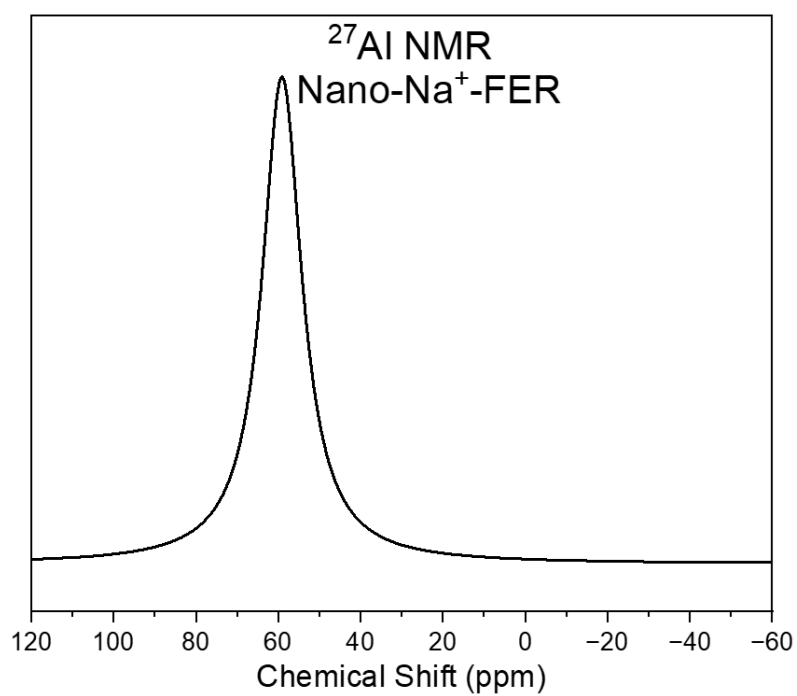


Figure 4.39.  $^{27}\text{Al}$ -MAS-NMR Spectra of Nano- $\text{Na}^+$ -FER

For the Nano- $\text{Na}^+$ -FER, Figure 4.39, similar peak at approximately 60 ppm. In addition, no off-structure Al sites were observed by  $^{27}\text{Al}$  MAS NMR for Nano- $\text{Na}^+$ -FER.

The percentage of Al in the framework ( $Al_{IV}$  and  $Al_V$ ) for these two zeolites (Micro-FER and Nano-FER) was determined by deconvolution (see Appendix A) of the  $^{27}Al$  MAS NMR spectra (40-70 ppm for  $Al_{IV}$ , 20-40 ppm for  $Al_V$ ) and it was found that 90.8% and 100% respectively. It is commonly known that  $Al_F$  can be divided into two categories: Al pairs ( $Al_p$ ) and isolated Al atoms ( $Al_i$ ). An interval of less than three (-Si-O-) groups separates the two Al atoms in one ring is represented by the  $Al_p$ , which can be balanced by  $Co^{2+}$  cations [127]

#### 4.1.7 $^{29}Si$ MAS NMR

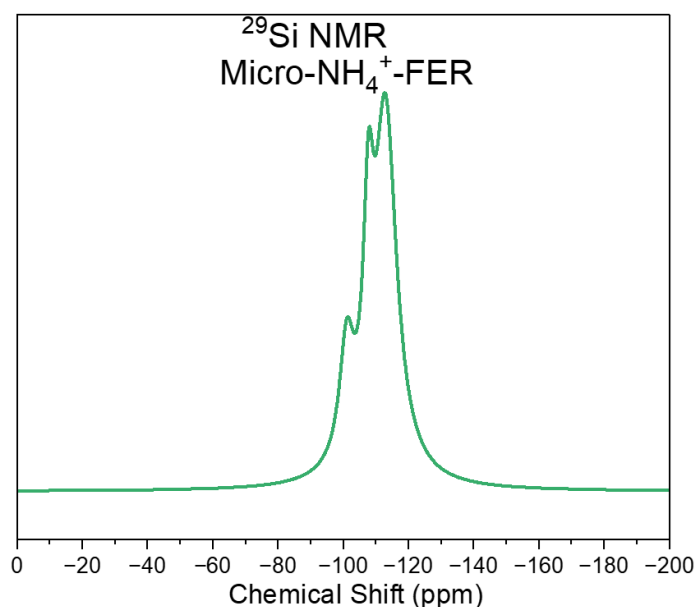


Figure 4.40.  $^{29}Si$ -MAS-NMR Spectra of Micro- $NH_4^+$ -FER

Figure 4.40 and Figure 4.41 show the  $^{29}Si$ -NMR plots of the Micro and Meso-Steam-FER structures. For micro- $NH_4^+$ -FER, 3 peaks are located at approximately -102 ppm, -108 ppm and -112 ppm. These are associated with Si(2Si), Si(3Si) and Si(4Si) respectively. Similar peaks appear at -103, -109 and -111 ppm for the Meso-Steam- $NH_4^+$ -FER in Figure 4.41.

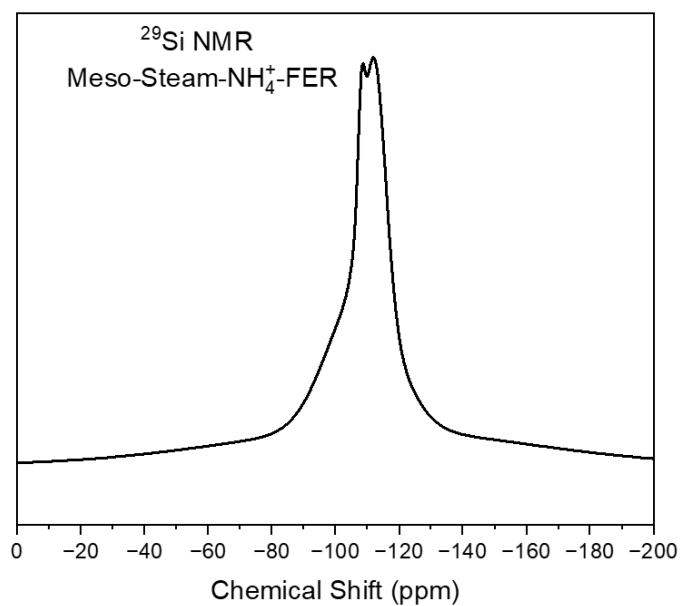


Figure 4.41.  $^{29}\text{Si}$ -MAS-NMR Spectra of Meso-Steam- $\text{NH}_4^+$ -FER

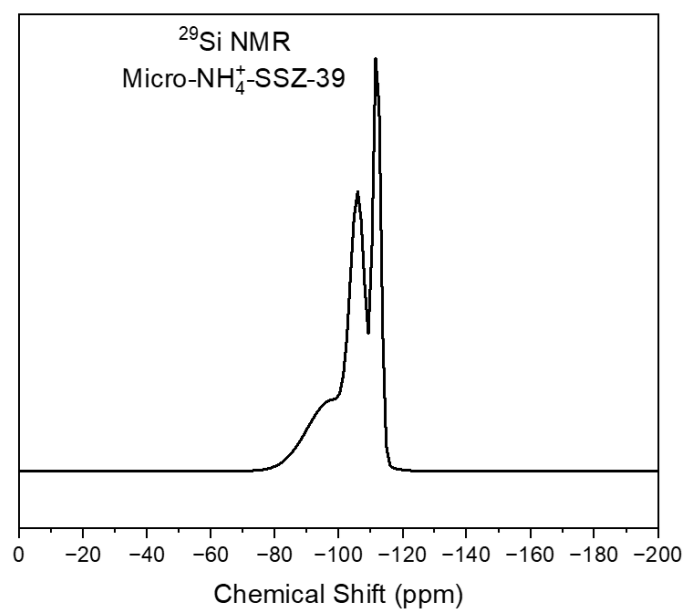


Figure 4.42.  $^{29}\text{Si}$ -MAS-NMR Spectra of Micro- $\text{NH}_4^+$ -SSZ-39

Figure 4.42 shows the  $^{29}\text{Si}$  MAS NMR of the Micro- $\text{NH}_4^+$ -SSZ-39 sample showing two signals at -112, -106 ppm associated with Si(4Si) and Si(3Si) respectively.

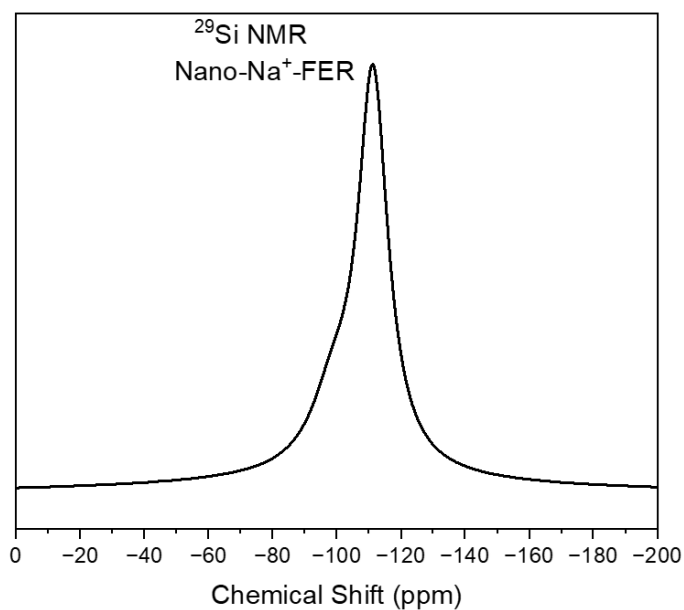


Figure 4.43.  $^{29}\text{Si}$ -MAS-NMR Spectra of Nano- $\text{Na}^+$ -FER

Figure 4.43 show the  $^{29}\text{Si}$ -NMR plot of the Nano- $\text{Na}^+$ -FER, 3 peaks are located at approximately -103, -112 and -115 ppm. These are associated with Si(2Si), Si(3Si) and Si(4Si) respectively.

#### 4.1.8 Raman Spectroscopy Results

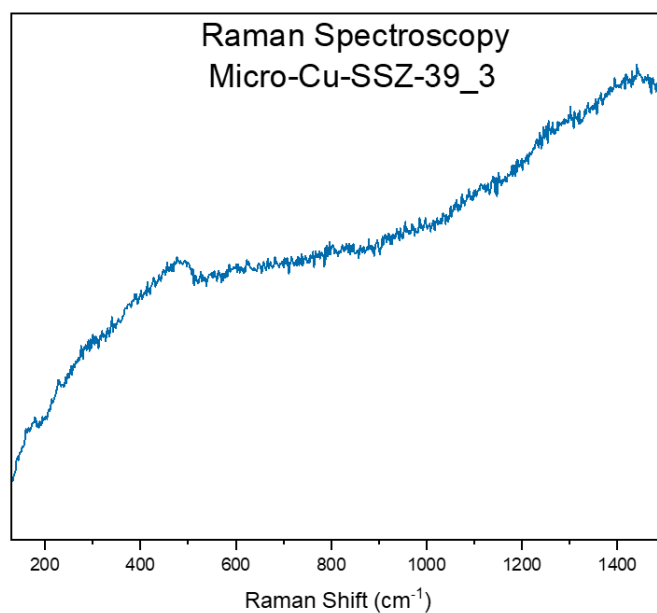


Figure 4.44. Raman Spectra of Micro-Cu-SSZ-39\_3R

The Raman spectra of Cu-Micro-FER\_3R and Cu-Micro-SSZ-39\_3R activated under N<sub>2</sub>O flow were obtained with a 532 nm laser source. Unfortunately, since the laser with a lower wavelength was not available at METU Central Laboratory, the 532 nm laser caused a large fluorescence scattering in the sample, which resulted in an uneven spectrum. The spectrum of Cu-Micro-SSZ-39\_3R obtained at low laser energies is given in Figure 4.44. In the high-noise spectrum obtained, T-O-T vibrations at 400-500 cm<sup>-1</sup> and Cu-O vibration of the mono-( $\mu$ -oxo) dicopper(II) active site at 610-620 cm<sup>-1</sup> can be noticed as stated in Section 2.1.1.

#### 4.1.9 In-Situ DR UV–Vis

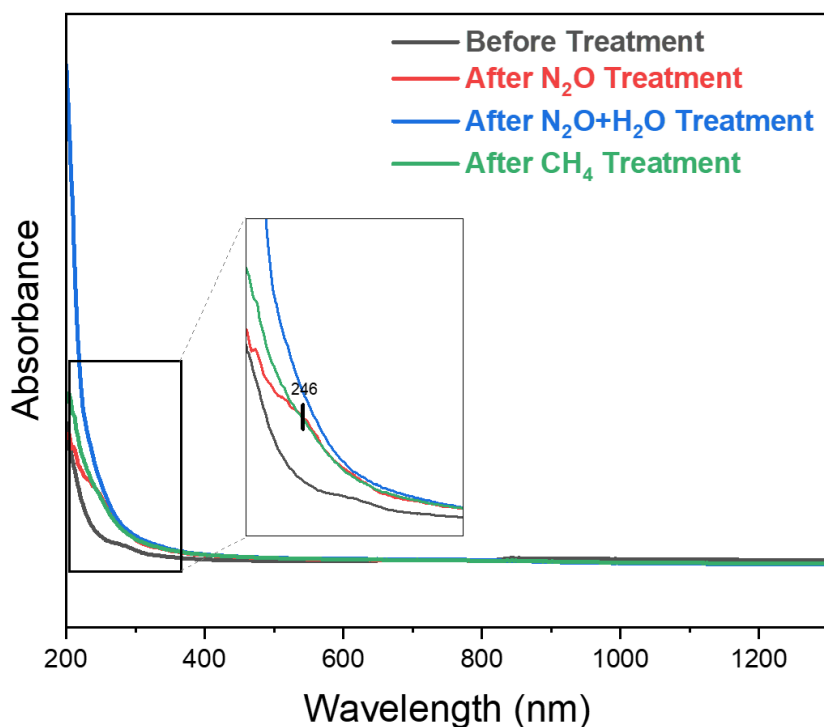


Figure 4.45. In-situ DR UV–Vis spectra of Micro-Cu-FER\_1

UV–Vis spectra are given in Figure 4.45, Figure 4.46, Figure 4.47, Figure 4.48, Figure 4.49, and Figure 4.50. In all samples, there is a peak around 250 nm ( $41\,000\text{ cm}^{-1}$ ) which does not appear in untreated state but appears with N<sub>2</sub>O treatment. This peak continued to be observed in Nano-Cu-FER\_2, and Micro-Cu-FER\_2 after H<sub>2</sub>O+N<sub>2</sub>O treatment, while it disappeared in Micro-Cu-FER\_1, Micro-Cu-FER\_3, Nano-Cu-FER\_1 samples after H<sub>2</sub>O+N<sub>2</sub>O treatment. In the Micro-Cu-SSZ-39\_3 sample, the intensity of the peak decreased after H<sub>2</sub>O+N<sub>2</sub>O treatment. According to the literature, the high wavenumber peak around  $41\,000\text{ cm}^{-1}$  is assigned to “Cu monomers” [128]. In addition to the studies mentioned in the literature section, there are many studies on this subject. It is thought that there are two basic structures of this monomer structure, one is Cu bound in a unit cell (silanol defect-Cu) and the other is CuOH. Experimental and theoretical studies have shown that both active sites are located around  $41\,000\text{ cm}^{-1}$ , but the silanol defect-Cu shows an extra peak

at  $11\,500\text{ cm}^{-1}$  (around  $870\text{ nm}$ ). In addition, more extensive studies in the literature have shown that the peak around  $41\,000\text{ cm}^{-1}$  belongs to the adjacent 2  $(\text{CuOH})^{2+}$  active site [128], [129], [130].

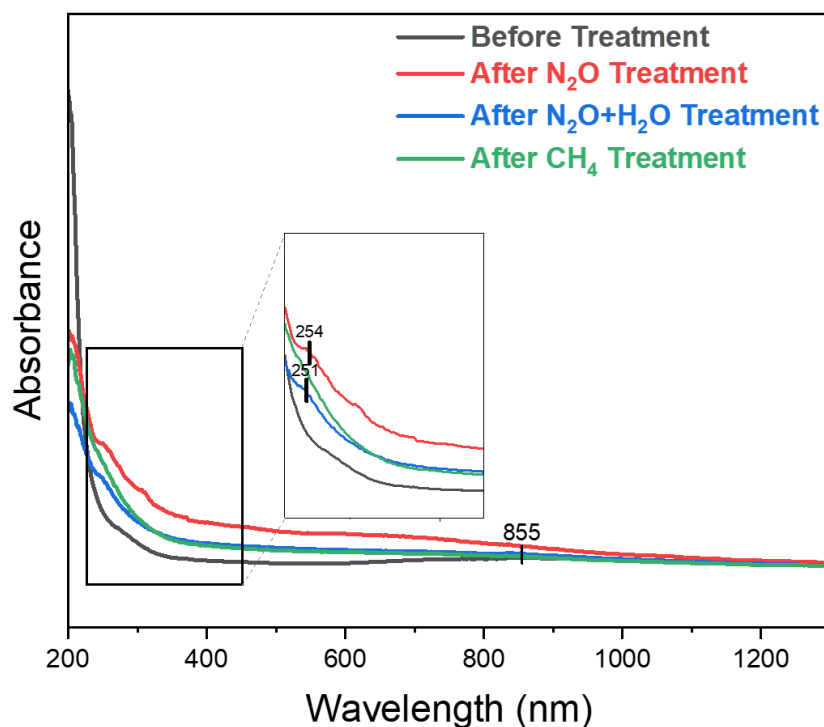


Figure 4.46. In-situ DR UV-Vis spectra of Micro-Cu-FER<sub>2</sub>

In line with this information, it can be considered that our catalysts showing a peak around  $250\text{ nm}$  ( $41\,000\text{ cm}^{-1}$ ) have a monomer Cu active site and those that do not show a peak around  $870\text{ nm}$  ( $11\,500\text{ cm}^{-1}$ ) have only CuOH active site. These are also likely to be composed of 2 adjacent structures. Micro-Cu-FER<sub>1</sub> is an example of this case. Nano-Cu-FER<sub>1</sub> shows peaks around  $870\text{ nm}$ , indicating the coexistence of CuOH and silanol defect-Cu structures. This is normal as multiple active sites can be present in a catalyst at the same time, and hydroxylated copper dimer structures around  $750\text{ nm}$  are also present in the high copper content samples Micro-Cu-FER<sub>3</sub>, Nano-Cu-FER<sub>2</sub> and Micro-Cu-SSZ-39<sub>3</sub>. Peaks around  $800\text{ nm}$  are also assigned to d-d transitions of  $\text{Cu}^{2+}$  cations and it is generally observed that as the Cu/Al ratio increases, the related peak intensities also increase.

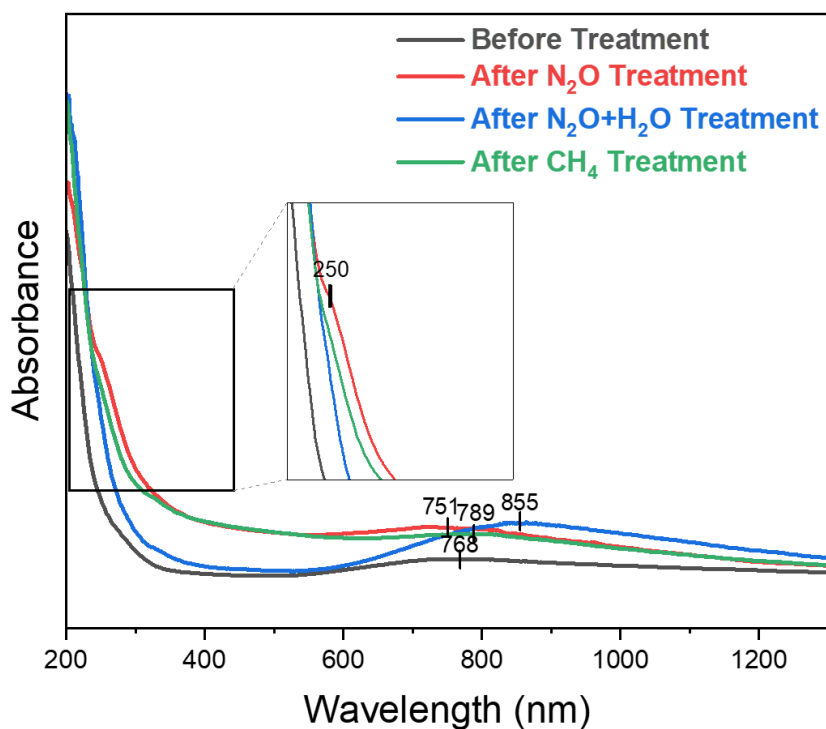


Figure 4.47. In-situ DR UV-Vis spectra of Micro-Cu-FER\_3

In studies in the literature, it is said that CuO particles are also seen around  $40\,000\text{ cm}^{-1}$  (250 nm). If there are peaks around 245-250 nm in the before treatment state of the samples, this indicates CuO formation [131], [132]. This is seen in three of the Micro-FER zeolites, but looking at the intensity values, it cannot be said that the Micro-FER\_3 sample has the highest value. This is not expected because CuO formation is expected in high-temperature exchanges or in samples with higher copper molarity (such as Micro-Cu-FER\_3), while peak intensity values are more distinctive in Nano-Cu-FER samples. However, unlike Micro-FER, peaks were observed more clearly in Nano-Cu-FER samples. Similar peak before treatment was observed in the Micro-SSZ-39\_3 sample (see Figure 4.50).

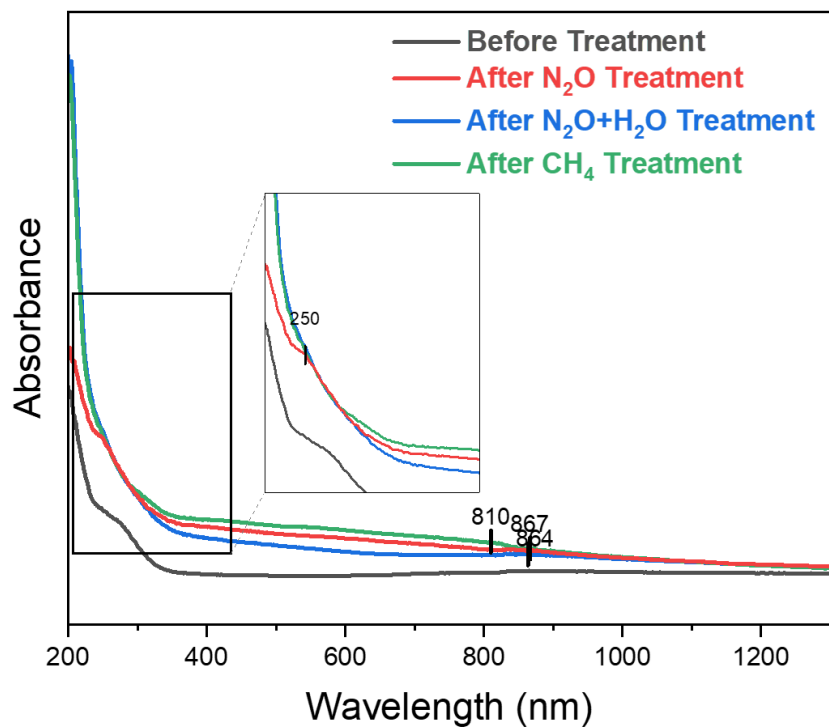


Figure 4.48. In-situ DR UV-Vis spectra of Nano-Cu-FER\_1

While we expected a definite disappearance of the peaks after CH<sub>4</sub> treatment, in Micro-Cu-SSZ-39\_3 (see Figure 4.50) they did not decrease and even increased, while in Nano-Cu-FER\_2 (see Figure 4.49) the intensity decreased but did not disappear.

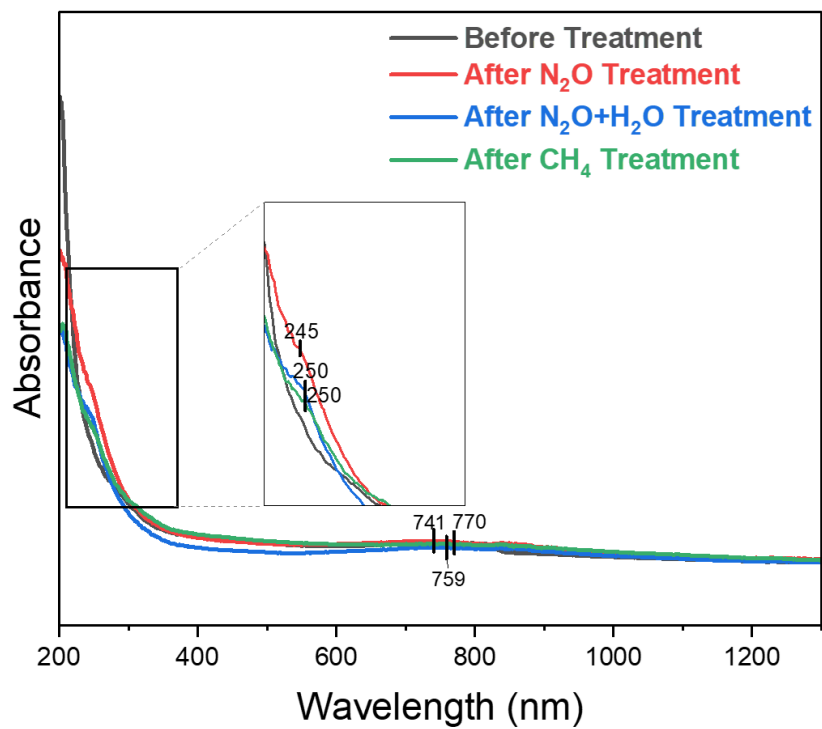


Figure 4.49. In-situ DR UV-Vis spectra of Nano-Cu-FER<sub>2</sub>

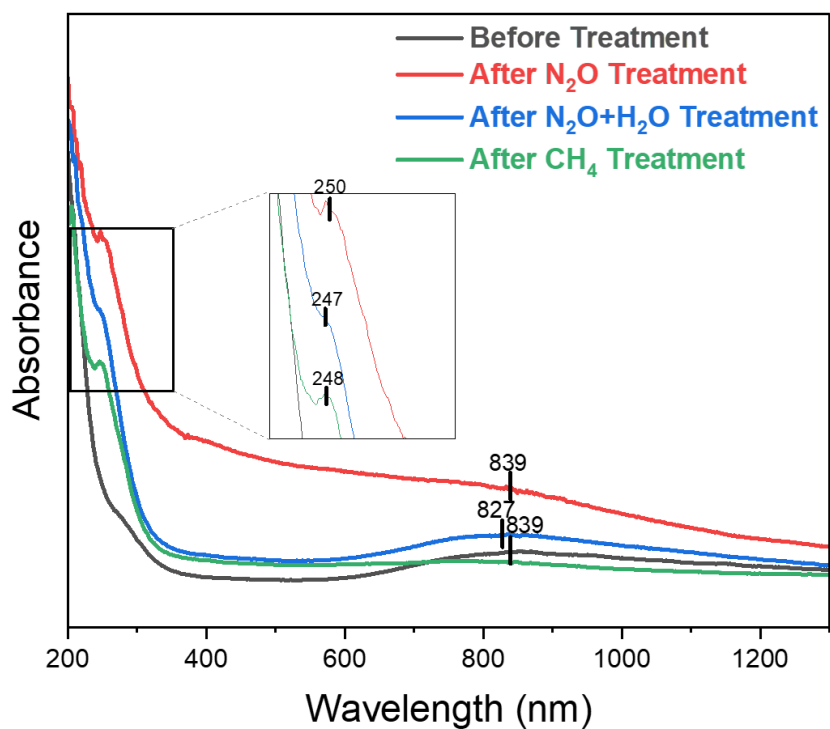


Figure 4.50. In-situ DR UV-Vis spectra of Micro-Cu-SSZ-39<sub>3</sub>

## 4.2 Activity Test Results

The reaction results are divided into two parts: reactant and helium heating.

### 4.2.1 Activity Test Results with Reactant Heating Method

In this section, in terms of optimization, Cu/Al ratio in two different framework structures (FER and AEI), Na<sup>+</sup> ion effect, N<sub>2</sub>O effect, calcination effect after Cu(II)-exchange, and reusability effect were studied.

#### 4.2.1.1 Effect of Copper on Micro-FER

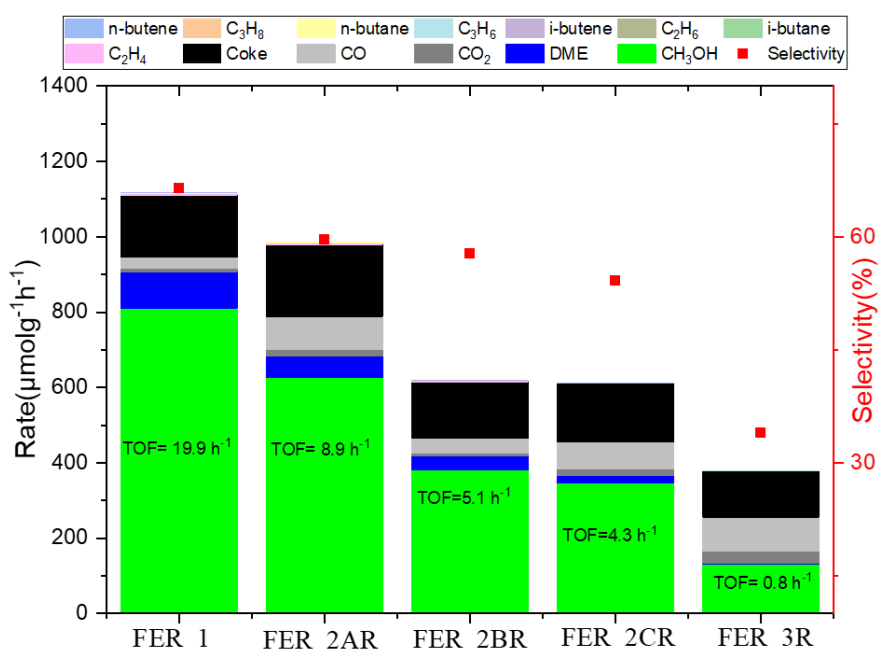


Figure 4.51. Activity test results of Micro-Cu-FER samples, 325 °C, 40% methane, 15% N<sub>2</sub>O, 3% H<sub>2</sub>O and 42% He

The activity tests of 5 prepared catalysts were carried out under the conditions mentioned in the reaction procedure (325°C, 40% methane, 15% N<sub>2</sub>O, 3% H<sub>2</sub>O and 42% He). The test results of Micro-Cu-FER catalysts containing different amounts of copper are given in Figure 4.51. It was observed that methanol production

decreased as the amount of copper increased in the structure. The catalyst with the lowest amount of copper, Micro-Cu-FER\_1 (Cu concentration of 0.041 mmol Cu g cat<sup>-1</sup>) gave the highest methanol production (about 810  $\mu\text{mol g}^{-1}\text{h}^{-1}$ ). In the studies conducted by Pappas et al., the opposite is observed in copper-containing FER zeolites in the three-step stoichiometric conversion of methane to methanol. In addition, according to Pappas et al., methanol production was not observed when the Cu/Al ratio was below 0.1 [121]. In the three-step study, the highest methanol production was 95  $\mu\text{mol g}^{-1}$  for Cu/Al=0.2, Si/Al=11 and methanol selectivity was 85%. The methanol selectivity of the Micro-Cu-FER\_1 sample is about 65% and the TOF value is 19.9 molCH<sub>3</sub>OH molCu<sup>-1</sup>h<sup>-1</sup>. As the amount of copper in zeolite increased, methanol production decreased and TOF values also decreased as seen in Figure 4.51. At the same time, MeOH selectivity showed a similar trend. Dinh et al. in their study on the catalytic conversion of methane to methanol by continuous flow found conclusions in line with the present results. According to the study, copper nanoparticle formation is observed when the copper atoms per lattice structure is above 0.3 (since the study was carried out with CHA zeolite, the corresponding Cu/Al ratio is above 0.1) and this resulted in direct conversion of methane to carbon dioxide [114]. This is also shown in Figure 4.51. As the Cu/Al ratio increased, the amount of CO<sub>2</sub> produced also increased. In order to see the difference clearly, CO<sub>2</sub> production rate of 8  $\mu\text{mol g}^{-1}\text{h}^{-1}$  was observed on Micro-Cu-FER\_1, while it was 31  $\mu\text{mol g}^{-1}\text{h}^{-1}$  on Micro-Cu-FER\_3 (Cu/Al=0.09, Cu concentration: 0.155 mmol Cu g cat<sup>-1</sup>). In addition, when TEM images are analyzed, CuO formation was observed in samples with high copper content and this is consistent with our results.

However, there are some discussions related with CuO formation in the literature. While some studies indicate that CuO does not activate the methane molecule or is not selective [114], [133].

#### 4.2.1.2 Effect of Na<sup>+</sup> ions

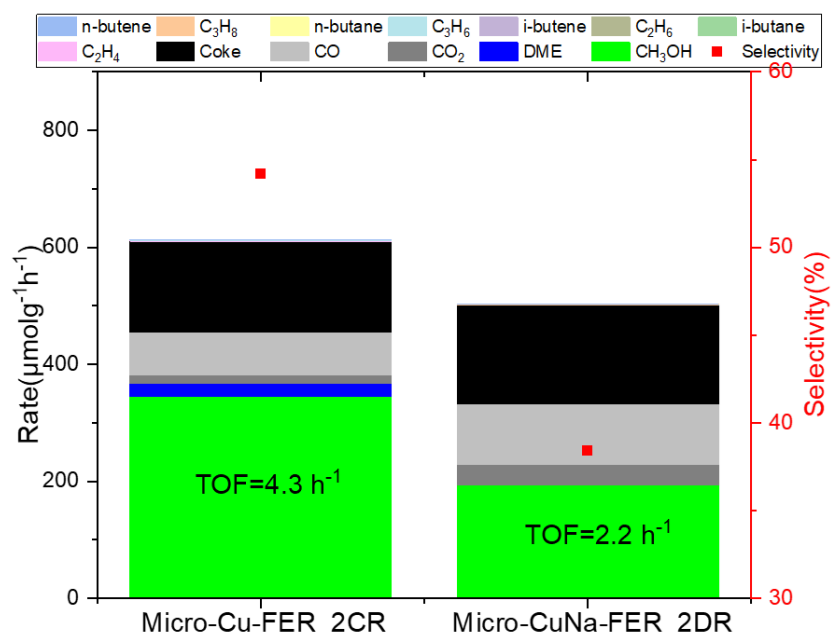


Figure 4.52. Activity test results of Micro-Cu-FER samples with and without Na<sup>+</sup> ions, 325 °C, 40% methane, 15% N<sub>2</sub>O, 3% H<sub>2</sub>O and 42% He

Na<sup>+</sup> containing sample Micro-CuNa-FER\_2DR produced less methanol than the Micro-Cu-FER\_2CR as can be seen in Figure 4.52. Their Cu/Al ratios and Si/Al ratios are similar. In the literature, this was again explained by Dinh et al. that zeolitic protons and H<sub>2</sub>O are critical for the desorption of CH<sub>3</sub>OH, although they have a kinetic effect. Cu dimers are assumed to be formed under reaction conditions by hydrated ionic diffusion along a protonic pathway in the presence of H<sup>+</sup>-zeolite content [114].

### 4.2.1.3 Effect of N<sub>2</sub>O

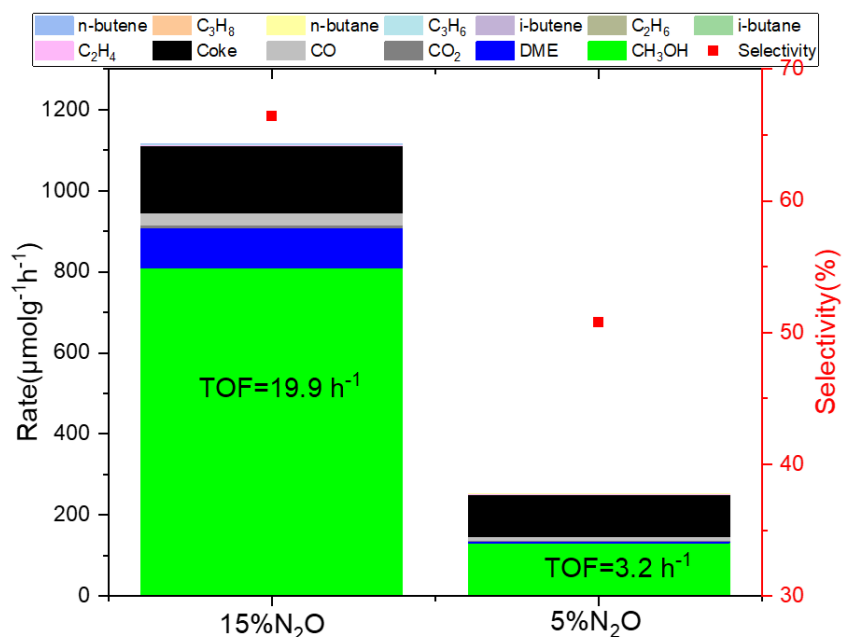


Figure 4.53. Activity test results of Micro-Cu-FER\_1 sample, 325 °C, 40% methane, 5 or 15% N<sub>2</sub>O, 3% H<sub>2</sub>O and balance He

It is known that the increased amount of nitrous oxide in feed enhances the creation of active sites but also speeds up the secondary reactions [91]. The optimization study was carried out with a lower value (5% N<sub>2</sub>O) than the 15% N<sub>2</sub>O value in the previous study [112]. The main reason for this is that N<sub>2</sub>O production consists of more than one step, is expensive and is not widely used [134]. As can be seen in Figure 4.53, methanol production decreased from 800 to 180 μmol g<sup>-1</sup>h<sup>-1</sup> with the decrease in N<sub>2</sub>O value. Since further increase was not preferred for economic reasons, the study was continued with 15% N<sub>2</sub>O value.

#### 4.2.1.4 Effect of Calcination

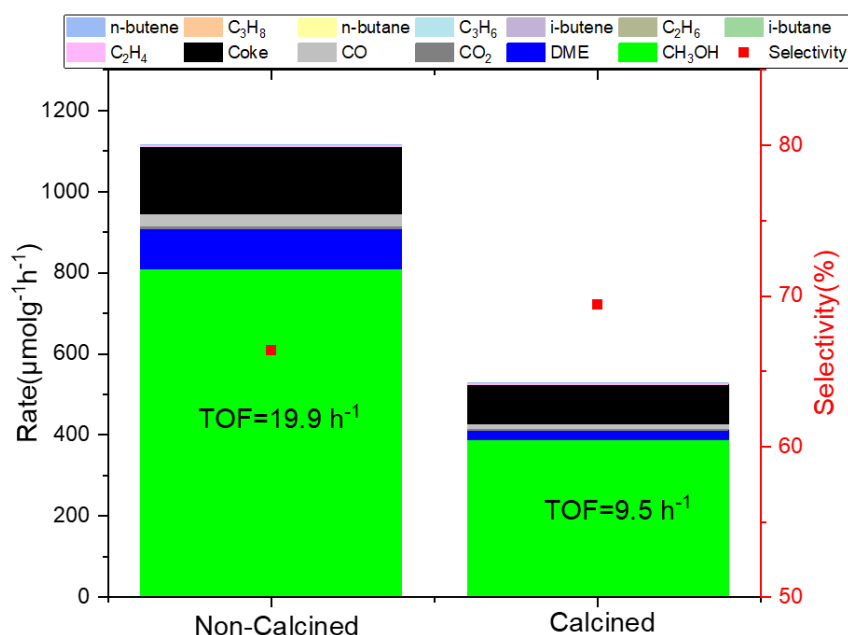


Figure 4.54. Activity test results of Micro-Cu-FER\_1 sample with and without calcination, 325 °C, 40% methane, 15% N<sub>2</sub>O, 3% H<sub>2</sub>O and 42% He

Samples were only washed and filtered with DI H<sub>2</sub>O after Cu(II)-exchange as described in the Experimental Methodology and no heat treatment/calcination was applied. The main reason for this is the effect on methanol activity as can be seen in Figure 4.54. The methanol production decreased from 800 to 400 μmol g<sup>-1</sup>h<sup>-1</sup> following calcination, which might be due to formation of inactive CuO<sub>x</sub> sites. The methanol selectivity value is only slightly higher in the calcined sample (around 69%) than in the non-calcined sample (around 66%). However, for the combined carbon-based CH<sub>3</sub>OH+DME selectivity value is 82% on non-calcined sample whereas the value on calcined one is 76%. Extra-framework Al sites are known to increase Lewis acid sites and decrease Brønsted acid sites. The higher selectivity of CH<sub>3</sub>OH+DME can be observed when the BAS is higher. The higher BAS in the non-calcined sample can be explained by the absence or lower intensity of extra-framework sites compared to the calcined version because the calcined sample reaches around 550 °C and extra-framework Al sites can be observed. For these

reasons, the samples were thoroughly filtered and washed after Cu(II)-exchange and calcination was not applied.

#### 4.2.1.5 Effect of Mesoporosity

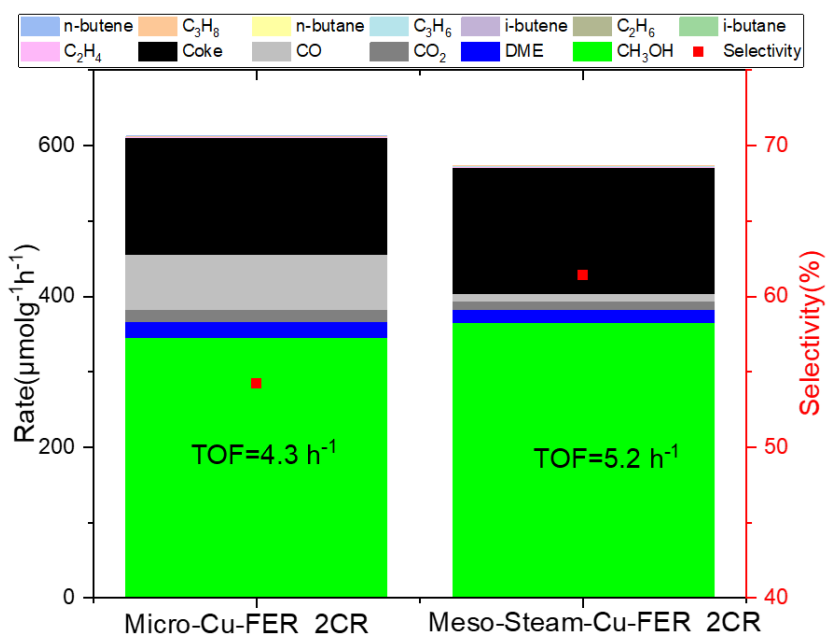


Figure 4.55. Activity test results of Micro-Cu-FER and Meso-Steam-Cu-FER samples, 325 °C, 40% methane, 15% N<sub>2</sub>O, 3% H<sub>2</sub>O and 42% He

Figure 4.55 shows the activity test result of Meso-Steam-Cu-FER\_2CR and Micro-Cu-FER\_2CR with similar Cu/Al ratio. Looking at the TOF values and methanol production, it was observed that slightly mesoporous sample gave better results. Although the Meso-Steam-Cu-FER\_2CR sample is higher in terms of coke production (167 vs 155 μmol g<sup>-1</sup>h<sup>-1</sup>), the opposite is the case for CO (10 vs 73 μmol g<sup>-1</sup>h<sup>-1</sup>) and CO<sub>2</sub> (10 vs 15 μmol g<sup>-1</sup>h<sup>-1</sup>). Meso-Steam-Cu-FER\_2CR also gave better results in terms of methanol selectivity (61% vs 54%), but it is not possible to make a clear interpretation under these conditions. The main reason is the presence of extra-framework Al sites in the mesoporous sample when looking at the <sup>27</sup>Al-MAS-NMR results. This changes the Si/Al ratio in the structure directly affecting the

results. There is also an ongoing debate on the positive effect of the extra-framework Al sites on the activity [45], [106].

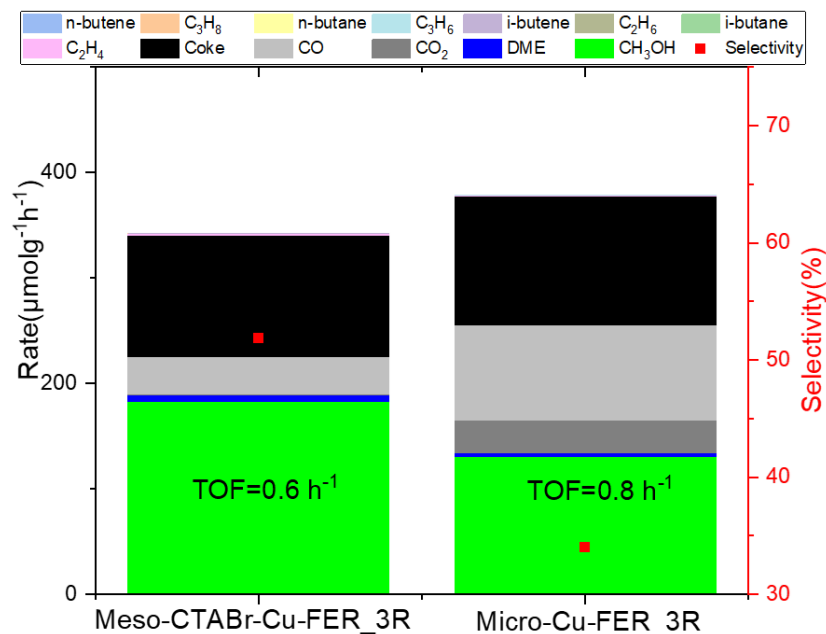


Figure 4.56. Activity test results of Micro-Cu-FER and Meso-CTABr-Cu-FER samples, 325 °C, 40% methane, 15% N<sub>2</sub>O, 3% H<sub>2</sub>O and 42% He

The other sample prepared to form mesoporous FER, Meso-CTABr-Cu-FER\_3R, although higher in Cu/Al (See Table 4.1), was tested under similar reaction conditions as Micro-Cu-FER\_3R as can be seen from Figure 4.56. Methanol production (182 vs 130 μmol g<sup>-1</sup>h<sup>-1</sup>) and selectivity gave better results. Less CO (36 vs 90 μmol g<sup>-1</sup>h<sup>-1</sup>), CO<sub>2</sub> (0.3 vs 31 μmol g<sup>-1</sup>h<sup>-1</sup>) and coke (115 vs 122 μmol g<sup>-1</sup>h<sup>-1</sup>) formation was also observed. However, the purity of the mesoporous structure is questionable as can be seen from the XRD and N<sub>2</sub> physisorption results. In addition, the different Si/Al ratios make the comparison difficult.

#### 4.2.1.6 Effect of Copper on SSZ-39

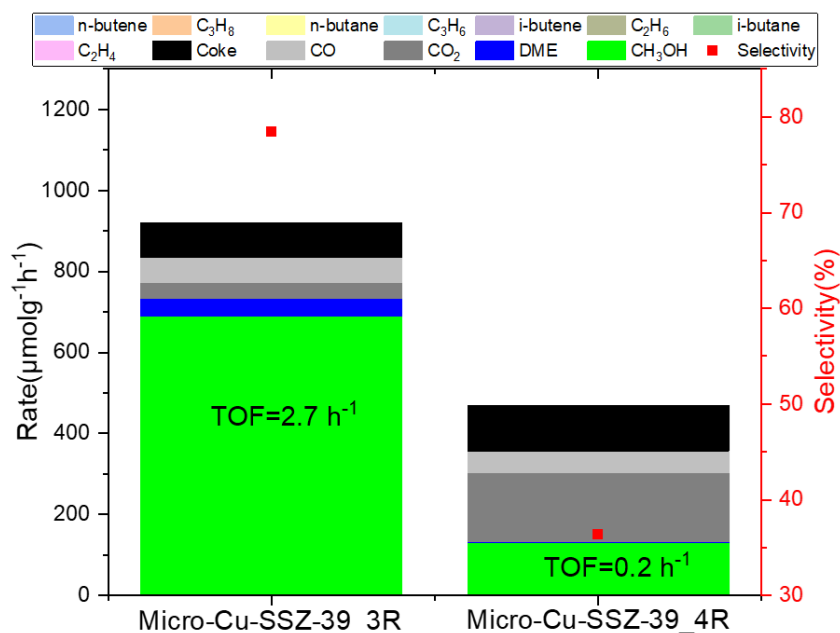


Figure 4.57. Activity test results of Micro-Cu-SSZ-39 samples, 325 °C, 40% methane, 15% N<sub>2</sub>O, 3% H<sub>2</sub>O and 42% He

SSZ-39 (AEI) samples, which have a framework structure different from the FER structure, were also tested under similar conditions at different Cu/Al ratios can be seen from Figure 4.57. A situation similar to Micro-Cu-FER was observed in this sample. As the copper content increased, the selectivity decreased (from 78% to 36%) and methanol production decreased (from 689 to 130 μmol g<sup>-1</sup>h<sup>-1</sup>). This can be explained by the fact that Cu/Al > 0.1 as mentioned in the Micro-Cu-FER sample and the decrease in H<sup>+</sup> sites, because in the Micro-Cu-SSZ-39\_4R sample CO<sub>2</sub> production increased (from 39 to 170 μmol g<sup>-1</sup>h<sup>-1</sup>) considerably and DME formation (1 μmol g<sup>-1</sup>h<sup>-1</sup>) was almost not observed.

#### 4.2.1.7 Effect of Reusability

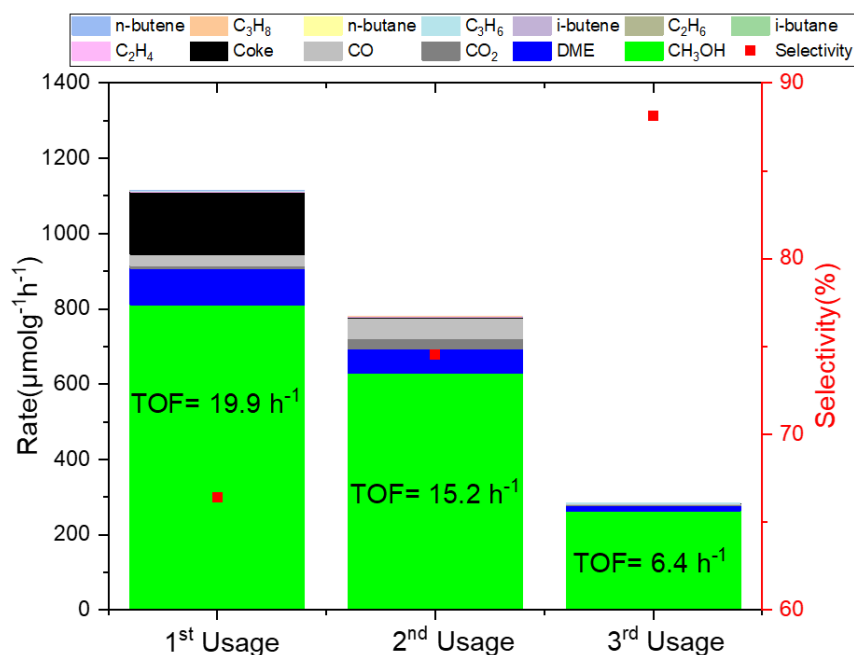


Figure 4.58. Activity test results of Micro-Cu-FER\_1 after regeneration steps, 325 °C, 40% methane, 15% N<sub>2</sub>O, 3% H<sub>2</sub>O and 42% He

Reusability of catalysts is as important as their long-term stability. In this context, Micro-Cu-FER\_1 experienced a serious loss in methanol activity (809, 630 and 262 μmol g<sup>-1</sup>h<sup>-1</sup> respectively) in repeated use as given in Figure 4.58. The sample was regenerated at 550 °C under 75 sccm air flow for 2 hours after each use. However, coke formation also decreased dramatically (165, 2.9 and 1.6 μmol g<sup>-1</sup>h<sup>-1</sup> respectively). Different reactions take place at low temperatures until the reaction temperature reaches 325 °C with reactant heating. Due to this situation, changes in structure may have been observed. Although this situation is explained in the literature through leaching or sintering [135].

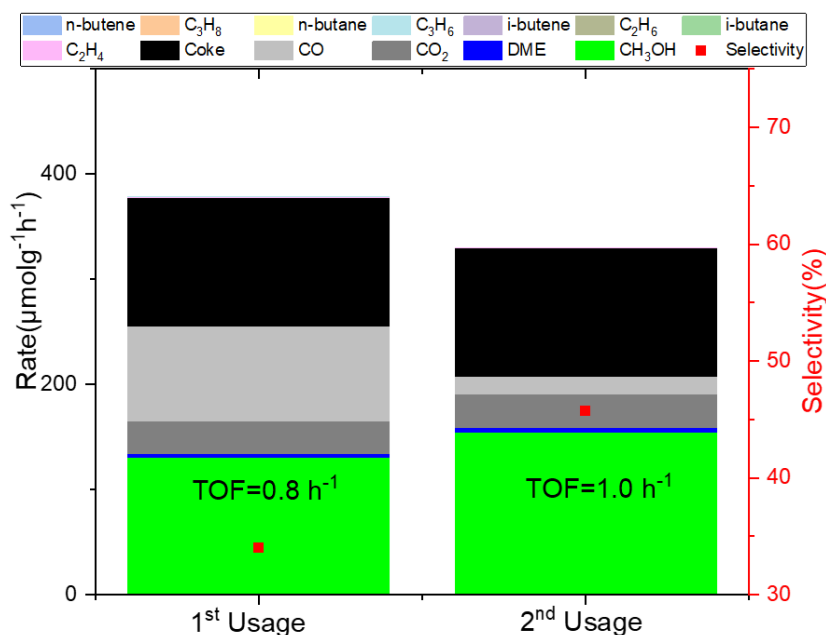


Figure 4.59. Activity test results of Micro-Cu-FER\_3R after regeneration steps, 325 °C, 40% methane, 15% N<sub>2</sub>O, 3% H<sub>2</sub>O and 42% He

The reusability effect was also tested under similar conditions for the higher copper content. However, unlike Micro-Cu-FER\_1, Micro-Cu-FER\_3R did not show any reduction in methanol production. In fact, while methanol production increased (from 130 to 154  $\mu\text{mol g}^{-1}\text{h}^{-1}$ ) with reuse, no change was observed in coke production (122  $\mu\text{mol g}^{-1}\text{h}^{-1}$  for both case).

#### 4.2.2 Activity Test Results with Helium Heating Method

In this section, samples brought to reaction temperature with helium were tested. Comparison of reactant and helium heating method, reusability, catalytic activity results of copper content on Micro-FER, Micro-SSZ-39, Micro-SSZ-13 and Nano-FER and in this context the comparison between framework structures and zeolite particle size and finally the effect of different H<sub>2</sub>O amounts were investigated.

#### 4.2.2.1 Effect of Heating Method

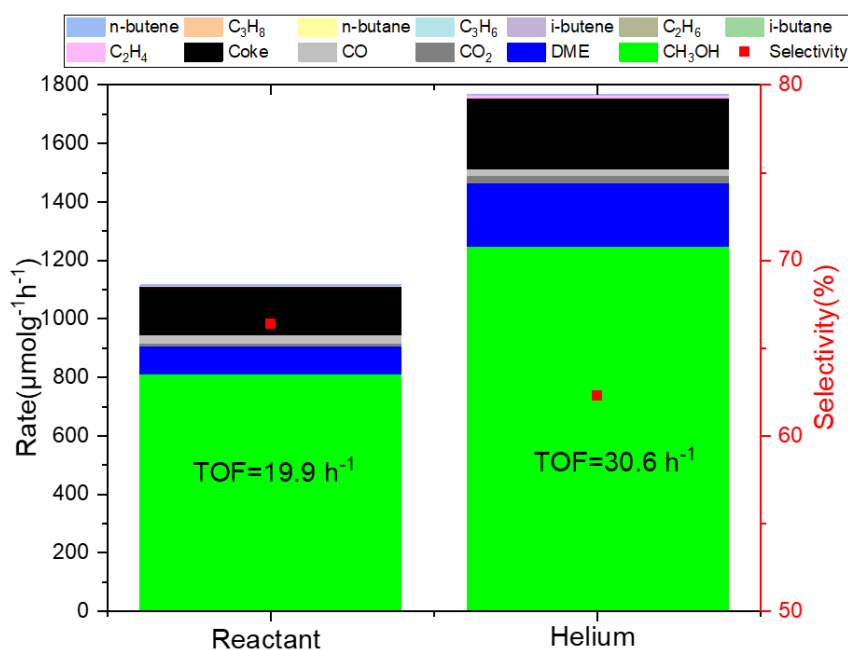


Figure 4.60. Activity test results of Micro-Cu-FER\_1 with reactant or helium heating, 325 °C, 40% methane, 15% N<sub>2</sub>O, 3% H<sub>2</sub>O and 42% He

Micro-Cu-FER\_1 reactant and helium heating results are shown in Figure 4.60. Methanol production is 1249  $\mu\text{mol g}^{-1}\text{h}^{-1}$  in helium heating case and 809  $\mu\text{mol g}^{-1}\text{h}^{-1}$  in reactant heating case. DME production is 216  $\mu\text{mol g}^{-1}\text{h}^{-1}$  in helium heating and 96  $\mu\text{mol g}^{-1}\text{h}^{-1}$  in the other. This can be explained by the decrease in DME production due to the closure of the acidic sites in the structure during reactant heating by possible coke formation during heating. The difference between the TOF values is also quite large (30.6  $\text{h}^{-1}$  vs 19.9  $\text{h}^{-1}$ ). In terms of CH<sub>3</sub>OH selectivity reactant heating method is 66% whereas 63% for helium heating. However, CH<sub>3</sub>OH+DME carbon-based selectivity of helium heating method is 85% while reactant heating method has 82%. In reactions taking place at low temperatures in the reactant heating method, acid sites may be closed by coke formation or copper sites may be blocked in terms of activity. The Boudouard reaction also triggers the formation of carbon at temperatures up to 325 °C [136]. This may also have an effect on the closure of active sites and acid sites on these surfaces.

#### 4.2.2.2 Effect of Reusability

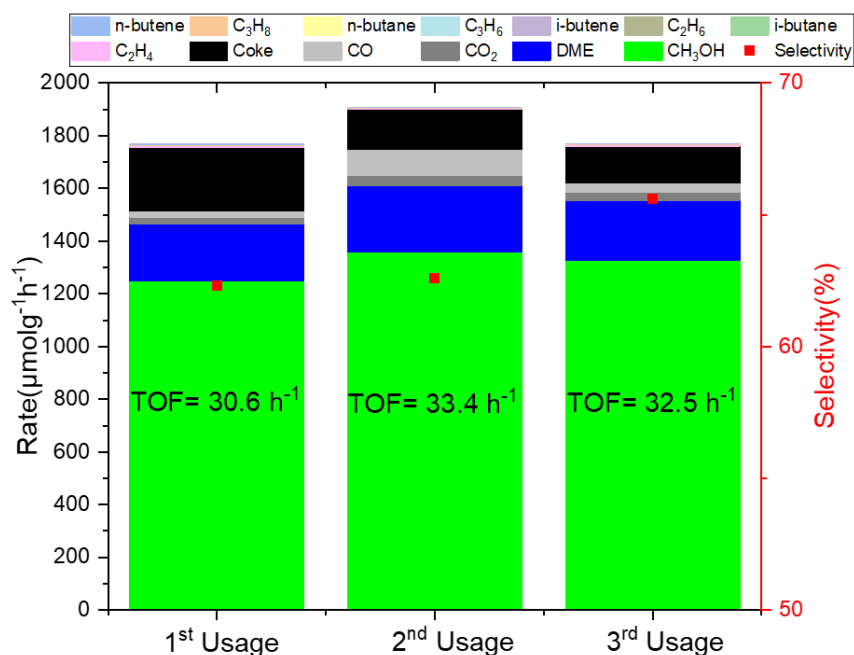


Figure 4.61. Activity test results of Micro-Cu-FER\_1 after regenerations, 325 °C, 40% methane, 15% N<sub>2</sub>O, 3% H<sub>2</sub>O and 42% He

Reusability tests after regeneration with reactant heating were also performed with helium heating for the Micro-Cu-FER\_1 and the results can be seen in Figure 4.61. In contrast to the reactant heating method, no decrease in methanol production was observed in reuse, in fact a slight increase (1249, 1360 and 1325 μmol g<sup>-1</sup>h<sup>-1</sup> respectively) was observed. The selectivity values are also very close (62%, 63% and 65%). Only a decrease in coke formation was observed after the first use, but no significant decrease was observed in the 2<sup>nd</sup> and 3<sup>rd</sup> use (241, 150 and 141 μmol g<sup>-1</sup>h<sup>-1</sup>).

The helium heating method was preferred and the study was continued in this way since methanol production increased and there was no problem in reuse and selectivity values did not change dramatically.

### 4.2.2.3 Effect of Copper on Micro-FER

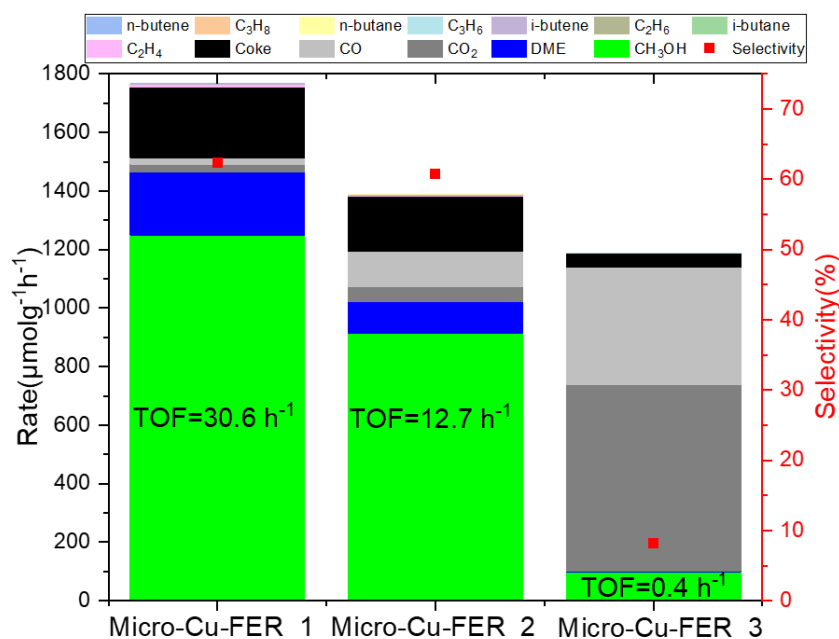


Figure 4.62. Activity test results of Micro-Cu-FER with different Cu/Al ratios, 325 °C, 40% methane, 15% N<sub>2</sub>O, 3% H<sub>2</sub>O and 42% He

The effect of copper content on Micro-FER was tested for 3 different Cu/Al ratios and the results are shown in Figure 4.62. Methanol production decreased with increasing copper content (1249, 914, and 98  $\mu\text{mol g}^{-1}\text{h}^{-1}$  respectively), similar to the results for reactant heating. A similar situation was also observed for DME production (216, 108 and 4  $\mu\text{mol g}^{-1}\text{h}^{-1}$  respectively). CO<sub>2</sub> formation was 636  $\mu\text{mol g}^{-1}\text{h}^{-1}$  in Micro-Cu-FER\_3 and 26 and 52  $\mu\text{mol g}^{-1}\text{h}^{-1}$  in Micro-Cu-FER\_1 and Micro-Cu-FER\_2 respectively. This can be explained by the CuO formation in Micro-Cu-FER\_2. In addition, coke production is 241, 187 and 49  $\mu\text{mol g}^{-1}\text{h}^{-1}$ . Selectivity values of methanol are 62%, 60% and 8%. The production of C<sub>2</sub>, C<sub>3</sub> and C<sub>4</sub> is higher in the Micro-Cu-FER\_1 sample compared to the others and this is mainly due to the conversion of the excess amount of produced methanol produced to olefin on acidic sites of FER.

#### 4.2.2.4 Effect of Copper on SSZ-39

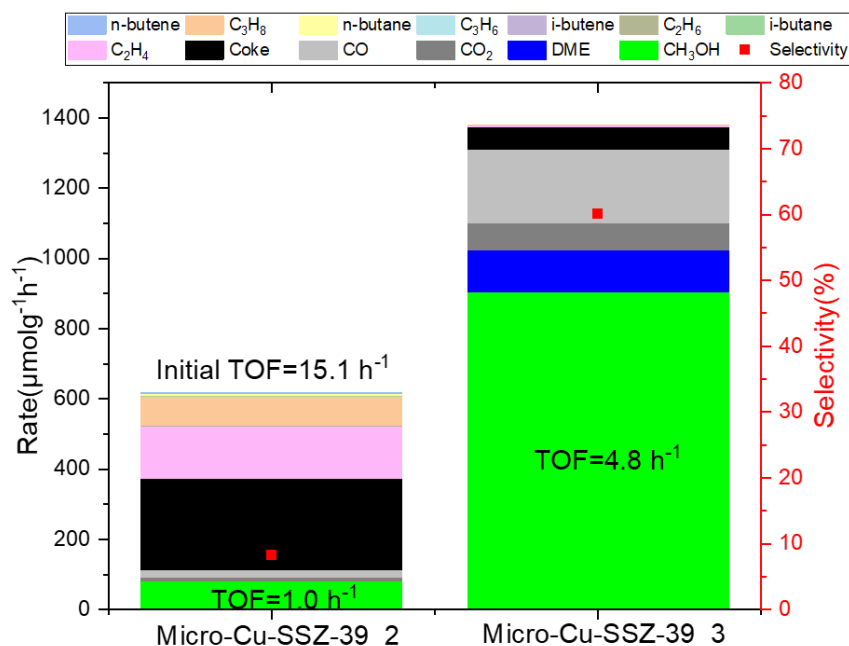


Figure 4.63. Activity test results of Micro-Cu-SSZ-39 with different Cu/Al ratios, 325 °C, 40% methane, 15% N<sub>2</sub>O, 3% H<sub>2</sub>O and 42% He

The Micro-Cu-SSZ-39 samples in this section have lower Cu/Al ratios compared to those in the reactant heating and the results are shown in Figure 4.63. Although methanol production seems to be lower at a low Cu/Al ratio, this is actually not the case. As shown in Figure 4.64, methanol production decreased (from values of 1300  $\mu\text{mol g}^{-1}\text{h}^{-1}$ ) during the reaction while C<sub>3</sub>H<sub>8</sub> and C<sub>2</sub>H<sub>4</sub> production (mixed alkane and olefin) dominates. Initial TOF of Micro-Cu-SSZ-39\_2 was 15.1 (in mol CH<sub>3</sub>OH/mol Cu\*h<sup>-1</sup>), which stabilized at 1.0 during the reaction. It is reported that the acidic characteristics (BAS) play a significant role in the catalytic ability of continuous catalytic DMTM because methanol is readily further transformed on the acid sites into light olefins [105], [137], [138].

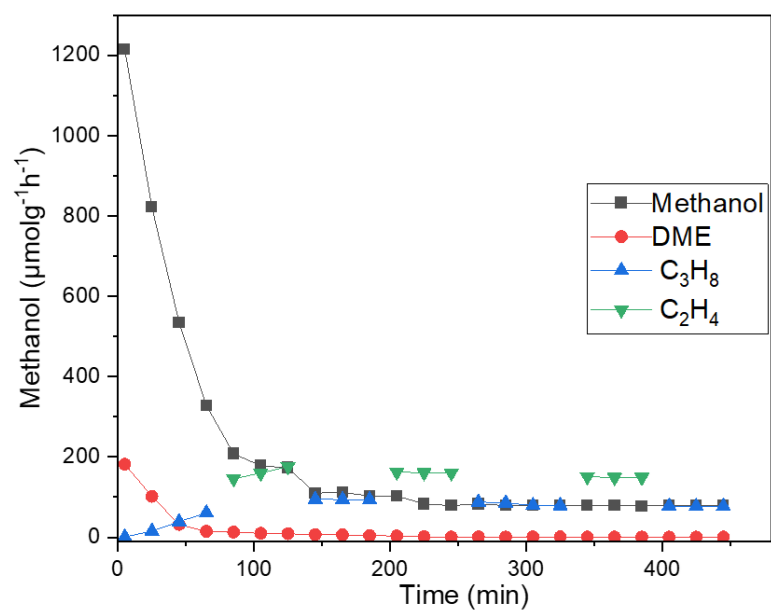


Figure 4.64. Activity test results of Micro-Cu-SSZ-39\_2 with respect to time

#### 4.2.2.5 Effect of Copper Content on SSZ-13

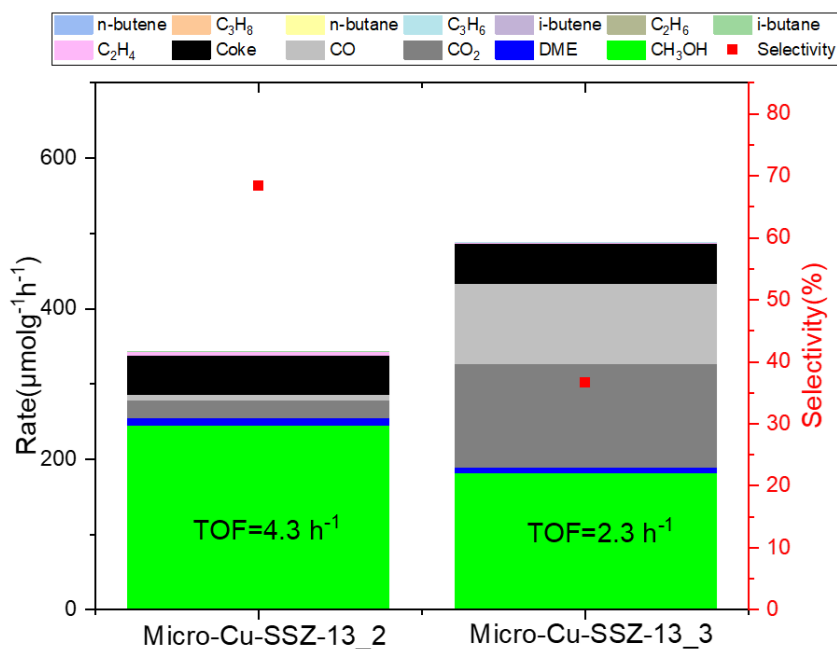


Figure 4.65. Activity test results of Micro-Cu-SSZ-13 with different Cu/Al ratios, 325 °C, 40% methane, 15%  $\text{N}_2\text{O}$ , 3%  $\text{H}_2\text{O}$  and 42% He

Samples of Micro-SSZ-13 at different Cu/Al ratios were tested and the results are shown in Figure 4.65. In these samples, production of methanol decreased (from 245 to 182  $\mu\text{mol g}^{-1} \text{h}^{-1}$ ) with increasing copper content, but not as dramatically as in FER and SSZ-39. An increase in CO (from 8 to 106  $\mu\text{mol g}^{-1} \text{h}^{-1}$ ) and  $\text{CO}_2$  (from 24 to 138  $\mu\text{mol g}^{-1} \text{h}^{-1}$ ) production was observed with increasing copper content, whereas no change was observed in coke (53 vs 54  $\mu\text{mol g}^{-1} \text{h}^{-1}$ ).

When the zeolite framework structures were examined at similar Cu/Al ratios, the most stable and active structure in terms of methanol production was FER zeolite. In this context, more active results were tried to be obtained by synthesizing the nano-particle size of FER zeolite.

#### 4.2.2.6 Effect of Copper on Nano-FER

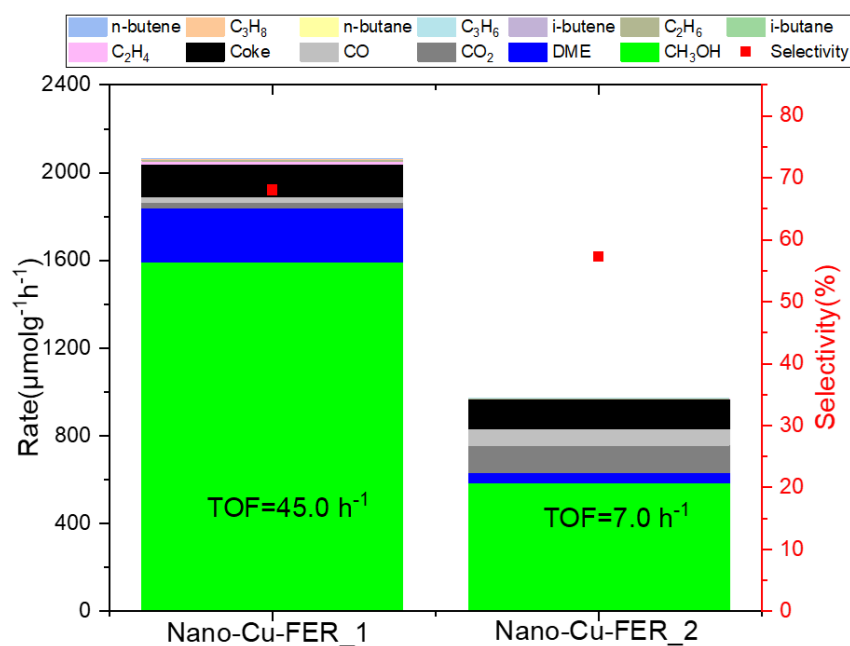


Figure 4.66. Activity test results of Nano-Cu-FER with different Cu/Al ratios, 325 °C, 40% methane, 15% N<sub>2</sub>O, 3% H<sub>2</sub>O and 42% He

Similar to the situation in Micro-Cu-FER and other samples, a similar trend was observed in Nano-Cu-FER with increasing copper content and the results are given in Figure 4.66. Nano-Cu-FER\_1 produced 1594  $\mu\text{mol g}^{-1}\text{h}^{-1}$  methanol while Nano-Cu-FER\_2 produced 586  $\mu\text{mol g}^{-1}\text{h}^{-1}$ . Selectivity values also decreased from 68% to 57% and DME was 245 and 46  $\mu\text{mol g}^{-1}\text{h}^{-1}$  respectively.

#### 4.2.2.7 Effect of H<sub>2</sub>O and Zeolite Particle Size

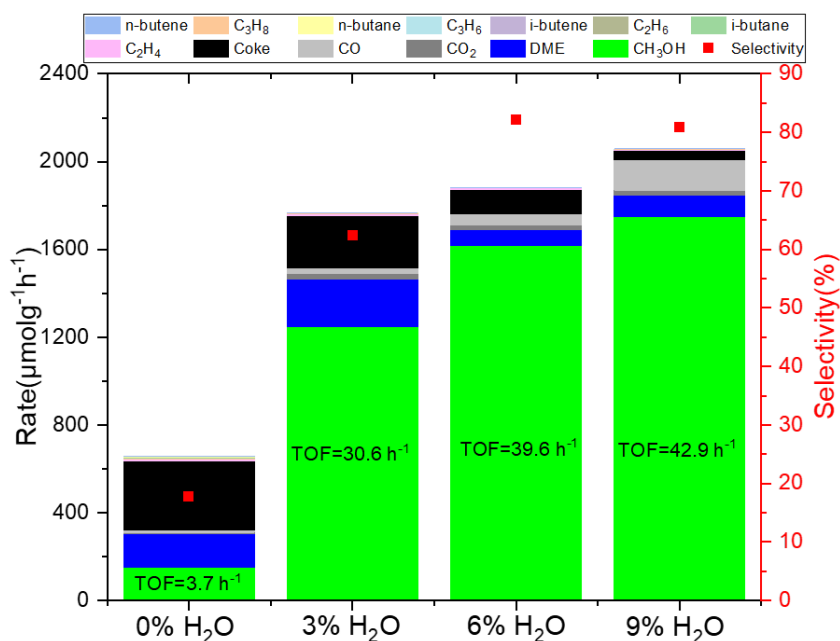


Figure 4.67. Activity test results of Micro-Cu-FER\_1 with different H<sub>2</sub>O contents, 325 °C, 40% methane, 15% N<sub>2</sub>O, 0-9% H<sub>2</sub>O and 42% He

Figure 4.67 and Figure 4.68 show the activity results of Micro-Cu-FER\_1 and Nano-Cu-FER\_1 containing 0, 3, 6 and 9% H<sub>2</sub>O in the feed. H<sub>2</sub>O vapor addition in the feed is known to increase methanol selectivity. H<sub>2</sub>O vapor increase in feed reduces overoxidation and eventually improves methanol selectivity [139], [140], [141]. Methanol is difficult to desorb from the surface; hence, in stepwise processes, H<sub>2</sub>O vapor is employed to desorb produced methanol from the active sites. Thus, an increase in methanol selectivity is occurred if H<sub>2</sub>O vapor aids in methanol desorption and prevents overoxidation. The presence of H<sub>2</sub>O vapor is also known to reduce coke production resulting in a longer catalyst lifetime. At Figure 4.67, it is observed that situations similar to these conclusions. In the Micro-Cu-FER\_1, methanol production (152, 1249, 1616 and 1749 μmol g<sup>-1</sup>h<sup>-1</sup> respectively) and methanol selectivity (18%, 62%, 83% and 81%, respectively) increased as H<sub>2</sub>O increased. Coke formation and C<sub>2</sub>+ production decreased also decreased with increasing H<sub>2</sub>O. Although the increase in values stabilized between 6 and 9% without showing very

large changes, the change between 0 and 3% is quite dramatic. The variation between 0% and 3% H<sub>2</sub>O has led to claims that H<sub>2</sub>O acts as an oxygen source for methanol production, but this is still debated as mentioned before in Chapter 2. In Micro-Cu-FER\_1, the best result was obtained in the case of 9% H<sub>2</sub>O with 81% selectivity and 1749  $\mu\text{mol g}^{-1}\text{h}^{-1}$  methanol production, which is well above the values in the literature especially in terms of both selectivity and production of methanol (best result in literature, Cu-SSZ-39, 350°C, 10:10:3:2 CH<sub>4</sub>, N<sub>2</sub>O, H<sub>2</sub>O, Ar 50% selectivity, 2100  $\mu\text{mol g}^{-1}\text{h}^{-1}$ ).

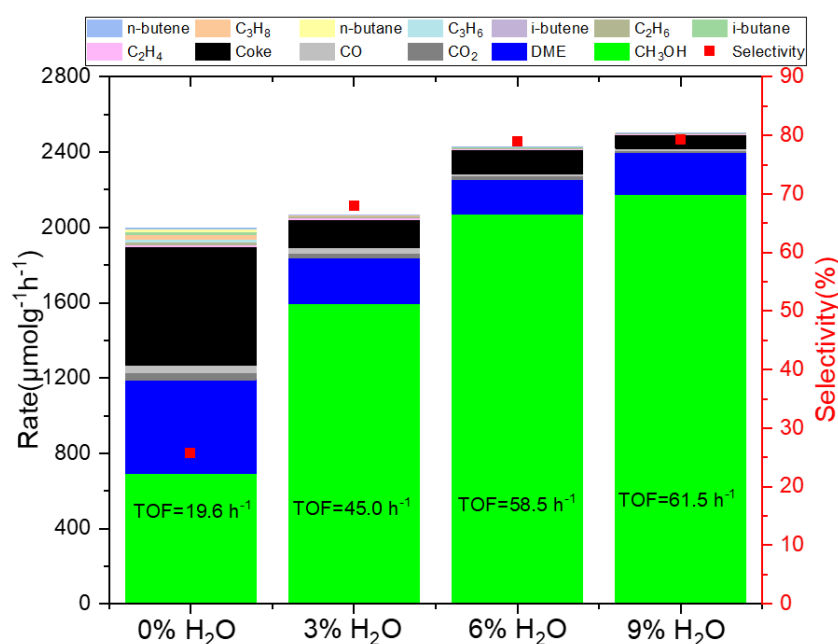


Figure 4.68. Activity test results of Nano-Cu-FER\_1 with different H<sub>2</sub>O contents, 325 °C, 40% methane, 15% N<sub>2</sub>O, 0-9% H<sub>2</sub>O and 42% He

Following Micro-Cu-FER\_1, Nano-Cu-FER\_1 was also analyzed for H<sub>2</sub>O and a similar situation was observed for this sample and can be seen from Figure 4.68. Methanol production (694, 1594, 2071 and 2174  $\mu\text{mol g}^{-1}\text{h}^{-1}$ ) and methanol selectivity (26%, 68%, 79% and 79% respectively) increased with increasing H<sub>2</sub>O content (up to 9%). Coke formation and C<sub>2</sub>+ formation also decreased with increasing H<sub>2</sub>O. In the case of Nano-Cu-FER\_1, there was no sharp change at 6 and 9% H<sub>2</sub>O, while a dramatic increase was observed at 0 and 3%. Similar to Micro-Cu-FER\_1, the best result was observed at 9% H<sub>2</sub>O with 2174  $\mu\text{mol g}^{-1}\text{h}^{-1}$  methanol

formation rate and 79% metanol selectivity. Increasing H<sub>2</sub>O more than 9% resulted in deactivation, i.e. decreased methanol production (at 15% H<sub>2</sub>O approximately 600  $\mu\text{mol g}^{-1}\text{h}^{-1}$  MeOH formation rate).

Considering the effect of zeolite particle size, CO and CO<sub>2</sub> formation is considerably low for Nano-Cu-FER\_1, especially in cases containing 6 and 9% H<sub>2</sub>O (9 and 10  $\mu\text{mol g}^{-1}\text{h}^{-1}$  for CO, 19 and 14  $\mu\text{mol g}^{-1}\text{h}^{-1}$  for CO<sub>2</sub> respectively) when comparing with Micro-Cu-FER\_1 (52 and 136  $\mu\text{mol g}^{-1}\text{h}^{-1}$  for CO, 24 and 24  $\mu\text{mol g}^{-1}\text{h}^{-1}$  for CO<sub>2</sub> respectively). The selectivity of Micro-Cu-FER\_1 at 6% and 9% H<sub>2</sub>O is slightly higher than Nano-Cu-FER\_1, and the reason for is that the DME production is much higher in the Nano-Cu-FER\_1 sample and therefore the methanol selectivity is relatively low which can be seen easily from Figure 4.67 and Figure 4.68. However, again with respect to methanol+DME selectivity, Nano-Cu-FER\_1 is higher for 6% H<sub>2</sub>O (93% vs 89%) and 9% H<sub>2</sub>O (93% vs 90%).

#### 4.2.2.8 Activation Energy Calculations

In Figure 4.69, Figure 4.70, Figure 4.71, Figure 4.72 and Figure 4.73, the activation energies of the catalysts Nano-Cu-FER and Micro-Cu-FER were calculated at 3 different temperatures (311, 318 and 325 °C) and 3% H<sub>2</sub>O content.

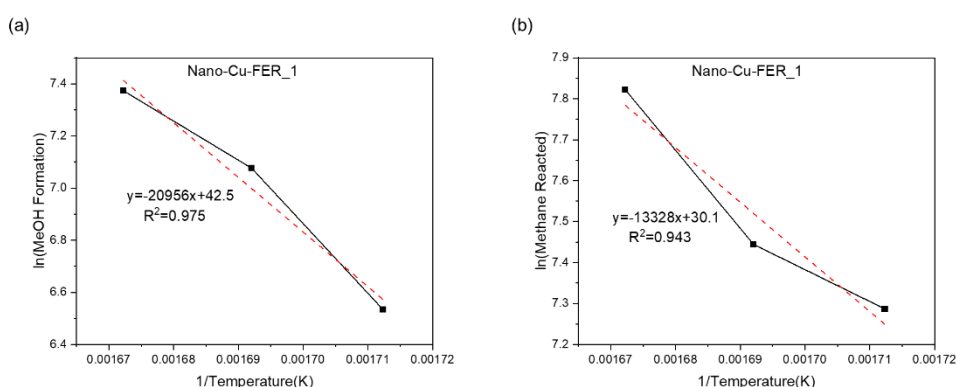


Figure 4.69. Activation energy plot of Nano-Cu-FER\_1 a) MeOH and b) Methane

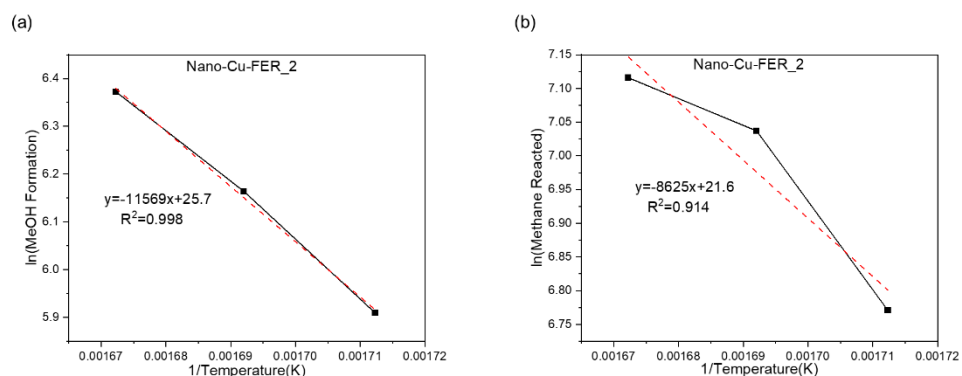


Figure 4.70 Activation energy plot of Nano-Cu-FER\_2 a) MeOH and b) Methane

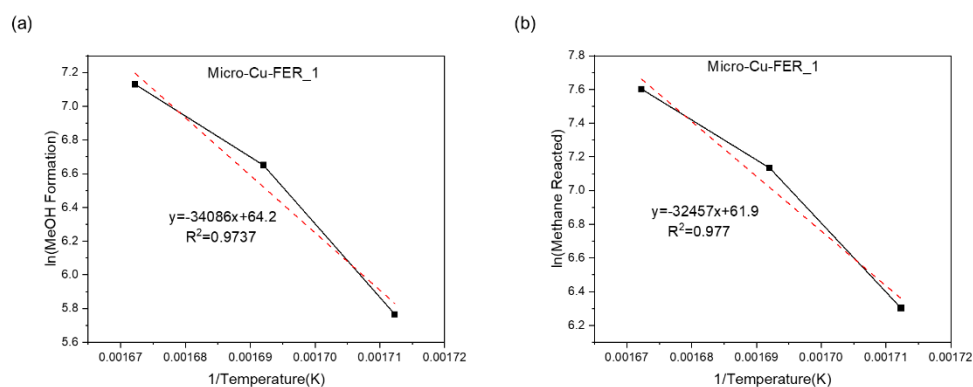


Figure 4.71. Activation energy plot of Micro-Cu-FER\_1 a) MeOH and b) Methane

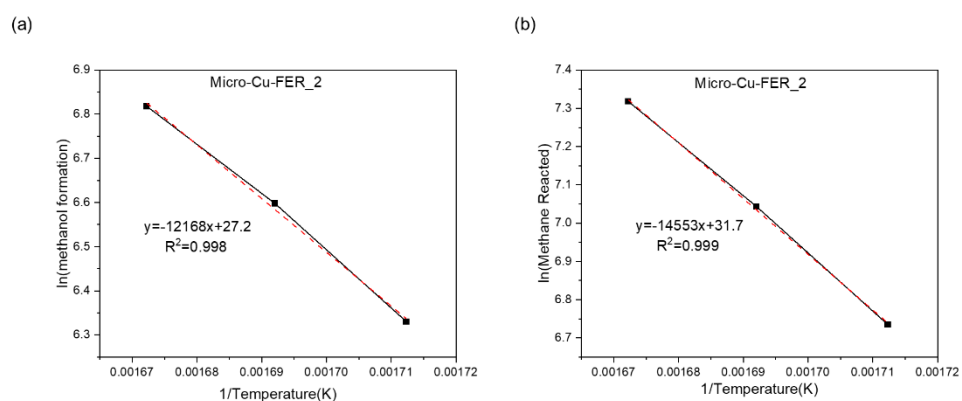


Figure 4.72. Activation energy plot of Micro-Cu-FER\_2 a) MeOH and b) Methane

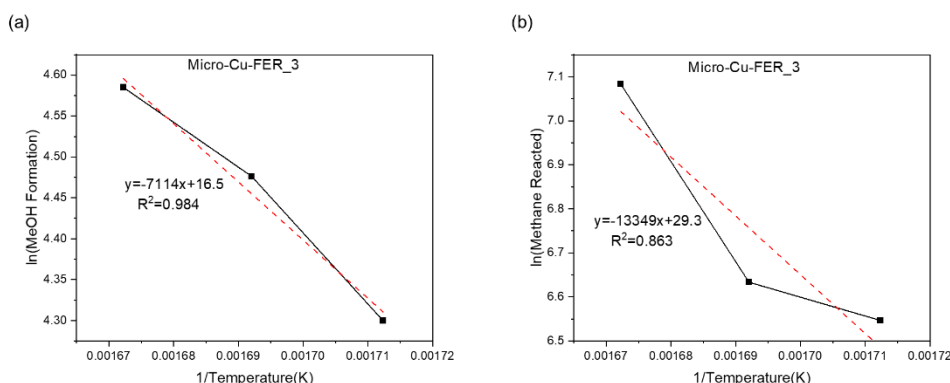


Figure 4.73. Activation energy plot of Micro-Cu-FER\_3 a) MeOH and b) Methane

As seen in Table 4.3,  $E_a$  methane and  $E_a$  methanol decreased in Micro-Cu-FER and Nano-Cu-FER samples as the copper content increased. The Micro-Cu-FER\_1 and relatively the Nano-Cu-FER\_1 sample gave a result far above the methanol activation energy values in the literature. In addition, activation energy values of Nano-Cu-FER is for methanol considerably lower than Micro-Cu-FER. As mentioned in the literature, monomer active sites generally give high methanol formation activation energy while dimer structures give lower activation energy. While Micro-Cu-FER\_1 contains only CuOH active sites, Micro-Cu-FER\_2, Micro-Cu-FER\_3 and Nano-Cu-FER\_2 contain dimer active sites according to UV-Vis results.

Table 4.3. Activation energy values of FER samples

Catalyst Name	$E_a$ Methane (kJ/mol)	$E_a$ Methanol (kJ/mol)
Micro-Cu-FER_1	269.8	283.4
Micro-Cu-FER_2	121.0	101.2
Micro-Cu-FER_3	111	59.2
Nano-Cu-FER_1	110.8	174.2
Nano-Cu-FER_2	71.7	96.2

#### 4.2.2.9 Effect of Brønsted Acidity and Mesoporous or Nanosized Zeolite on Activity Test Results

Although the Brønsted Acid Site was examined with the effect of  $\text{Na}^+$  ion, this situation can also be explained with different samples. It has been previously explained through  $\text{NH}_3$ -TPD studies in the literature that the BAS decreases as the amount of copper exchanged into the zeolite structure increases [114]. In all samples with different frame structures, it is also seen that as BAS increases, methanol production also increases. Again, studies in the literature, it was stated that BAS sites are not directly active sites but are involved in the methanol production mechanism [17]. The situation seen in Micro-Cu-SSZ-39\_2 zeolite at very low loadings is an example that these sites are not methanol active sites. At the same time, high percent of  $\text{H}_2\text{O}$  also have the effect of reducing methanol production by blocking BAS. Moreover, methanol to DME conversion reactions also require acid sites and Le Chatelier's principle, BAS sites take advantage of methanol production, which will increase as the amount of DME increases.

A clear direct assessment of the mesopore effect is not possible due to the characterization results. Although both mesoporous samples show better results in terms of selectivity, this cannot be directly attributed to the mesopore. In the case of the Meso-Steam-FER sample, the extra-framework Al sites visible in Al-NMR and therefore the changing Si/Al ratio in the structure prevent a direct comparison even though they have similar Cu/Al ratios. In the Meso-CTABr-FER sample, the effect of the extra phases in the XRD peaks supported by  $\text{N}_2$  physisorption is also not fully known, so it is not possible to make a direct interpretation, although a positive result is seen here. When looking at Nano-Cu-FER zeolites, CO,  $\text{CO}_2$  production is lower at optimum conditions with respect to Micro-Cu-FER, while at the same time DME+MeOH selectivity is higher.



## CHAPTER 5

### CONCLUSION

In this study, partial oxidation of methane to methanol was carried out using copper-containing zeolites using  $N_2O$  as the oxidant. Firstly, the effect of copper was examined and it was observed that methanol production increased with decreasing copper content in all samples except Micro-Cu-SSZ-39. Over Micro-Cu-SSZ-39, the results were not stable even though high methanol was produced at low copper content ( $0.08 \text{ mmol Cu g}^{-1}$ ) since methanol was converted to olefins as the reaction progresses. The unstability phenomena was not observed at higher Cu concentrations of SSZ-39 ( $0.19 \text{ mmol Cu g}^{-1}$ ). The highest methanol production was observed ( $1249 \mu\text{mol CH}_3\text{OH g}^{-1} \text{ h}^{-1}$ ,  $31 \text{ h}^{-1}$ ) on Micro-Cu-FER\_1 ( $0.04 \text{ mmol Cu g}^{-1}$ ) among the tested microporous zeolites (FER, CHA, AEI) at  $325 \text{ }^\circ\text{C}$  and  $100 \text{ sccm}$   $40\%$  methane,  $15\%$   $N_2O$ ,  $3\%$   $H_2O$  and  $42\%$  He flow.

$Na^+$  content of the Cu-zeolites had a negative effect on methanol production as the methanol desorption is linked to presence of protonic sites on zeolites. Decreased  $N_2O$  concentration also decreased the methanol formation due to insufficient active site formation. Calcination of the Cu-exchanged samples resulted in a lower methanol formation rate, most probably due to formation of more stable but less active  $CuO_x$  sites upon heat treatment. The effect of mesopores on FER structure (Meso-Steam-FER and Meso-CTABr-FER) could not be interpreted due to slightly different Al content and presence of extra-framework Al sites even though better methanol selectivity and methanol formation rates were observed.

The Micro-Cu-FER\_1 sample tested by reactant heating method experienced deactivation upon reuse, while Micro-Cu-FER\_1 tested by helium heating remained active. However, no deactivation was observed in the reuse of Micro-Cu-FER\_3R

(higher Cu content) in reactant heating due to better stability of the active sites on higher copper content.

Since FER was the most stable and gave the highest activity results in the helium heating method, the Nano-FER was synthesized and tested after copper introduction. As a result, Nano-FER showed higher methanol activity and selectivity results compared to Micro-Cu-FER. Micro-Cu-FER\_1 and Nano-Cu-FER\_1 samples showing the best activity were tested at different H<sub>2</sub>O ratios and a remarkably higher methanol selectivity (ca. 81%) was observed when the H<sub>2</sub>O concentration was increased to 9%. The best result in terms of methanol production of 2179  $\mu\text{mol g}^{-1}\text{h}^{-1}$  with 79% selectivity was obtained over Nano-Cu-FER\_1 using 9% H<sub>2</sub>O.

Lastly, higher methanol activation energy values were observed on FER structures when the copper loading decreases, indicating the difficulty of not only methanol production but also active site formation on infinitesimal concentration of copper.

## REFERENCES

- [1] G. Rocher-Ros *et al.*, “Global methane emissions from rivers and streams,” *Nature* 2023 621:7979, vol. 621, no. 7979, pp. 530–535, Aug. 2023, doi: 10.1038/s41586-023-06344-6.
- [2] S. Liu, M. Xue, X. Cui, and W. Peng, “A review on the methane emission detection during offshore natural gas hydrate production,” *Front Energy Res*, vol. 11, p. 1130810, Jan. 2023, doi: 10.3389/FENRG.2023.1130810/BIBTEX.
- [3] G. Rocher-Ros *et al.*, “Global methane emissions from rivers and streams,” *Nature* 2023 621:7979, vol. 621, no. 7979, pp. 530–535, Aug. 2023, doi: 10.1038/s41586-023-06344-6.
- [4] “2021-2025: Rebound and beyond – Gas 2020 – Analysis - IEA.” Accessed: Jun. 21, 2024. [Online]. Available: <https://www.iea.org/reports/gas-2020/2021-2025-rebound-and-beyond>
- [5] “Global atmospheric CH<sub>4</sub> concentration by month 2023 | Statista.” Accessed: Jun. 20, 2024. [Online]. Available: <https://www.statista.com/statistics/1314344/atmospheric-concentration-of-ch4-historic-monthly/>
- [6] K. Wang, J. Zhang, B. Cai, and S. Yu, “Emission factors of fugitive methane from underground coal mines in China: Estimation and uncertainty,” *Appl Energy*, vol. 250, pp. 273–282, Sep. 2019, doi: 10.1016/J.APENERGY.2019.05.024.
- [7] “2023 Global Gas Flaring Tracker Report.” Accessed: Jun. 20, 2024. [Online]. Available: <https://www.worldbank.org/en/topic/extractiveindustries/publication/2023-global-gas-flaring-tracker-report>

- [8] M. Agerton, B. Gilbert, and G. B. Upton, “The Economics of Natural Gas Flaring and Methane Emissions in US Shale: An Agenda for Research and Policy,” *Rev Environ Econ Policy*, vol. 17, no. 2, pp. 251–273, Jun. 2023, doi: 10.1086/725004.
- [9] G. Rocher-Ros *et al.*, “Global methane emissions from rivers and streams,” *Nature* 2023 621:7979, vol. 621, no. 7979, pp. 530–535, Aug. 2023, doi: 10.1038/s41586-023-06344-6.
- [10] B. Han *et al.*, “A review of the direct oxidation of methane to methanol,” *Chinese Journal of Catalysis*, vol. 37, no. 8, pp. 1206–1215, Aug. 2016, doi: 10.1016/S1872-2067(15)61097-X.
- [11] B. Wang, S. Albarracín-Suazo, Y. Pagán-Torres, and E. Nikolla, “Advances in methane conversion processes,” *Catal Today*, vol. 285, pp. 147–158, May 2017, doi: 10.1016/J.CATTOD.2017.01.023.
- [12] V. Galvita and R. Bos, *Methane Conversion Routes: Status and Prospects*, vol. 76. Royal Society of Chemistry, 2023. doi: 10.1039/9781839160257.
- [13] G. A. Olah, *Beyond Oil and Gas: The Methanol Economy*. 2005. doi: 10.1002/anie.200462121.
- [14] I. Yarulina, A. D. Chowdhury, F. Meirer, B. M. Weckhuysen, and J. Gascon, “Recent trends and fundamental insights in the methanol-to-hydrocarbons process,” *Nat Catal*, vol. 1, no. 6, pp. 398–411, Jun. 2018, doi: 10.1038/s41929-018-0078-5.
- [15] H. Zhang, J. Li, D. Wang, Y. Wang, and H. Xiong, “A review on the active sites for direct oxidation of methane to methanol by copper-zeolites: Coordination structure, formation and activity,” *Coord Chem Rev*, vol. 503, p. 215637, Mar. 2024, doi: 10.1016/J.CCR.2023.215637.
- [16] P. Tomkins, M. Ranocchiari, and J. A. Van Bokhoven, “Direct Conversion of Methane to Methanol under Mild Conditions over Cu-Zeolites and beyond,”

- Acc Chem Res*, vol. 50, no. 2, pp. 418–425, Feb. 2017, doi: 10.1021/acs.accounts.6b00534.
- [17] U. Engedahl, A. A. Arvidsson, H. Grönbeck, and A. Hellman, “Reaction Mechanism for Methane-to-Methanol in Cu-SSZ-13: First-Principles Study of the Z2[Cu2O] and Z2[Cu2OH] Motifs,” *Catalysts*, vol. 11, no. 1, p. 17, Dec. 2020, doi: 10.3390/catal11010017.
- [18] V. Arutyunov, *Direct Methane to Methanol: Foundations and Prospects of the Process*. Elsevier, 2014. doi: 10.1016/C2012-0-06330-2.
- [19] G. A. Foulds and B. F. Gray, “Homogeneous gas-phase partial oxidation of methane to methanol and formaldehyde,” *Fuel Processing Technology*, vol. 42, no. 2–3, pp. 129–150, Apr. 1995, doi: 10.1016/0378-3820(94)00122-A.
- [20] W. C. Liu, J. Baek, and G. A. Somorjai, “The Methanol Economy: Methane and Carbon Dioxide Conversion,” *Top Catal*, vol. 61, no. 7–8, pp. 530–541, Jun. 2018, doi: 10.1007/s11244-018-0907-4.
- [21] M. Rivarolo, D. Bellotti, L. Magistri, and A. F. Massardo, “Feasibility study of methanol production from different renewable sources and thermo-economic analysis,” *Int J Hydrogen Energy*, vol. 41, no. 4, pp. 2105–2116, Jan. 2016, doi: 10.1016/J.IJHYDENE.2015.12.128.
- [22] R. C. Baliban, J. A. Elia, and C. A. Floudas, “Toward novel hybrid biomass, coal, and natural gas processes for satisfying current transportation fuel demands, 1: Process alternatives, gasification modeling, process simulation, and economic analysis,” *Ind Eng Chem Res*, vol. 49, no. 16, pp. 7343–7370, Aug. 2010, doi: 10.1021/ie100063y.
- [23] R. C. Baliban, J. A. Elia, and C. A. Floudas, “Biomass and natural gas to liquid transportation fuels: Process synthesis, global optimization, and topology analysis,” *Ind Eng Chem Res*, vol. 52, no. 9, pp. 3381–3406, Mar. 2013, doi: 10.1021/ie3024643.

- [24] S. I. Chan, K. H. C. Chen, S. S. F. Yu, C. L. Chen, and S. S. J. Kuo, "Toward Delineating the Structure and Function of the Particulate Methane Monooxygenase from Methanotrophic Bacteria," *Biochemistry*, vol. 43, no. 15, pp. 4421–4430, Apr. 2004, doi: 10.1021/bi0497603.
- [25] A. C. Rosenzweig, C. A. Frederick, S. J. Lippard, and P. Nordlund, "Crystal structure of a bacterial non-haem iron hydroxylase that catalyses the biological oxidation of methane," *Nature*, vol. 366, no. 6455, pp. 537–543, 1993, doi: 10.1038/366537a0.
- [26] J. Shan *et al.*, "Conversion of methane to methanol with a bent mono( $\mu$ -oxo)dinickel anchored on the internal surfaces of micropores," *Langmuir*, vol. 30, no. 28, pp. 8558–8569, Jul. 2014, doi: doi/10.1021/la501184b.
- [27] H. Zhang, J. Li, D. Wang, Y. Wang, and H. Xiong, "A review on the active sites for direct oxidation of methane to methanol by copper-zeolites: Coordination structure, formation and activity," *Coord Chem Rev*, vol. 503, p. 215637, Mar. 2024, doi: 10.1016/J.CCR.2023.215637.
- [28] M. H. Mahyuddin, Y. Shiota, A. Staykov, and K. Yoshizawa, "Theoretical Overview of Methane Hydroxylation by Copper-Oxygen Species in Enzymatic and Zeolitic Catalysts," *Acc Chem Res*, vol. 51, no. 10, pp. 2382–2390, Oct. 2018, doi: 10.1021/acs.accounts.8b00236.
- [29] S. Kulprathipanja, *Zeolites in Industrial Separation and Catalysis*. Wiley, 2010. doi: 10.1002/9783527629565.
- [30] J. Čejka, A. Corma, and S. Zones, *Zeolites and Catalysis: Synthesis, Reactions and Applications*. Wiley, 2010. doi: 10.1002/9783527630295.
- [31] "Database of Zeolite Structures." Accessed: Jun. 21, 2024. [Online]. Available: <https://www.iza-structure.org/databases/>
- [32] D. S. Coombs *et al.*, "Recommended nomenclature for zeolite minerals: report of the subcommittee on zeolites of the International Mineralogical

- Association, Commission on New Minerals and Mineral Names,” *Mineral Mag*, vol. 62, no. 4, pp. 533–571, 1998, doi: 10.1180/002646198547800.
- [33] M. Sunil Kumar, M. S. Alphin, S. Manigandan, S. Vignesh, S. Vigneshwaran, and T. Subash, “A review of comparison between the traditional catalyst and zeolite catalyst for ammonia-selective catalytic reduction of NO<sub>x</sub>,” *Fuel*, vol. 344, p. 128125, Jul. 2023, doi: 10.1016/J.FUEL.2023.128125.
- [34] L. Velarde, M. S. Nabavi, E. Escalera, M. L. Antti, and F. Akhtar, “Adsorption of heavy metals on natural zeolites: A review,” *Chemosphere*, vol. 328, p. 138508, Jul. 2023, doi: 10.1016/J.CHEMOSPHERE.2023.138508.
- [35] M. E. Davis, “Zeolites from a materials chemistry perspective,” *Chemistry of Materials*, vol. 26, no. 1, pp. 239–245, Jan. 2014, doi: 10.1021/CM401914U.
- [36] S. Goel, S. I. Zones, and E. Iglesia, “Synthesis of zeolites via interzeolite transformations without organic structure-directing agents,” *Chemistry of Materials*, vol. 27, no. 6, pp. 2056–2066, Mar. 2015, doi: 10.1021/cm504510f.
- [37] C. S. Cundy and P. A. Cox, “The hydrothermal synthesis of zeolites: History and development from the earliest days to the present time,” *Chem Rev*, vol. 103, no. 3, pp. 663–701, Mar. 2003, doi: 10.1021/cr020060i.
- [38] R. M. Barrer, “Zeolites: Their Nucleation and Growth,” pp. 11–27, Jul. 1989, doi: 10.1021/BK-1989-0398.CH002.
- [39] M. Moliner, C. Martínez, and A. Corma, “Synthesis strategies for preparing useful small pore zeolites and zeotypes for gas separations and catalysis,” *Chemistry of Materials*, vol. 26, no. 1, pp. 246–258, Jan. 2014, doi: 10.1021/CM4015095.
- [40] M. Moliner, C. Martínez, and A. Corma, “Multipore Zeolites: Synthesis and Catalytic Applications,” *Angewandte Chemie International Edition*, vol. 54, no. 12, pp. 3560–3579, Mar. 2015, doi: 10.1002/ANIE.201406344.

- [41] M. Dusselier and M. E. Davis, “Small-Pore Zeolites: Synthesis and Catalysis,” *Chem Rev*, vol. 118, no. 11, pp. 5265–5329, Jun. 2018, doi: 10.1021/ACS.CHEMREV.7B00738/ASSET/IMAGES/MEDIUM/CR-2017-007389\_0042.GIF.
- [42] M. Moliner, C. Martínez, and A. Corma, “Synthesis strategies for preparing useful small pore zeolites and zeotypes for gas separations and catalysis,” *Chemistry of Materials*, vol. 26, no. 1, pp. 246–258, Jan. 2014, doi: 10.1021/CM4015095.
- [43] S. Smeets and X. Zou, *Zeolites in Catalysis: Properties and Applications. Chapter 2: Zeolite Structures*. Royal Society of Chemistry, 2017. doi: 10.1039/9781788010610-00037.
- [44] J. Li, A. Corma, and J. Yu, “Synthesis of new zeolite structures,” *Chem Soc Rev*, vol. 44, no. 20, pp. 7112–7127, Oct. 2015, doi: 10.1039/C5CS00023H.
- [45] J. Li, M. Gao, W. Yan, and J. Yu, “Regulation of the Si/Al ratios and Al distributions of zeolites and their impact on properties,” *Chem Sci*, vol. 14, no. 8, pp. 1935–1959, Feb. 2023, doi: 10.1039/D2SC06010H.
- [46] X. Zhao, J. Xu, and F. Deng, “Solid-state NMR for metal-containing zeolites: From active sites to reaction mechanism,” *Front Chem Sci Eng*, vol. 14, no. 2, pp. 159–187, Jan. 2020, doi: 10.1007/S11705-019-1885-1.
- [47] S. Li *et al.*, “Brønsted/Lewis acid synergy in dealuminated HY zeolite: A combined solid-state NMR and theoretical calculation study,” *J Am Chem Soc*, vol. 129, no. 36, pp. 11161–11171, Sep. 2007, doi: 10.1021/ja072767y.
- [48] S. M. T. Almutairi *et al.*, “Influence of extraframework aluminum on the Brønsted acidity and catalytic reactivity of faujasite zeolite,” *ChemCatChem*, vol. 5, no. 2, pp. 452–466, Feb. 2013, doi: 10.1002/cctc.201200612.
- [49] A. Bolshakov, R. van de Poll, T. van Bergen-Brenkman, S. C. C. Wiedemann, N. Kosinov, and E. J. M. Hensen, “Hierarchically porous FER zeolite obtained

- via FAU transformation for fatty acid isomerization,” *Appl Catal B*, vol. 263, p. 118356, Apr. 2020, doi: 10.1016/J.APCATB.2019.118356.
- [50] H. Xu, J. Zhu, L. Zhu, E. Zhou, and C. Shen, “Advances in the Synthesis of Ferrierite Zeolite,” *Molecules* 2020, Vol. 25, Page 3722, vol. 25, no. 16, p. 3722, Aug. 2020, doi: 10.3390/MOLECULES25163722.
- [51] R. Gramlich-Meier, W. M. Meier, and B. K. Smith, “On faults in the framework structure of the zeolite ferrierite,” *Z Kristallogr Cryst Mater*, vol. 169, no. 1–4, pp. 201–210, Dec. 1984, doi: 10.1524/ZKRI.1984.169.14.201.
- [52] H. Xu, L. Zhu, Q. Wu, X. Meng, and F. S. Xiao, “Advances in the synthesis and application of the SSZ-39 zeolite,” *Inorg Chem Front*, vol. 9, no. 6, pp. 1047–1057, Mar. 2022, doi: 10.1039/D1QI01636A.
- [53] “AEI: Framework Type.” Accessed: Jun. 21, 2024. [Online]. Available: <https://europe.iza-structure.org/IZA-SC/framework.php?ID=20>
- [54] R. Ransom, J. Coote, R. Moulton, F. Gao, and D. F. Shantz, “Synthesis and Growth Kinetics of Zeolite SSZ-39,” *Ind Eng Chem Res*, vol. 56, no. 15, pp. 4350–4356, Apr. 2017, doi: 10.1021/ACS.IECR.7B00629.
- [55] N. Martín, C. R. Boruntea, M. Moliner, and A. Corma, “Efficient synthesis of the Cu-SSZ-39 catalyst for DeNO<sub>x</sub> applications,” *Chemical Communications*, vol. 51, no. 55, pp. 11030–11033, Jun. 2015, doi: 10.1039/C5CC03200H.
- [56] “CHA: Framework Type.” Accessed: Jun. 21, 2024. [Online]. Available: <https://asia.iza-structure.org/IZA-SC/framework.php?ID=65>
- [57] K. Mlekodaj, M. Bernauer, J. E. Olszowka, P. Klein, V. Pashkova, and J. Dedecek, “Synthesis of the Zeolites from SBU: An SSZ-13 Study,” *Chemistry of Materials*, vol. 33, no. 5, pp. 1781–1788, Mar. 2021, doi: 10.1021/acs.chemmater.0c04710.

- [58] L. Han *et al.*, “Preparation of SSZ-13 zeolites and their NH<sub>3</sub>-selective catalytic reduction activity,” *Microporous and Mesoporous Materials*, vol. 261, pp. 126–136, May 2018, doi: 10.1016/J.MICROMESO.2017.11.012.
- [59] Z. Li, M. T. Navarro, J. Martínez-Triguero, J. Yu, and A. Corma, “Synthesis of nano-SSZ-13 and its application in the reaction of methanol to olefins,” *Catal Sci Technol*, vol. 6, no. 15, pp. 5856–5863, Jul. 2016, doi: 10.1039/C6CY00433D.
- [60] P. J. Smeets, M. H. Groothaert, and R. A. Schoonheydt, “Cu based zeolites: A UV–vis study of the active site in the selective methane oxidation at low temperatures,” *Catal Today*, vol. 110, no. 3–4, pp. 303–309, Dec. 2005, doi: 10.1016/J.CATTOD.2005.09.028.
- [61] M. H. Groothaert, P. J. Smeets, B. F. Sels, P. A. Jacobs, and R. A. Schoonheydt, “Selective oxidation of methane by the bis( $\mu$ -oxo)dicopper core stabilized on ZSM-5 and mordenite zeolites,” *J Am Chem Soc*, vol. 127, no. 5, pp. 1394–1395, Feb. 2005, doi: 10.1021/JA047158U.
- [62] J. S. Woertink *et al.*, “A [Cu<sub>2</sub>O]<sub>2</sub><sup>+</sup> core in Cu-ZSM-5, the active site in the oxidation of methane to methanol,” *Proc Natl Acad Sci U S A*, vol. 106, no. 45, pp. 18908–18913, Nov. 2009, doi: 10.1073/PNAS.0910461106.
- [63] X. Yu, L. Zhong, and S. Li, “Catalytic cycle of the partial oxidation of methane to methanol over Cu-ZSM-5 revealed using DFT calculations,” *Physical Chemistry Chemical Physics*, vol. 23, no. 8, pp. 4963–4974, Mar. 2021, doi: 10.1039/D0CP06696F.
- [64] P. J. Smeets *et al.*, “Oxygen precursor to the reactive intermediate in methanol synthesis by Cu-ZSM-5,” *J Am Chem Soc*, vol. 132, no. 42, pp. 14736–14738, Oct. 2010, doi: 10.1021/JA106283U.
- [65] G. Li, P. Vassilev, M. Sanchez-Sanchez, J. A. Lercher, E. J. M. Hensen, and E. A. Pidko, “Stability and reactivity of copper oxo-clusters in ZSM-5 zeolite

- for selective methane oxidation to methanol,” *J Catal*, vol. 338, pp. 305–312, Jun. 2016, doi: 10.1016/J.JCAT.2016.03.014.
- [66] M. A. C. Markovits, A. Jentys, M. Tromp, M. Sanchez-Sanchez, and J. A. Lercher, “Effect of Location and Distribution of Al Sites in ZSM-5 on the Formation of Cu-Oxo Clusters Active for Direct Conversion of Methane to Methanol,” *Top Catal*, vol. 59, no. 17–18, pp. 1554–1563, Oct. 2016, doi: 10.1007/S11244-016-0676-X.
- [67] X. Tang *et al.*, “Atomic Insights into the Cu Species Supported on Zeolite for Direct Oxidation of Methane to Methanol via Low-Damage HAADF-STEM,” *Advanced Materials*, vol. 35, no. 25, p. 2208504, Jun. 2023, doi: 10.1002/ADMA.202208504.
- [68] Y. Tsuchimura, H. Yoshida, M. Machida, S. Nishimura, K. Takahashi, and J. Ohyama, “Investigation of the Active-Site Structure of Cu-CHA Catalysts for the Direct Oxidation of Methane to Methanol Using In Situ UV-Vis Spectroscopy,” *Energy and Fuels*, vol. 37, no. 13, pp. 9411–9418, Jul. 2023, doi: 10.1021/ACS.ENERGYFUELS.3C00333.
- [69] B. Ipek *et al.*, “Formation of  $[\text{Cu}_2\text{O}_2]^{2+}$  and  $[\text{Cu}_2\text{O}]^{2+}$  toward C-H Bond Activation in Cu-SSZ-13 and Cu-SSZ-39,” *ACS Catal*, vol. 7, no. 7, pp. 4291–4303, Jul. 2017, doi: 10.1021/ACSCATAL.6B03005/SUPPL\_FILE/CS6B03005\_SI\_004.CIF.
- [70] X. Tang *et al.*, “Direct oxidation of methane to oxygenates on supported single Cu atom catalyst,” *Appl Catal B*, vol. 285, p. 119827, May 2021, doi: 10.1016/J.APCATB.2020.119827.
- [71] D. K. Pappas *et al.*, “Methane to Methanol: Structure-Activity Relationships for Cu-CHA,” *J Am Chem Soc*, vol. 139, no. 42, pp. 14961–14975, Oct. 2017, doi: 10.1021/JACS.7B06472.
- [72] Y. Zhang *et al.*, “Using Transient FTIR Spectroscopy to Probe Active Sites and Reaction Intermediates for Selective Catalytic Reduction of NO on

- Cu/SSZ-13 Catalysts,” *ACS Catal*, vol. 9, no. 7, pp. 6137–6145, Jul. 2019, doi: 10.1021/ACSCATAL.9B00759.
- [73] C. Zhou, S. Li, S. He, Z. Zhao, Y. Jiao, and H. Zhang, “Temperature-dependant active sites for methane continuous conversion to methanol over Cu-zeolite catalysts using water as the oxidant,” *Fuel*, vol. 329, p. 125483, Dec. 2022, doi: 10.1016/J.FUEL.2022.125483.
- [74] L. Burnett, M. Rysakova, K. Wang, J. González-Carballo, R. P. Tooze, and F. R. García-García, “Isothermal cyclic conversion of methane to methanol using copper-exchanged ZSM-5 zeolite materials under mild conditions,” *Appl Catal A Gen*, vol. 587, p. 117272, Oct. 2019, doi: 10.1016/J.APCATA.2019.117272.
- [75] B. Ipek *et al.*, “Formation of [Cu<sub>2</sub>O<sub>2</sub>]<sup>2+</sup> and [Cu<sub>2</sub>O]<sup>2+</sup> toward C-H Bond Activation in Cu-SSZ-13 and Cu-SSZ-39,” *ACS Catal*, vol. 7, no. 7, pp. 4291–4303, Jul. 2017, doi: 10.1021/ACSCATAL.6B03005.
- [76] L. Vilella and F. Studt, “The Stability of Copper Oxo Species in Zeolite Frameworks,” *Eur J Inorg Chem*, vol. 2016, no. 10, pp. 1514–1520, Apr. 2016, doi: 10.1002/EJIC.201501270.
- [77] Y. Mao and P. Hu, “Identification of the active sites and mechanism for partial methane oxidation to methanol over copper-exchanged CHA zeolites,” *Sci China Chem*, vol. 63, no. 6, pp. 850–859, Jun. 2020, doi: 10.1007/S11426-019-9695-9/METRICS.
- [78] F. Giordanino *et al.*, “Characterization of Cu-exchanged SSZ-13: a comparative FTIR, UV-Vis, and EPR study with Cu-ZSM-5 and Cu-β with similar Si/Al and Cu/Al ratios,” *Dalton Transactions*, vol. 42, no. 35, pp. 12741–12761, Aug. 2013, doi: 10.1039/C3DT50732G.
- [79] Q. Guo *et al.*, “Effect of the Nature and Location of Copper Species on the Catalytic Nitric Oxide Selective Catalytic Reduction Performance of the

- Copper/SSZ-13 Zeolite,” *ChemCatChem*, vol. 6, no. 2, pp. 634–639, Feb. 2014, doi: 10.1002/CCTC.201300775.
- [80] P. Vanelderen *et al.*, “Spectroscopic definition of the copper active sites in mordenite: Selective methane oxidation,” *J Am Chem Soc*, vol. 137, no. 19, pp. 6383–6392, May 2015, doi: 10.1021/JACS.5B02817.
- [81] V. L. Sushkevich, D. Palagin, M. Ranocchiari, and J. A. Van Bokhoven, “Selective anaerobic oxidation of methane enables direct synthesis of methanol,” *Science (1979)*, vol. 356, no. 6337, pp. 523–527, May 2017, doi: 10.1126/SCIENCE.AAM9035.
- [82] M. H. Mahyuddin, T. Tanaka, Y. Shiota, A. Staykov, and K. Yoshizawa, “Methane Partial Oxidation over  $[\text{Cu}_2(\mu\text{-O})]^{2+}$  and  $[\text{Cu}_3(\mu\text{-O})_3]^{2+}$  Active Species in Large-Pore Zeolites,” *ACS Catal*, vol. 8, no. 2, pp. 1500–1509, Feb. 2018, doi: 10.1021/ACSCATAL.7B03389.
- [83] J. Zheng *et al.*, “Importance of Methane Chemical Potential for Its Conversion to Methanol on Cu-Exchanged Mordenite,” *Chemistry – A European Journal*, vol. 26, no. 34, pp. 7563–7567, Jun. 2020, doi: 10.1002/CHEM.202000772.
- [84] C. Paolucci *et al.*, “Catalysis in a cage: Condition-dependent speciation and dynamics of exchanged cu cations in ssz-13 zeolites,” *J Am Chem Soc*, vol. 138, no. 18, pp. 6028–6048, May 2016, doi: 10.1021/JACS.6B02651.
- [85] D. Palagin, A. J. Knorpp, A. B. Pinar, M. Ranocchiari, and J. A. Van Bokhoven, “Assessing the relative stability of copper oxide clusters as active sites of a CuMOR zeolite for methane to methanol conversion: size matters?,” *Nanoscale*, vol. 9, no. 3, pp. 1144–1153, Jan. 2017, doi: 10.1039/C6NR07723D.
- [86] A. A. Verma *et al.*, “NO oxidation: A probe reaction on Cu-SSZ-13,” *J Catal*, vol. 312, pp. 179–190, Apr. 2014, doi: 10.1016/J.JCAT.2014.01.017.

- [87] J. Ohyama *et al.*, “Relationships among the Catalytic Performance, Redox Activity, and Structure of Cu-CHA Catalysts for the Direct Oxidation of Methane to Methanol Investigated Using In Situ XAFS and UV-Vis Spectroscopies,” *ACS Catal*, vol. 12, no. 4, pp. 2454–2462, Feb. 2022, doi: 10.1021/ACSCATAL.1C05559.
- [88] E. Borfecchia *et al.*, “Revisiting the nature of Cu sites in the activated Cu-SSZ-13 catalyst for SCR reaction,” *Chem Sci*, vol. 6, no. 1, pp. 548–563, Dec. 2014, doi: 10.1039/C4SC02907K.
- [89] V. L. Sushkevich, D. Palagin, and J. A. van Bokhoven, “The Effect of the Active-Site Structure on the Activity of Copper Mordenite in the Aerobic and Anaerobic Conversion of Methane into Methanol,” *Angewandte Chemie*, vol. 130, no. 29, pp. 9044–9048, Jul. 2018, doi: 10.1002/ANGE.201802922.
- [90] V. L. Sushkevich, R. Verel, and J. A. van Bokhoven, “Pathways of Methane Transformation over Copper-Exchanged Mordenite as Revealed by In Situ NMR and IR Spectroscopy,” *Angewandte Chemie*, vol. 132, no. 2, pp. 920–928, Jan. 2020, doi: 10.1002/ANGE.201912668.
- [91] B. Ipek and R. F. Lobo, “Catalytic conversion of methane to methanol on Cu-SSZ-13 using N<sub>2</sub>O as oxidant,” *Chemical Communications*, vol. 52, no. 91, pp. 13401–13404, Nov. 2016, doi: 10.1039/C6CC07893A.
- [92] A. J. Knorpp *et al.*, “Paired Copper Monomers in Zeolite Omega: The Active Site for Methane-to-Methanol Conversion,” *Angewandte Chemie International Edition*, vol. 60, no. 11, pp. 5854–5858, Mar. 2021, doi: 10.1002/ANIE.202014030.
- [93] M. H. Mahyuddin, A. Staykov, Y. Shiota, M. Miyanishi, and K. Yoshizawa, “Roles of Zeolite Confinement and Cu-O-Cu Angle on the Direct Conversion of Methane to Methanol by [Cu<sub>2</sub>(μ-O)]<sup>2+</sup>-Exchanged AEI, CHA, AFX, and MFI Zeolites,” *ACS Catal*, vol. 7, no. 6, pp. 3741–3751, Jun. 2017, doi: 10.1021/ACSCATAL.7B00588.

- [94] M. A. Artsiusheuski, J. A. Van Bokhoven, and V. L. Sushkevich, "Structure of Selective and Nonselective Dicopper (II) Sites in CuMFI for Methane Oxidation to Methanol," *ACS Catal*, vol. 12, no. 24, pp. 15626–15637, Dec. 2022, doi: 10.1021/ACSCATAL.2C05299.
- [95] A. Delabie, K. Pierloot, M. H. Grootaert, and R. A. Schoonheydt, "The Coordination of Cu II in Zeolites Structure and Spectroscopic Properties," *Eur. J. Inorg. Chem*, p. 515530, 2002, doi: 10.1002/1099-0682.
- [96] A. Godiksen, O. L. Isaksen, S. B. Rasmussen, P. N. R. Vennestrøm, and S. Mossin, "Site-Specific Reactivity of Copper Chabazite Zeolites with Nitric Oxide, Ammonia, and Oxygen," *ChemCatChem*, vol. 10, no. 2, pp. 366–370, Jan. 2018, doi: 10.1002/CCTC.201701357.
- [97] E. M. C. Alayon, M. Nachtegaal, A. Bodi, M. Ranocchiari, and J. A. Van Bokhoven, "Bis( $\mu$ -oxo) versus mono( $\mu$ -oxo)dicopper cores in a zeolite for converting methane to methanol: an in situ XAS and DFT investigation," *Physical Chemistry Chemical Physics*, vol. 17, no. 12, pp. 7681–7693, Mar. 2015, doi: 10.1039/C4CP03226H.
- [98] M. H. Mahyuddin, T. Tanaka, A. Staykov, Y. Shiota, and K. Yoshizawa, "Dioxygen Activation on Cu-MOR Zeolite: Theoretical Insights into the Formation of Cu<sub>2</sub>O and Cu<sub>3</sub>O<sub>3</sub> Active Species," *Inorg Chem*, vol. 57, no. 16, pp. 10146–10152, Aug. 2018, doi: 10.1021/ACS.INORGCHEM.8B01329.
- [99] T. Ikuno *et al.*, "Formation of Active Cu-oxo Clusters for Methane Oxidation in Cu-Exchanged Mordenite," *Journal of Physical Chemistry C*, vol. 123, no. 14, pp. 8759–8769, Apr. 2019, doi: 10.1021/ACS.JPCC.8B10293.
- [100] M. L. Tsai, R. G. Hadt, P. Vanelderen, B. F. Sels, R. A. Schoonheydt, and E. I. Solomon, "2+ Active site formation in Cu-ZSM-5: Geometric and electronic structure requirements for N<sub>2</sub>O activation," *J Am Chem Soc*, vol. 136, no. 9, pp. 3522–3529, Mar. 2014, doi: 10.1021/JA4113808.

- [101] K. Narsimhan, K. Iyoki, K. Dinh, and Y. Román-Leshkov, “Catalytic oxidation of methane into methanol over copper-exchanged zeolites with oxygen at low temperature,” *ACS Cent Sci*, vol. 2, no. 6, pp. 424–429, Jun. 2016, doi: 10.1021/ACSCENTSCI.6B00139.
- [102] A. Koishybay and D. F. Shantz, “Water Is the Oxygen Source for Methanol Produced in Partial Oxidation of Methane in a Flow Reactor over Cu-SSZ-13,” *J Am Chem Soc*, vol. 142, no. 28, pp. 11962–11966, Jul. 2020, doi: 10.1021/JACS.0C03283.
- [103] L. Sun, Y. Wang, C. Wang, Z. Xie, N. Guan, and L. Li, “Water-involved methane-selective catalytic oxidation by dioxygen over copper zeolites,” *CHEMPR*, vol. 7, pp. 1557–1568, 2021, doi: 10.1016/j.chempr.2021.02.026.
- [104] C. Zhou *et al.*, “Methane-selective oxidation to methanol and ammonia selective catalytic reduction of NO<sub>x</sub> over monolithic Cu/SSZ-13 catalysts: Are hydrothermal stability and active sites same?,” *Fuel*, vol. 309, p. 122178, Feb. 2022, doi: 10.1016/J.FUEL.2021.122178.
- [105] P. Xiao *et al.*, “Highly Effective Cu/AEI Zeolite Catalysts Contribute to Continuous Conversion of Methane to Methanol,” *ACS Catal*, vol. 13, no. 16, pp. 11057–11068, Aug. 2023, doi: 10.1021/ACSCATAL.3C02271.
- [106] P. Xiao *et al.*, “Effects of Al distribution in the Cu-exchanged AEI zeolites on the reaction performance of continuous direct conversion of methane to methanol,” *Appl Catal B*, vol. 325, May 2023, doi: 10.1016/j.apcatb.2023.122395.
- [107] E. Borfecchia *et al.*, “Evolution of active sites during selective oxidation of methane to methanol over Cu-CHA and Cu-MOR zeolites as monitored by operando XAS,” *Catal Today*, vol. 333, pp. 17–27, Aug. 2019, doi: 10.1016/J.CATTOD.2018.07.028.
- [108] G. Brezicki, J. Zheng, C. Paolucci, R. Schlögl, and R. J. Davis, “Effect of the Co-cation on Cu Speciation in Cu-exchanged mordenite and ZSM-5 catalysts

- for the oxidation of methane to methanol,” *ACS Catal*, vol. 11, no. 9, pp. 4973–4987, May 2021, doi: 10.1021/ACSCATAL.1C00543.
- [109] M. J. Wulfers, S. Teketel, B. Ipek, and R. F. Lobo, “Conversion of methane to methanol on copper-containing small-pore zeolites and zeotypes,” *Chemical Communications*, vol. 51, no. 21, pp. 4447–4450, Feb. 2015, doi: 10.1039/C4CC09645B.
- [110] M. B. Park, S. H. Ahn, A. Mansouri, M. Ranocchiari, and J. A. van Bokhoven, “Comparative Study of Diverse Copper Zeolites for the Conversion of Methane into Methanol,” *ChemCatChem*, vol. 9, no. 19, pp. 3705–3713, Oct. 2017, doi: 10.1002/CCTC.201700768.
- [111] Y. R. Jeong, H. Jung, J. Kang, J. W. Han, and E. D. Park, “Continuous Synthesis of Methanol from Methane and Steam over Copper-Mordenite,” *ACS Catal*, vol. 11, no. 3, pp. 1065–1070, Feb. 2021, doi: 10.1021/ACSCATAL.0C04592.
- [112] O. Memioglu and B. Ipek, “A potential catalyst for continuous methane partial oxidation to methanol using N<sub>2</sub>O: Cu-SSZ-39,” *Chemical Communications*, vol. 57, no. 11, pp. 1364–1367, Feb. 2021, doi: 10.1039/D0CC06534J.
- [113] S. Sogukkanli, T. Moteki, and M. Ogura, “Selective methanol formation via CO-assisted direct partial oxidation of methane over copper-containing CHA-type zeolites prepared by one-pot synthesis,” *Green Chemistry*, vol. 23, no. 5, pp. 2148–2154, Mar. 2021, doi: 10.1039/D0GC03645E.
- [114] K. T. Dinh *et al.*, “Continuous Partial Oxidation of Methane to Methanol Catalyzed by Diffusion-Paired Copper Dimers in Copper-Exchanged Zeolites,” *J Am Chem Soc*, vol. 141, no. 29, pp. 11641–11650, Jul. 2019, doi: 10.1021/JACS.9B04906.
- [115] M. Signorile, E. Borfecchia, S. Bordiga, and G. Berlier, “Influence of ion mobility on the redox and catalytic properties of Cu ions in zeolites,” *Chem Sci*, vol. 13, no. 35, pp. 10238–10250, Sep. 2022, doi: 10.1039/D2SC03565K.

- [116] Y. Wang *et al.*, “Synthesis and catalytic application of FER zeolites with controllable size,” *J Mater Chem A Mater*, vol. 7, no. 13, pp. 7573–7580, 2019, doi: 10.1039/C8TA09420A.
- [117] F. Wang *et al.*, “Shape selectivity conversion of biomass derived glycerol to aromatics over hierarchical HZSM-5 zeolites prepared by successive steaming and alkaline leaching: Impact of acid properties and pore constraint,” *Fuel*, vol. 262, Feb. 2020, doi: 10.1016/j.fuel.2019.116538.
- [118] X. Cheng, T. Cacciaguerra, D. Minoux, J. P. Dath, F. Fajula, and C. Gérardin, “Generation of parallelepiped-shaped mesopores and structure transformation in highly stable ferrierite zeolite crystals by framework desilication in NaOH solution,” *Microporous and Mesoporous Materials*, vol. 260, pp. 132–145, Apr. 2018, doi: 10.1016/j.micromeso.2017.05.050.
- [119] M. Dusselier and M. E. Davis, “Small-Pore Zeolites: Synthesis and Catalysis,” *Chem Rev*, vol. 118, no. 11, pp. 5265–5329, Jun. 2018.
- [120] T. D. Pham, Q. Liu, and R. F. Lobo, “Carbon dioxide and nitrogen adsorption on cation-exchanged SSZ-13 zeolites,” *Langmuir*, vol. 29, no. 2, pp. 832–839, Jan. 2013, doi: 10.1021/la304138z.
- [121] D. K. Pappas *et al.*, “Understanding and Optimizing the Performance of Cu-FER for The Direct CH<sub>4</sub> to CH<sub>3</sub>OH Conversion,” *ChemCatChem*, vol. 11, no. 1, pp. 621–627, Jan. 2019, doi: 10.1002/cctc.201801542.
- [122] V. J. Inglezakis, “The concept of ‘capacity’ in zeolite ion-exchange systems,” *J Colloid Interface Sci*, vol. 281, no. 1, pp. 68–79, Jan. 2005, doi: 10.1016/J.JCIS.2004.08.082.
- [123] Y. P. Khitev *et al.*, “Synthesis and catalytic properties of hierarchical micro/mesoporous materials based on FER zeolite,” *Microporous and Mesoporous Materials*, vol. 146, no. 1–3, pp. 201–207, Dec. 2011, doi: 10.1016/J.MICROMESO.2011.05.003.

- [124] R. K. Khaled, M. A. Wahba, M. D. Badry, M. F. Zawrah, and E. A. Heikal, “Highly ordered pure and indium-incorporated MCM-41 mesoporous adsorbents: synthesis, characterization and evaluation for dye removal,” *J Mater Sci*, vol. 57, no. 7, pp. 4504–4527, Feb. 2022, doi: 10.1007/S10853-022-06877-7.
- [125] A. R. Padmavathi *et al.*, “Impediment to growth and yeast-to-hyphae transition in *Candida albicans* by copper oxide nanoparticles,” *Biofouling*, vol. 36, no. 1, pp. 56–72, Jan. 2020, doi: 10.1080/08927014.2020.1715371.
- [126] M. Thommes *et al.*, “Physisorption of gases, with special reference to the evaluation of surface area and pore size distribution (IUPAC Technical Report),” *Pure Appl. Chem.*, vol. 87, no. 9–10, pp. 1051–1069, Oct. 2015, doi: 10.1515/pac-2014-1117.
- [127] T. Biligetu *et al.*, “Al distribution and catalytic performance of ZSM-5 zeolites synthesized with various alcohols,” *J Catal*, vol. 353, pp. 1–10, Sep. 2017, doi: 10.1016/J.JCAT.2017.06.026.
- [128] F. Göttl *et al.*, “Exploring the Impact of Active Site Structure on the Conversion of Methane to Methanol in Cu-Exchanged Zeolites,” *Angewandte Chemie International Edition*, vol. 63, no. 23, p. e202403179, Jun. 2024, doi: 10.1002/ANIE.202403179.
- [129] F. Göttl *et al.*, “Identifying hydroxylated copper dimers in SSZ-13 via UV-vis-NIR spectroscopy,” *Catal Sci Technol*, vol. 12, no. 9, pp. 2744–2748, May 2022, doi: 10.1039/D2CY00353H.
- [130] T. C. P. Pereira *et al.*, “Conversion of methane to methanol over Cu-MAZ (zeolite omega): An oxygen-free process using H<sub>2</sub>O and CO<sub>2</sub> as oxidants,” *Appl Catal B*, vol. 342, p. 123370, Mar. 2024, doi: 10.1016/J.APCATB.2023.123370.

- [131] A. Palčić *et al.*, “Nanosized Cu-SSZ-13 and Its Application in NH<sub>3</sub>-SCR,” *Catalysts* 2020, Vol. 10, Page 506, vol. 10, no. 5, p. 506, May 2020, doi: 10.3390/CATAL10050506.
- [132] I. Lezcano-Gonzalez *et al.*, “Chemical deactivation of Cu-SSZ-13 ammonia selective catalytic reduction (NH<sub>3</sub>-SCR) systems,” *Appl Catal B*, vol. 154–155, pp. 339–349, Jul. 2014, doi: 10.1016/J.APCATB.2014.02.037.
- [133] S. C. M. Mizuno *et al.*, “Stepwise methane to methanol conversion: Effect of copper loading on the formation of active species in copper-exchanged mordenite,” *Catal Today*, vol. 381, pp. 13–25, Dec. 2021, doi: 10.1016/J.CATTOD.2020.11.027.
- [134] Q. Yang *et al.*, “Lattice-Stabilized Chromium Atoms on Ceria for N<sub>2</sub>O Synthesis,” *ACS Catal*, vol. 13, no. 24, pp. 15977–15990, Dec. 2023, doi: 10.1021/ACSCATAL.3C04463.
- [135] M. B. Park, E. D. Park, and W. S. Ahn, “Recent progress in direct conversion of methane to methanol over copper-exchanged zeolites,” *Front Chem*, vol. 7, pp. 1–7, Jul. 2019, doi: 10.3389/FCHEM.2019.00514/BIBTEX.
- [136] J. Y. Lim, J. McGregor, A. J. Sederman, and J. S. Dennis, “The role of the Boudouard and water–gas shift reactions in the methanation of CO or CO<sub>2</sub> over Ni/γ-Al<sub>2</sub>O<sub>3</sub> catalyst,” *Chem Eng Sci*, vol. 152, pp. 754–766, Oct. 2016, doi: 10.1016/J.CES.2016.06.042.
- [137] P. Han *et al.*, “Critical role of al pair sites in methane oxidation to methanol on cu-exchanged mordenite zeolites,” *Catalysts*, vol. 11, no. 6, p. 751, Jun. 2021, doi: 10.3390/CATAL11060751/S1.
- [138] M. A. Artsiusheuski, R. Verel, J. A. van Bokhoven, and V. L. Sushkevich, “Methane Transformation over Copper-Exchanged Zeolites: From Partial Oxidation to C-C Coupling and Formation of Hydrocarbons,” *ACS Catal*, vol. 11, no. 20, pp. 12543–12556, Oct. 2021, doi: 10.1021/ACSCATAL.1C02547.

- [139] I. Gokce, M. O. Ozbek, and B. Ipek, "Conditions for higher methanol selectivity for partial CH<sub>4</sub> oxidation over Fe-MOR using N<sub>2</sub>O as the oxidant and comparison to Fe-SSZ-13, Fe-SSZ-39, Fe-FER, and Fe-ZSM-5," *J Catal*, vol. 427, p. 115113, Nov. 2023, doi: 10.1016/J.JCAT.2023.115113.
- [140] Y. Li *et al.*, "Synergistic effect of neighboring fe and cu cation sites boosts fencum-bea activity for the continuous direct oxidation of methane to methanol," *Catalysts*, vol. 11, no. 12, p. 1444, Dec. 2021, doi: 10.3390/CATAL11121444/S1.
- [141] Y. K. Chow *et al.*, "A Kinetic Study of Methane Partial Oxidation over Fe-ZSM-5 Using N<sub>2</sub>O as an Oxidant," *ChemPhysChem*, vol. 19, no. 4, pp. 402–411, Feb. 2018, doi: 10.1002/CPHC.201701202.



## APPENDICES

### A. Deconvolution of $^{27}\text{Al}$ -MAS-NMR and $^{29}\text{Si}$ -MAS-NMR

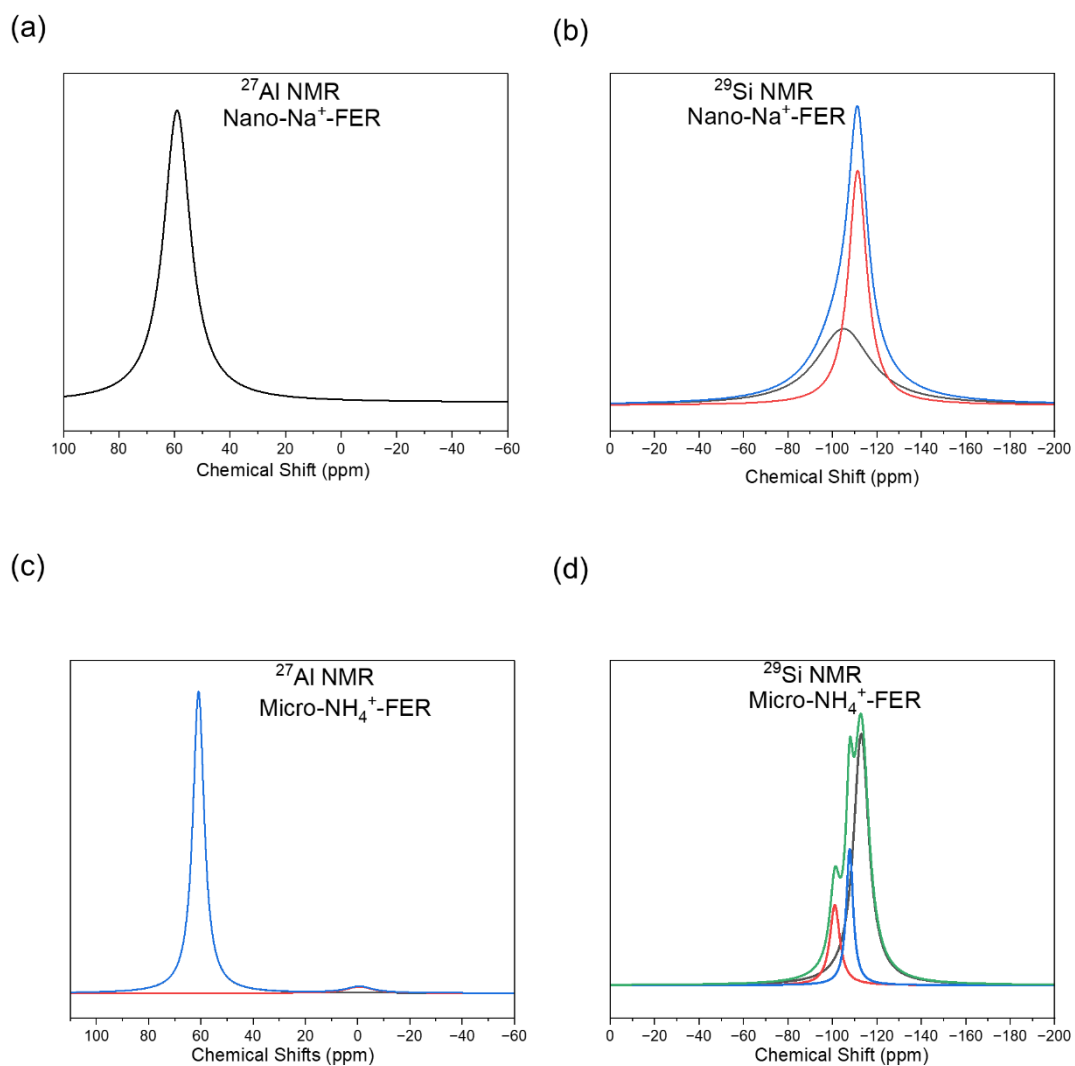


Figure A.1. Deconvoluted  $^{27}\text{Al}$  and  $^{29}\text{Si}$  MAS NMR of samples (a-b) Nano- $\text{Na}^+$ -FER, (c-d) Micro- $\text{NH}_4^+$ -FER

Table A.1. Al structure of Nano-FER and Micro-FER using Dedecek Method

<b>Sample</b>	<b>Si/Al</b>	<b>Co/Al</b>	<b>Al<sub>F</sub> (%)</b>	<b>Al arrangement</b>	
				<b>Al<sub>p</sub> (%)</b>	<b>Al<sub>i</sub> (%)</b>
<b>Micro-FER</b>	9.6	0.08	90.8	17	83
<b>Nano-FER</b>	12.8	0.1	100.0	20	80

## B. Detailed Activity Test Results

Table B.1. Micro-Cu-FER activity results 100 sccm total flow, 40% CH<sub>4</sub>, 15% N<sub>2</sub>O, 3% H<sub>2</sub>O, balance He at 325 °C (Reactant Heating). Yields based on per g<sub>zeolite</sub> (300 mg). r unit is μmolg<sup>-1</sup>h<sup>-1</sup>.

Catalyst	r	r	r	r	r	r	X (%)	TOF(h <sup>-1</sup> )	S (%)	r
	CH <sub>3</sub> OH	DME	CO <sub>2</sub>	CO	Coke	CH <sub>4</sub>	CH <sub>4</sub>	CH <sub>3</sub> OH	CH <sub>3</sub> OH	C <sub>2</sub> -C <sub>4</sub>
Micro-Cu-FER_1	809±5	96±2	8±2	30±4	165.2	1216	0.37	19.8	66.5	4.9±0.2
Micro-Cu-FER_2AR	626±3	57±2	16±1	88±5	191	860	0.26	8.9	59.6	5.3±0.3
Micro-Cu-FER_2BR	381±2	37±1	8±0.5	39±4	151	509	0.15	5.1	57.8	2.5±0.1
Micro-Cu-FER_2CR	346±3	22±1	15±0.3	73±2	155	482	0.15	4.3	54.2	2.1±0.1
Micro-CuNa-FER_2DR	194±0.5	0	35±0.3	104±5	168	337	0.10	2.2	38.4	1.8±0.2
Micro-Cu-FER_3R	130±1	3.5±0.5	31±0.3	90±8	122	262	0.08	0.8	34.0	1.0

Table B.2. Micro-Cu-FER activity results 100 sccm total flow, 40% CH<sub>4</sub>, 5-15% N<sub>2</sub>O, 3% H<sub>2</sub>O, balance He at 325 °C (Reactant Heating). Yields based on per g<sub>zeolite</sub> (300 mg). r unit is μmolg<sup>-1</sup>h<sup>-1</sup>.

Catalyst	r CH <sub>3</sub> OH	r DME	r CO <sub>2</sub>	r CO	r Coke	r CH <sub>4</sub>	X (%) CH <sub>4</sub>	TOF(h <sup>-1</sup> ) CH <sub>3</sub> OH	S (%) CH <sub>3</sub> OH	r C <sub>2</sub> -C <sub>4</sub>
Micro-Cu-FER_1 5%N <sub>2</sub> O	132±0.2	3.7±0.1	3±0.1	9±0.3	103	256	0.08	3.2	50.8	1.9±0.1
Micro-Cu-FER_1 Calcined	388±2	24±1	3.8±0.2	12±2	98	563	0.16	9.5	69.4	3.6±0.2

Table B.3. Meso-Steam/CTABr-Cu-FER activity results 100 sccm total flow, 40% CH<sub>4</sub>, 15% N<sub>2</sub>O, 3% H<sub>2</sub>O, balance He at 325 °C (Reactant Heating). Yields based on per g<sub>zeolite</sub> (300 mg). r unit is μmolg<sup>-1</sup>h<sup>-1</sup>.

Catalyst	r CH <sub>3</sub> OH	r DME	r CO <sub>2</sub>	r CO	r Coke	r CH <sub>4</sub>	X (%) CH <sub>4</sub>	TOF(h <sup>-1</sup> ) CH <sub>3</sub> OH	S (%) CH <sub>3</sub> OH	r C <sub>2</sub> -C <sub>4</sub>
Meso-Steam-Cu- FER_2CR	366±4	18±0.2	10±0.4	10±0.2	167	618.6	0.17	5.2	61.4	2.8±0.1
Meso-CTABr-Cu- FER_3R	183±2	7±0.3	0.3	36±0.9	115	252	0.10	0.6	51.9	1.8±0.1

Table B.4. Micro-Cu-SSZ-39 activity results 100 sccm total flow, 40% CH<sub>4</sub>, 15% N<sub>2</sub>O, 3% H<sub>2</sub>O, balance He at 325 °C (Reactant Heating). Yields based on per g<sub>zeolite</sub> (300 mg). r unit is μmolg<sup>-1</sup>h<sup>-1</sup>.

Catalyst	r CH <sub>3</sub> OH	r DME	r CO <sub>2</sub>	r CO	r Coke	r CH <sub>4</sub>	X (%) CH <sub>4</sub>	TOF(h <sup>-1</sup> ) CH <sub>3</sub> OH	S (%) CH <sub>3</sub> OH	r C <sub>2</sub> -C <sub>4</sub>
Micro-Cu-SSZ-39_3R	689±2	44±0.4	39±0.2	62±7	86	880	0.27	2.7	78.4	0
Micro-Cu-SSZ-39_4R	130±0.4	1.4±0.1	170±1	55±5	113	471	0.15	0.2	36.4	0

Table B.5. Micro-Cu-FER\_1 activity results 100 sccm total flow, 40% CH<sub>4</sub>, 15% N<sub>2</sub>O, 3% H<sub>2</sub>O, balance He at 325 °C (Reactant Heating). Yields based on per g<sub>zeolite</sub> (300 mg). r unit is μmolg<sup>-1</sup>h<sup>-1</sup>.

Catalyst	r CH <sub>3</sub> OH	r DME	r CO <sub>2</sub>	r CO	r Coke	r CH <sub>4</sub>	X (%) CH <sub>4</sub>	TOF(h <sup>-1</sup> ) CH <sub>3</sub> OH	S (%) CH <sub>3</sub> OH	r C <sub>2</sub> -C <sub>4</sub>
Micro-Cu-FER_1 1 <sup>st</sup> Usage	809±5	96±2	8±2	30±4	165.2	1216	0.37	19.8	66.5	4.9±0.2
Micro-Cu-FER_1 2 <sup>nd</sup> Usage	630±5	63±1	28±3	54±6	2.9	848	0.26	15.4	74.2	2.7±0.3
Micro-Cu-FER_1 3 <sup>rd</sup> Usage	262±1	14±1	0.3	2±0.5	1.6	298	0.09	6.4	88.1	1.6±0.1

Table B.6. Micro-Cu-FER\_1 activity results 100 sccm total flow, 40% CH<sub>4</sub>, 15% N<sub>2</sub>O, 3% H<sub>2</sub>O, balance He at 325 °C (Helium Heating). Yields based on per g<sub>zeolite</sub> (300 mg). r unit is μmolg<sup>-1</sup>h<sup>-1</sup>.

Catalyst	r CH <sub>3</sub> OH	r DME	r CO <sub>2</sub>	r CO	r Coke	r CH <sub>4</sub>	X (%) CH <sub>4</sub>	TOF(h <sup>-1</sup> ) CH <sub>3</sub> OH	S (%) CH <sub>3</sub> OH	r C <sub>2</sub> H <sub>4</sub>
Micro-Cu-FER_1 1 <sup>st</sup> Usage	1249±6	216±3	26±1	23±4	241	2003	0.60	30.6	62.3	13.4±0.3
Micro-Cu-FER_1 2 <sup>nd</sup> Usage	1360±3	250±8	39±6	100±9	150	2172	0.65	33.4	62.6	9±0.1
Micro-Cu-FER_1 3 <sup>rd</sup> Usage	1325±2	229±4	33±1	32±66	141	2012	0.60	32.5	65.6	9.7±0.6

Table B.7. Micro-Cu-FER activity results 100 sccm total flow, 40% CH<sub>4</sub>, 15% N<sub>2</sub>O, 3% H<sub>2</sub>O, balance He at 325 °C (Helium Heating). Yields based on per g<sub>zeolite</sub> (300 mg). r unit is μmolg<sup>-1</sup>h<sup>-1</sup>.

Catalyst	r CH <sub>3</sub> OH	r DME	r CO <sub>2</sub>	r CO	r Coke	r CH <sub>4</sub>	X (%) CH <sub>4</sub>	TOF(h <sup>-1</sup> ) CH <sub>3</sub> OH	S (%) CH <sub>3</sub> OH	r C <sub>2</sub> -C <sub>4</sub>
Micro-Cu-FER_1	1249±6	216±3	26±1	23±4	241	2003	0.60	30.6	62.3	13.4±0.3
Micro-Cu-FER_2	914±2	108±0.5	52±2	122±7	187	1507	0.46	12.7	60.7	8.1±0.3
Micro-Cu-FER_3	98±0.5	4±0.2	636±4	401±11	49	1192	0.36	0.4	8.2	0.1

Table B.8. Nano-Cu-FER activity results 100 sccm total flow, 40% CH<sub>4</sub>, 15% N<sub>2</sub>O, 3% H<sub>2</sub>O, balance He at 325 °C (Helium Heating). Yields based on per g<sub>zeolite</sub> (300 mg). r unit is μmolg<sup>-1</sup>h<sup>-1</sup>.

Catalyst	r	r	r	r	r	r	X (%)	TOF(h <sup>-1</sup> )	S (%)	r
	CH <sub>3</sub> OH	DME	CO <sub>2</sub>	CO	Coke	CH <sub>4</sub>	CH <sub>4</sub>	CH <sub>3</sub> OH	CH <sub>3</sub> OH	C <sub>2</sub> -C <sub>4</sub>
Nano-Cu-FER_1	1594±6	245±6	26±1	28±6	149	2495	0.75	45	68.0	25±2
Nano-Cu-FER_2	586±8	46±2	126±1	76±5	133	1154	0.35	7	57.3	4.7±0.5

Table B.9. Micro-Cu-SSZ-39 activity results 100 sccm total flow, 40% CH<sub>4</sub>, 15% N<sub>2</sub>O, 3% H<sub>2</sub>O, balance He at 325 °C (Helium Heating). Yields based on per g<sub>zeolite</sub> (300 mg). r unit is μmolg<sup>-1</sup>h<sup>-1</sup>.

Catalyst	r	r	r	r	r	r	X (%)	TOF(h <sup>-1</sup> )	S (%)	r
	CH <sub>3</sub> OH	DME	CO <sub>2</sub>	CO	Coke	CH <sub>4</sub>	CH <sub>4</sub>	CH <sub>3</sub> OH	CH <sub>3</sub> OH	C <sub>2</sub> -C <sub>4</sub>
Micro-Cu-SSZ-39_2	81±1	1±0.1	11±0.5	21±4	260	970	0.29	1	8.3	245±9
Micro-Cu-SSZ-39_3	905±2	118±3	79±1	208±9	63	1505	0.45	4.8	60.1	6.3±0.5

Table B.10. Micro-Cu-SSZ-13 activity results 100 sccm total flow, 40% CH<sub>4</sub>, 15% N<sub>2</sub>O, 3% H<sub>2</sub>O, balance He at 325 °C (Helium Heating). Yields based on per g<sub>zeolite</sub> (300 mg). r unit is μmolg<sup>-1</sup>h<sup>-1</sup>.

Catalyst	r	r	r	r	r	r	X (%)	TOF(h <sup>-1</sup> )	S (%)	r
	CH <sub>3</sub> OH	DME	CO <sub>2</sub>	CO	Coke	CH <sub>4</sub>	CH <sub>4</sub>	CH <sub>3</sub> OH	CH <sub>3</sub> OH	C <sub>2</sub> -C <sub>4</sub>
Micro-Cu-SSZ-13_1	245±1	10±0.1	24±0.1	8±2	53	358	0.11	4.3	68.4	4.5±0.5
Micro-Cu-SSZ-13_2	182±1	8±0.2	138±2	106±8	54	497	0.15	2.3	36.6	0.8

Table B.11. Micro-Cu-FER\_1 activity results 100 sccm total flow, 40% CH<sub>4</sub>, 15% N<sub>2</sub>O, 0-9% H<sub>2</sub>O, balance He at 325 °C (Helium Heating). Yields based on per g<sub>zeolite</sub> (300 mg). r unit is μmolg<sup>-1</sup>h<sup>-1</sup>.

Catalyst	r	r	r	r	r	r	X (%)	TOF(h <sup>-1</sup> )	S (%)	r
	CH <sub>3</sub> OH	DME	CO <sub>2</sub>	CO	Coke	CH <sub>4</sub>	CH <sub>4</sub>	CH <sub>3</sub> OH	CH <sub>3</sub> OH	C <sub>2</sub> -C <sub>4</sub>
Micro-Cu-FER_1 0% H <sub>2</sub> O	152±2	152±1	8±0.2	11±2	314	856	0.25	3.7	17.7	22.2±0.4
Micro-Cu-FER_1 3% H <sub>2</sub> O	1249±6	216±3	26±1	23±4	241	2003	0.60	30.6	62.3	13.4±0.3
Micro-Cu-FER_1 6% H <sub>2</sub> O	1616±6	73±2	24±1	52±4	111	1965	0.60	39.6	82.2	7.6±0.2
Micro-Cu-FER_1 9% H <sub>2</sub> O	1749±5	98±1	24±1	136±3	44	2166	0.66	42.9	80.8	7.3±0.3

Table B.12. Nano-Cu-FER\_1 activity results 100 sccm total flow, 40% CH<sub>4</sub>, 15% N<sub>2</sub>O, 0-9% H<sub>2</sub>O, balance He at 325 °C (Helium Heating). Yields based on per g<sub>zeolite</sub> (300 mg). r unit is μmolg<sup>-1</sup>h<sup>-1</sup>.

Catalyst	r	r	r	r	r	r	X (%)	TOF(h <sup>-1</sup> )	S (%)	r
	CH <sub>3</sub> OH	DME	CO <sub>2</sub>	CO	Coke	CH <sub>4</sub>	CH <sub>4</sub>	CH <sub>3</sub> OH	CH <sub>3</sub> OH	C <sub>2</sub> -C <sub>4</sub>
Nano-Cu-FER_1 0% H <sub>2</sub> O	694±4	497±6	37±1	40±7	631	2701	0.82	19.6	25.7	97±1
Nano-Cu-FER_1 3% H <sub>2</sub> O	1594±6	245±6	26±1	28±6	149	2495	0.75	45	68.0	25±2
Nano-Cu-FER_1 6% H <sub>2</sub> O	2071±4	183±2	19±1	9±2	131	2625	0.80	58.5	78.9	11.3±0. 3
Nano-Cu-FER_1 9% H <sub>2</sub> O	2174±6	222±3	14±0.5	10±1	72	2816	0.86	61.5	79.2	12.7±0. 7

Table B.13. Micro-Cu-FER\_1 activity results 100 sccm total flow, 40% CH<sub>4</sub>, 15% N<sub>2</sub>O, 3% H<sub>2</sub>O, balance He at different temperatures (Helium Heating). Yields based on per g<sub>zeolite</sub> (300 mg). r unit is μmolg<sup>-1</sup>h<sup>-1</sup>.

Catalyst	r CH <sub>3</sub> OH	r DME	r CO <sub>2</sub>	r CO	r Coke	r CH <sub>4</sub>	X (%) CH <sub>4</sub>	TOF(h <sup>-1</sup> ) CH <sub>3</sub> OH	S (%) CH <sub>3</sub> OH	r C <sub>2</sub> -C <sub>4</sub>
Micro-Cu-FER_1 311 °C	319±3	27±1	5±0.1	5±1	159	546	0.16	7.8	58.3	2.2±0.4
Micro-Cu-FER_1 318 °C	773±4	114±2	20±0.2	38±4	180	1253	0.37	19	61.7	6.3±0.6
Micro-Cu-FER_1 325 °C	1249±6	216±3	26±1	23±4	241	2003	0.60	30.6	62.3	13.4±0. 3

Table B.14. Micro-Cu-FER\_2 activity results 100 sccm total flow, 40% CH<sub>4</sub>, 15% N<sub>2</sub>O, 3% H<sub>2</sub>O, balance He at different temperatures (Helium Heating). Yields based on per g<sub>zeolite</sub> (300 mg). r unit is μmolg<sup>-1</sup>h<sup>-1</sup>.

Catalyst	r CH <sub>3</sub> OH	r DME	r CO <sub>2</sub>	r CO	r Coke	r CH <sub>4</sub>	X (%) CH <sub>4</sub>	TOF(h <sup>-1</sup> ) CH <sub>3</sub> OH	S (%) CH <sub>3</sub> OH	r C <sub>2</sub> -C <sub>4</sub>
Micro-Cu-FER_2 311 °C	561±2	46±0.2	37±2	0	141	841	0.25	7.8	66.8	4.3±0.2
Micro-Cu-FER_2 318 °C	734±5	67±1	42±2	65±5	157	1145	0.35	10.2	64.1	6.3±0.4
Micro-Cu-FER_2 325 °C	914±2	108±0.5	52±2	122±7	187	1507	0.46	12.7	60.7	8.1±0.3

Table B.15. Micro-Cu-FER\_3 activity results 100 sccm total flow, 40% CH<sub>4</sub>, 15% N<sub>2</sub>O, 3% H<sub>2</sub>O, balance He at different temperatures (Helium Heating). Yields based on per g<sub>zeolite</sub> (300 mg). r unit is μmolg<sup>-1</sup>h<sup>-1</sup>.

Catalyst	r CH <sub>3</sub> OH	r DME	r CO <sub>2</sub>	r CO	r Coke	r CH <sub>4</sub>	X (%) CH <sub>4</sub>	TOF(h <sup>-1</sup> ) CH <sub>3</sub> OH	S (%) CH <sub>3</sub> OH	r C <sub>2</sub> -C <sub>4</sub>
Micro-Cu-FER_3 311 °C	74±0.5	1±0.3	230±4	87±8	150	697	0.21	0.3	18.6	0.8
Micro-Cu-FER_3 318 °C	88±0.6	2±0.1	329±3	180±9	156	760	0.23	0.4	11.6	0.9
Micro-Cu-FER_3 325 °C	98±0.5	4±0.2	636±4	401±11	49	1192	0.36	0.4	8.2	0.1

Table B.16. Nano-Cu-FER\_1 activity results 100 sccm total flow, 40% CH<sub>4</sub>, 15% N<sub>2</sub>O, 3% H<sub>2</sub>O, balance He at different temperatures (Helium Heating). Yields based on per g<sub>zeolite</sub> (300 mg). r unit is μmolg<sup>-1</sup>h<sup>-1</sup>.

Catalyst	r	r	r	r	r	r	X (%)	TOF(h <sup>-1</sup> )	S (%)	r
	CH <sub>3</sub> OH	DME	CO <sub>2</sub>	CO	Coke	CH <sub>4</sub>	CH <sub>4</sub>	CH <sub>3</sub> OH	CH <sub>3</sub> OH	C <sub>2</sub> H <sub>4</sub>
Nano-Cu-FER_1 311 °C	689±2	64±0.5	8±0.1	2±0.5	292	1461	0.44	19.5	58.9	23±1
Nano-Cu-FER_1 318 °C	1184±4	129±3	22±1	9±2	199	1710	0.52	36.7	69.2	16.4±0.4
Nano-Cu-FER_1 325 °C	1594±6	245±6	26±1	28±6	149	2495	0.75	45	68.0	25±2

Table B.17. Nano-Cu-FER\_2 activity results 100 sccm total flow, 40% CH<sub>4</sub>, 15% N<sub>2</sub>O, 3% H<sub>2</sub>O, balance He at different temperatures (Helium Heating). Yields based on per g<sub>zeolite</sub> (300 mg). r unit is μmolg<sup>-1</sup>h<sup>-1</sup>.

Catalyst	r CH <sub>3</sub> OH	r DME	r CO <sub>2</sub>	r CO	r Coke	r CH <sub>4</sub>	X (%) CH <sub>4</sub>	TOF(h <sup>-1</sup> ) CH <sub>3</sub> OH	S (%) CH <sub>3</sub> OH	r C <sub>2</sub> -C <sub>4</sub>
Nano-Cu-FER_1 311 °C	368±3	14±1	81±2	109±8	140	872	0.26	4.4	50.3	2.3±0.1
Nano-Cu-FER_1 318 °C	475±5	23±1	143±4	174±7	149	1138	0.35	5.7	48.1	0.3
Nano-Cu-FER_1 325 °C	586±8	46±2	126±1	76±5	133	1231	0.35	7	57.3	4.7±0.5